ISSN 0370—8691

NATIONAL ACADEMY OF SCIENCES OF THE REPUBLIC OF ARMENIA

Communications of the Byurakan Astrophysical Observatory

1

Erevan 2019

Communications of BAO, Vol. 66, Issue 1, 2019, pp. 1 - 7

Classification of BZCAT objects having uncertain types

H.V.Abrahamyan[*], A.M.Mickaelian[†], G.M.Paronyan[‡], G.A.Mikayelyan[§] and M.V.Gyulzadyan[¶]

NAS RA V. Ambartsumian Byurakan Astrophysical Observatory (BAO), Armenia

Abstract

In this work we try to understand some optical properties of blazars having uncertain types (BZU) in BZCAT vs. 5 Catalogue. Cross-correlation with SDSS reveals 43 BZU out of 227 that have spectra in SDSS. We have carried out spectral reclassification for these 43 blazar candidates (BZU) for activity types. As a result, 37 (86%) objects out of 43 changed their previous type.

Keywords: *blazar, active galactic nuclei.*

1. Introduction

Blazars are considered to be the most energetic sources in the Universe. BLL Lac was discovered by the Hoffmeister (Hoffmeister, 1929). The originally discovered source was considered to be a variable star. Later, a thorough study of this source showed that it was extragalactic radio source. Discovered source was a radio source which had optical variability. Nowadays 3,561 blazars are known. The disclosed sources have been published by Massaro et al. (2015) as a general list. In this catalog, Massaro grouped all blazars in four main classes: BZB, BZQ, BZG and BZU. According to the definition, blazars should be radio sources and have optical variability. But information about variability is not complete in this catalogue. Information for optical variability of blazars is given by Abrahamyan et al. (2019).

From BZCAT catalog, we cannot understand which sources are called Blazars. Using this catalogue we plan to take out definition of blazars. But in the first step we must understand properties of different types of Blazars. The most important and very interesting sources are blazars, which are classified as uncertain type (BZU). In this type included sources which have not good spectra, or have united properties which have other types of blazars. So, for better understanding of Blazars we must carry out investigations of all types of Blazars and take out united properties.

For summarize different physical properties of blazars we must understand which properties show different types of blazars (BZU, BZB, BZG and BZU).
This work is dedicated to classification of 43 blazars having uncertain type (BZU) in BZCAT catalogue v.5 (Massaro et al., 2015).

2. Observational data

For our investigation we take BZCAT v.5 (Massaro et al., 2015), which includes 3561 blazars. In BZCAT blazars have 4 types (table 1). In table 1 we can see 227 objects out of 3561 have uncertain

[*]abrahamyanhayk@gmail.com, Corresponding author
[†]aregmick@yahoo.com
[‡]gurgen@bao.sci.am
[§]gormick@mail.ru
[¶]mgyulz@gmail.com

DOI: 10.52526/25792776-2019.66.1-1

Table 1. Distribution of types of objects in BZCAT.

N	Type	Numbers
1	BZB	1151
2	BZG	274
3	BZQ	1909
4	BZU	227
All		**3561**

types of blazars. For our investigation we take these 227 BZU objects.

In the First step we cross-corelated these objects with SDSS (Fan et al., 1999). In results we have 81 identification from which 43 have spectra. Our work is dedicated to these 43 objects. For a better understanding of the properties of BZU objects we cross-correlated with VCV-13 (Véron-Cetty & Véron, 2010), SDSS and NED (table 2).

Table 2. The list of BZU objects with their activity types and radio morphology.

BZCAT name	SDSS	VCV	NED		
		Sp.	Object Type	Radio Morphology Homogenized Classification	Activity Type Homogenized Classification
5BZUJ0217-0820	Star	BL	QSO		BL Lac
5BZUJ0304+0002	Star		QSO		QSO
5BZUJ0742+3744	Star		QSO		QSO
5BZUJ0840+1312	Star	S1.2	QSO	FR II	Sy 1.2
5BZUJ0849+5108	Star	S1n	QSO		Flat-Spectrum Radio Source
5BZUJ0856+0140	Star	BL	G		BL Lac
5BZUJ0909+4253	Star	S2	QSO	Core-Dominated	CSS
5BZUJ0933+0003	Galaxy	BL?	RadioS		
5BZUJ0954+5719	Star		QSO		QSO
5BZUJ1000+2233	Star	S2	QSO		
5BZUJ1021+4523	Star		G	radio jet	Flat-Spectrum Radio Source
5BZUJ1030+3102	Galaxy	S1.5	G	radio jet	Flat-Spectrum Radio Source
5BZUJ1033+0711	Galaxy		RadioS		Flat-Spectrum Radio Source
5BZUJ1051+4644	Star		QSO		Flat-Spectrum Radio Source
5BZUJ1058+0133	Star	HP	QSO	radio jet	BL Lac
5BZUJ1059+4051	Star		RadioS		
5BZUJ1153+5831	Galaxy	S1.5	QSO		Sy 1.5
5BZUJ1208+6121	Galaxy	BL?	G		BL Lac
5BZUJ1225+4834	Star		QSO		QSO
5BZUJ1238+5325	Star	S1	G		Sy 1
5BZUJ1257+0024	Star		QSO		QSO
5BZUJ1302+5748	Star		QSO		Flat-Spectrum Radio Source
5BZUJ1310+3220	Star	HP	QSO		Flat-Spectrum Radio Source
5BZUJ1345+4125	Star		QSO		
5BZUJ1345+5332	Galaxy	S1	G		
5BZUJ1347+3012	Star		QSO		QSO
5BZUJ1353+0443	Star		QSO		Flat-Spectrum Radio Source
5BZUJ1431-0052	Star		QSO		QSO
5BZUJ1435+2021	Star	BL?	G		Flat-Spectrum Radio Source
5BZUJ1448+0402	Star	S2	G		Flat-Spectrum Radio Source
5BZUJ1449+4221	Galaxy	S2	QSO		Flat-Spectrum Radio Source
5BZUJ1458+0416	Star		QSO		Flat-Spectrum Radio Source
5BZUJ1511+0518	Galaxy	S1	G		Flat-Spectrum Radio Source
5BZUJ1536+3742	Galaxy		G		
5BZUJ1550+1120	Star	S1.5	QSO		Flat-Spectrum Radio Source
5BZUJ1557+3304	Star		QSO	radio jet	QSO
5BZUJ1602+2646	Galaxy	S2	G		Flat-Spectrum Radio Source
5BZUJ1603+1554	Galaxy		G		Flat-Spectrum Radio Source
5BZUJ1618+2159	Star	S1	QSO		
5BZUJ1633+2112	Galaxy	S1	QSO		
5BZUJ1706+3214	Star		RadioS		
5BZUJ2156-0037	Star	BL	QSO		Flat-Spectrum Radio Source
5BZUJ2327+1524	Galaxy	S1	G		Flat-Spectrum Radio Source

Using table 2 we can conclude the following:

- In SDSS: 13 objects are "galaxies" (extended objects) and 30 are "stars" (point-like objects),
- In VCV-13: 6 objects are BL or BL?, 2 objects are HP (HPQ), 6 objects are Sy1, 1 object is Sy1.2, 3 objects are Sy1.5, 1 object is Sy1n (Narrow Line Seyfert 1), 5 objects are Sy2, and for 19 objects we do not have any information,
- In NED: 13 objects are galaxies, 26 objects are quasars and 4 objects are RadioS (radio sources). Among these objects we have 4 BL Lac, 18 FSS (Flat-Spectrum Radio Source), 1 CSS (Compact Steep Spectrum), 1 Sy1, 1 Sy1.2, and 1 Sy 1.5,
- In NED we have radio morphology: 4 objects have radio jets, 1 object is FRII and 1 object is core-dominated radio object.

In Figure 1, we give redshift distribution of BZU and distribution of 43 objects, which have spectra in SDSS.

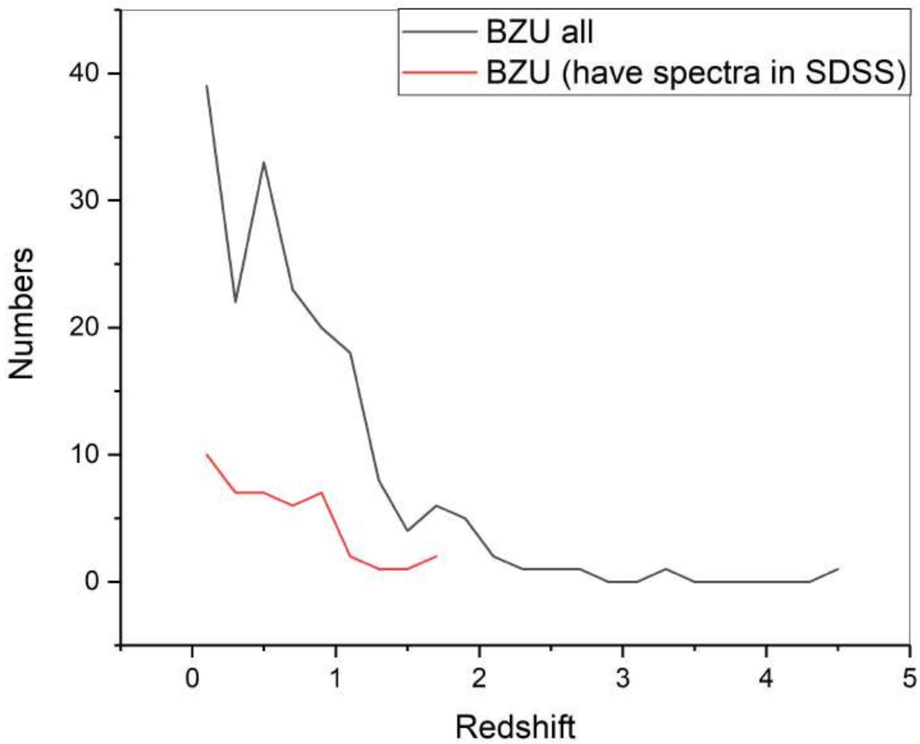

Figure 1. Redshift distribution of BZU objects.

In figure 1 BZU source mainly have 0 until 2.2 redshift and our studied sources have 0 until 1.75 redshift. For these 43 sources we have done classification using SDSS spectra.

For understanding some physical properties of blazars we use the paper Abrahamyan et al. (2019). In this paper calculated absolute magnitude for all blazars. In Figure 2, we give graphs of the absolute magnitude versus redshift.

In Figure 2 our investigated sources have -21 to -25 absolute magnitudes.

So, using 43 SDSS spectra for our sources, we have carried out optical classification.

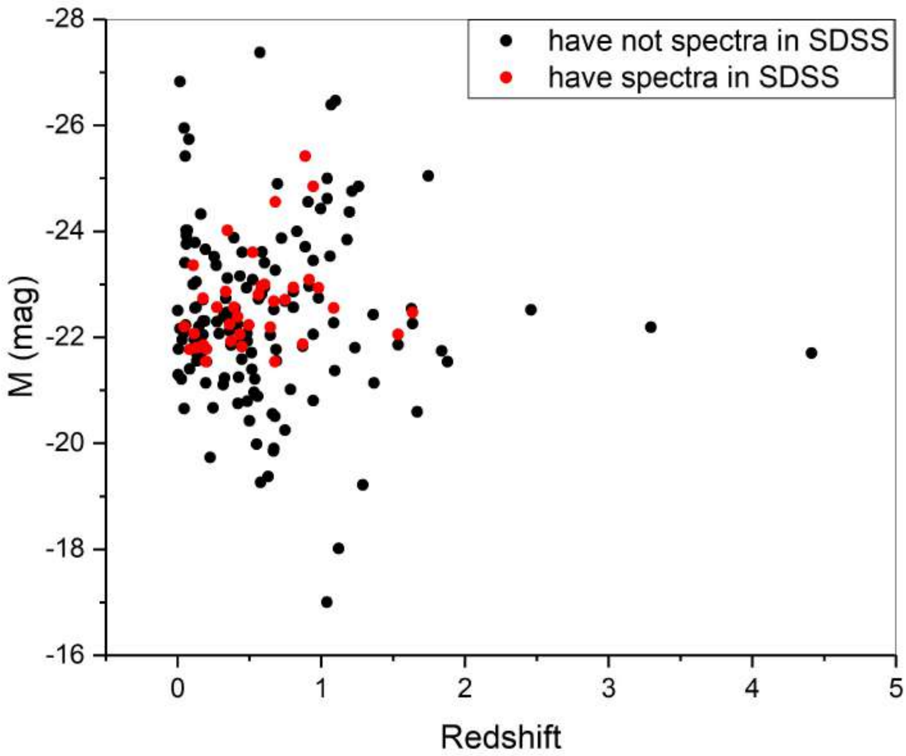

Figure 2. Absolute magnitude vs. redshift.

3. Classification method and results

We have used several methods for classification of our spectra (Mickaelian et al., 2018);

- By eye (taking into account all features and effects)
- By diagnostic diagram using [OIII]/H_β and [NII]/H_α ratios (Reines et al., 2013),
- By diagnostic diagram using [OIII]/H_β and [SII]/H_α ratios (Reines et al., 2013),
- By diagnostic diagram using [OIII]/H_β and [OI]/H_α ratios (Reines et al., 2013),

We have done classification only by eye, because we have not enough information for diagnostic diagrams from the spectra.

We started the studying of spectra with identifications of spectral lines. We have used only lines having intensities 3 sigma over the noise level.
In Figure 3 we give 4 spectra out of 43 our investigated blazars.

In order to do classification, we need to consider the classification Massaro et al. (2015):

- **BZB**: BL Lac objects, used for AGNs with a featureless optical spectrum, or having only absorption lines of galactic origin and weak and narrow emission lines (Massaro et al., 2015);
- **BZG** objects, usually reported as BL Lac objects in the literature, but having a spectral energy distribution (SED) with a significant dominance of the galactic emission over the nuclear one (Massaro et al., 2015);

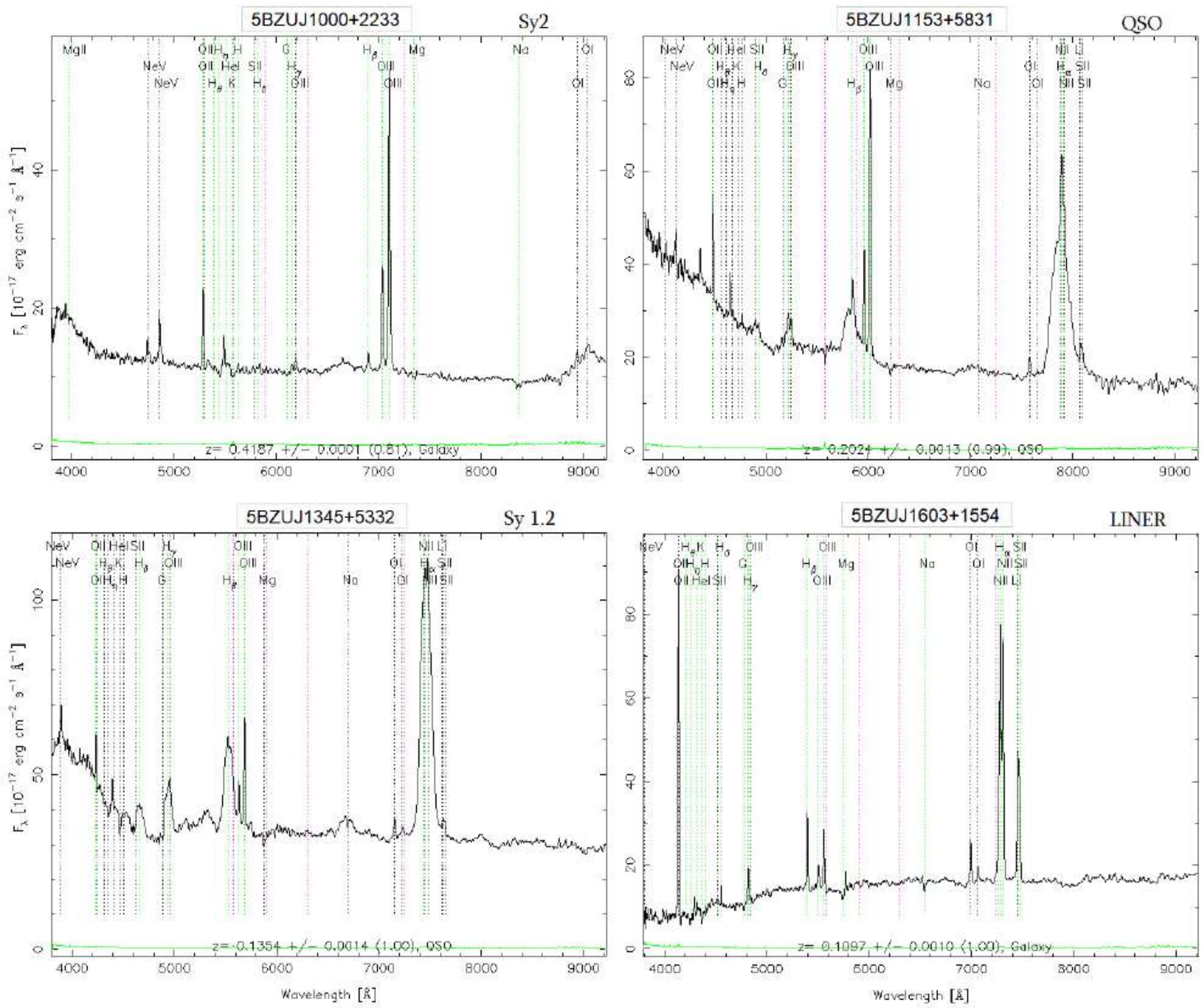

Figure 3. Examples of spectra.

- **BZQ**: Flat Spectrum Radio Quasars, with an optical spectrum showing broad emission lines and dominant blazar characteristics (Massaro et al., 2015).

Using classification of BZCAT given in Massaro et al. (2015). we have carried out classification of 43 sources which have uncertain type.
So, 37 BZU objects from 43 changed their classification to BZQ, BZG and BZG. In table 3 we give the new classification and redshifts from SDSS.

In table 3 we give old and new classification, and give activity type using SDSS spectra. And we give redshift form catalogue BZCAT v. 5, NED and SDSS. For 5 sources we checked and corrected redshift and for 4 sources is given by SDSS and for 1 source is given by BZCAT.

4. Conclusion

So, having optical spectra of 43 BZU, we reclassified these objects. As the main results we have:

1) 37 (86%) objects from 43 changed classification (table 4).

2) In table 3 we give information of redshift from BZCAT, SDSS and NED. For 5 objects that numbers are different (5BZUJ0933+0003, 5BZUJ1051+4644, 5BZUJ1058+0133, 5BZUJ1302+5748, 5BZUJ2156-0037). We checked and corrected redshift and for 4 (5BZUJ0933+0003, 5BZUJ1051+4644, 5BZUJ1302+5748, 5BZUJ2156-0037) sources is given by SDSS and for 1 (5BZUJ1058+0133) sources is given by BZCAT.

Table 3. New classification of BZU objects.

BZCAT v.5		**Our classifaction**		**Redshift**		
Source name	**Type**			**BZCAT**	**NED**	**SDSS**
5BZUJ0217-0820	BZU	NLQSO	BZQ	0.607	0.606538	0.60654
5BZUJ0304+0002	BZU	QSO1.2	BZQ	0.564	0.56417	0.56366
5BZUJ0742+3744	BZU	QSO1.5	BZQ	0.806	0.806274	0.80574
5BZUJ0840+1312	BZU	QSO1.2	BZQ	0.681	0.6808	0.68037
5BZUJ0849+5108	BZU	QSO	BZQ	0.583	0.584701	0.58345
5BZUJ0856+0140	BZU	Unknown	BZU	0.448	0.448184	0.44807
5BZUJ0909+4253	BZU	QSO	BZQ	0.670	0.669915	0.67041
5BZUJ0933+0003	BZU	Unknown	BZU	0^{b}		0.71107^{a}
5BZUJ0954+5719	BZU	QSO	BZQ	0.981	0.981193	0.98121
5BZUJ1000+2233	BZU	Sy2.0	BZG	0.419	0.418732	0.41874
5BZUJ1021+4523	BZU	QSO	BZQ	0.364	0.36388	0.36437
5BZUJ1030+3102	BZU	QSO	BZQ	0.178	0.1782	0.17815
5BZUJ1033+0711	BZU	Unknown	BZU	1.535		1.52948
5BZUJ1051+4644	BZU	Unknown	BZU	0^{b}	1.419418^{b}	0.00005^{a}
5BZUJ1058+0133	BZU	BLL	BLB	0.890^{a}	0.89^{a}	0.3823^{b}
5BZUJ1059+4051	BZU	QSO	BZQ	1.746		1.75049
5BZUJ1153+5831	BZU	QSO	BZQ	0.202	0.202439	0.2024
5BZUJ1208+6121	BZU	Abs	BZG	0.275	0.274783	0.27479
5BZUJ1225+4834	BZU	QSO	BZQ	0.647	0.646553	0.64687
5BZUJ1238+5325	BZU	QSO1.2	BZQ	0.348	0.347506	0.34684
5BZUJ1257+0024	BZU	QSO	BZQ	1.259	1.260971	1.25808
5BZUJ1302+5748	BZU	Unknown	BZU	1.088^{b}	1.088^{b}	0.83066^{a}
5BZUJ1310+3220	BZU	QSO	BZQ	0.997	0.998007	0.99725
5BZUJ1345+4125	BZU	QSO	BZQ	0.916	0.916932	0.91654
5BZUJ1345+5332	BZU	Sy1.2	BZG	0.135	0.135406	0.13537
5BZUJ1347+3012	BZU	Sy1.5	BZG	0.118	0.11785	0.11784
5BZUJ1353+0443	BZU	QSO	BZQ	0.523	0.522821	0.5234
5BZUJ1431-0052	BZU	QSO	BZQ	1.635	1.633083	1.63687
5BZUJ1435+2021	BZU	Em	BZG	0.748	0.748	0.74768
5BZUJ1448+0402	BZU	Em	BZG	0.871	0.8712	0.8712
5BZUJ1449+4221	BZU	Sy2.0	BZG	0.179	0.1783	0.17867
5BZUJ1458+0416	BZU	Em	BZG	0.392	0.391547	0.39154
5BZUJ1511+0518	BZU	Sy2.0	BZG	0.084	0.084	0.08452
5BZUJ1536+3742	BZU	Em	BZG	0.679	0.679211	0.67911
5BZUJ1550+1120	BZU	Sy1.5	BZG	0.436	0.43598	0.43567
5BZUJ1557+3304	BZU	QSO	BZQ	0.943	0.944472	0.94962
5BZUJ1602+2646	BZU	LINER	BZG	0.372	0.371657	0.37171
5BZUJ1603+1554	BZU	LINER	BZG	0.110	0.109866	0.10971
5BZUJ1618+2159	BZU	QSO	BZQ	0.336	0.334828	0.3348
5BZUJ1633+2112	BZU	Sy1.8	BZG	0.198	0.198156	0.1982
5BZUJ1706+3214	BZU	QSO	BZQ	1.070		1.06979
5BZUJ2156-0037	BZU	Unknown	BZU	$0.495?^{b}$	0.495^{b}	2.23931^{a}
5BZUJ2327+1524	BZU	QSO	BZQ	0.046	0.045717	0.04581

(a) Right measurement.
(b) Wrong measurement.

3) Using SDSS spectra we have carried out classification in optical range. In table 5 we give

Table 4. New classification of BZU.

N	Old	New	Numbers
1	BZU	BZB	1 (2%)
2	BZU	BZG	14 (33%)
3	BZU	BZQ	22 (51%)
4	BZU	BZU	6 (14%)
All			**43 (100%)**

information for this classification.

Table 5. Spectral classification using SDSS spectra

Activity Type	**Numbers**
Abs	1
BLL	1
Em	4
LINER	2
NLQSO	1
QSO	17
QSO 1.2	3
QSO 1.5	1
Sy 1.2	1
Sy 1.5	2
Sy 1.8	1
Sy 2.0	3
Unknown	6
Total	43

In VCV–13 catalogue, if the absolute magnitude is more than -22.25 then the sources are classified as quasars in Véron-Cetty & Véron (2010). So, using that, among our sources we had classification QSO 1.2 and QSO 1.5. If these sources have absolute magnitude less than -22.25, we classify them as Sy1.2 and Sy1.5.
QSO 1.2 and QSO 1.5 have the same properties which have Sy 1.2 and Sy1.5, and according to VCV catalogue there is only absolute magnitude limit -22.25.

References

Abrahamyan H. V., Mickaelian A. M., Mikayelyan G. A., Paronyan G. M., 2018, ComBAO, 2 (LXV), 1

Abrahamyan H. V., Mickaelian A. M., Paronyan G. M., Mikayelyan G. A., 2019, AN, 5, 437

Fan X., Strauss M. A., Schneider D. P., et al. 1999, AJ, 1, 118

Hoffmeister C., 1929, AN, 233, 236

Massaro E., Alessandro M., Cristina L., 2015, Ap.SS, 4, 357

Mickaelian A. M., Harutyunyan G. S., Sarkissian A., 2018, Astronomy Letters, 6, 44

Paronyan G. M., Mickaelian A. M., Harutyunyan G. S., Abrahamyan H. V., Mikayelyan G. A., 2019, Astrophysics, 62, 147

Reines A. E., Greene J. E., Geha M., 2013, AJ, 2, 755

Véron-Cetty M.-P., Véron P., 2010, A&A, A10, 518

The role of dipolar magnetic field of AGN in the morphology and evolution of extragalactic radio sources

R.R. Andreasyan *

NAS RA V. Ambartsumian Byurakan Astrophysical Observatory (BAO), Armenia

Abstract

We discuss a model of formation of extragalactic radio sources when the parent optical galaxy has a large-scale dipolar magnetic field. The study of dynamics of ejected from the central part of optical galaxy clouds of relativistic particles in dipolar magnetic field gives a possibility to explain main morphological features and physical properties of formed extragalactic radio sources. We bring some results of statistical analyses and correlations between physical parameters for a large sample of extragalactic radio sources.

Keywords: *Magnetic field, radio sources, radio galaxies, Active Galactic Nuclei*

1. Introduction

It is well known that the magnetic field has an important role in the dynamics evolution and radiation of extragalactic radio sources. Almost in all known theories of formation and evolution of extragalactic radio sources as a mechanism of radiation in radio waves are suggested synchrotron radiation of relativistic plasma in the magnetic field without of concretization of the large-scale configuration of magnetic field or of the role of field configuration in the observing morphology of extragalactic radio sources. For example in most known Blandford & Znajek (1977) mechanism is supposed the existence of large angular momentum and strong magnetic field, parallel to the rotation axes of the Kerr black hole. Relativistic particles are moving along the magnetic field lines and radiating in this field. As there are no magnetic monopoles in the Universe one must consider that the parallel (in the central part of Active Galactic Nuclei (AGN)) lines of magnetic field will be closed in any place of galaxy. From the conclusion of symmetry this magnetic field can have a dipolar form. Another interpretation of the morphology of extragalactic radio sources was suggested by Luhmann (1979), what concerns the possibility that the emission arises from the belts of trapped in dipolar magnetic field electrons, encircling the parent galaxy in the same manner as the Van Allen belts encircle the Earth. In Andreasyan (1983)(hereafter the paper 1)) we have suggested a mechanism of the formation and evolution of extragalactic radio sources in framework of the cosmological conception of V.Ambartsumian (Ambartsumian, 1966). This mechanism was as a hybrid of (Blandford & Znajek, 1977) and (Luhmann, 1979) mechanisms. But in Andreasyan (1983)it was done a main suggestion about the magnetic field configuration of host supergiant elliptical galaxy. We conclude that the magnetic field of the host galaxy or AGN has a dipole configuration, with dipole axes parallel to the rotation axes of host galaxy. Extragalactic radio sources are formed from relativistic plasma clouds, ejected from the central part of the optical galaxy and moving in its large-scale, dipole magnetic field. In the frame of suggested mechanism the well-known Fanaroff-Ryley Dichotomy (Fanaroff & Riley, 1974) and many other morphological fetchers finds a very simple physical explanation.

*randrasy@bao.sci.am

DOI: 10.52526/25792776-2019.66.1-8

2. The large scale magnetic field of parent galaxies

The first main suggestion for the mechanism of the formation and evolution of extragalactic radio sources in Andreasyan (1983) is the large scale dipolar configuration of magnetic field of parent galaxy, with dipole axes parallel to the rotation axes of host elliptical galaxy. There are many observational evidences that large-scale galactic magnetic fields can have dipolar configuration (for example in NGC4631 (Dumke et al., 1995), or in NGC5775 (Soida et al., 2011), and also in the halo of our Galaxy (Andreasyan & Makarov (1989), Han et al. (1997)). The magnetic fields of dipole configuration can be formed and evaluate, for example, in the result of Biermann battery effect ((Biermann, 1950)), in Active Galactic Nucleus (Lesch et al. (1989), Andreasyan (1996)). Partly in (Andreasyan (1996)) for the evolution of dipolar magnetic field we suggest a model of AGN in agreement with the cosmological conception of V.Ambartsumian. In agreement with this model from the nucleus of Active galaxy there is a permanent ejection of hot plasma, which expands in the fast rotating gaseous medium of the central part of galaxy. Because of the large differences between scattering time of expanding electrons and protons with the rotating medium, in every point of rotating medium the rotation velocity of scattered electrons and protons will correspond to the rotation velocity of their last scattering point and will be different. In the result of forming of circular electric currents in the central part of Active galaxies evaluates dipolar magnetic fields. At the present time there are a lot of observational evidences of existence of the large amount of neutral and ionized gas in the host elliptical galaxies (for example Morganti et al. (2003), Andreasyan et al. (2008)), and also of outflows in Radio galaxies ((Oosterloo et al., 2004)), which provides the conditions for the working of Biermann battery effect, and evolution of dipolar magnetic fields.

The second suggestion in Andreasyan (1983) was that the extragalactic radio sources are formed from relativistic plasma clouds, ejected from the central part of the optical galaxy and moving in large-scale dipolar magnetic field of parent galaxy. The behaviors of relativistic plasma cloud, ejected in the direction of the dipole axis, depends on the ratio Q of the kinetic energy density of the plasma to the magnetic field energy density,

(i) If the ratio Q is greater than unity ($Q > 1$, the kinetic energy density of the plasma is larger than the magnetic field energy density), the clouds of charged particles, expanding, travels large distances from the optical galaxy, carrying with them the magnetic field lines, as it takes place in many well known models. In this case we expect to observe the more elongated radio images (Fig. 1). The directions of the major axes of the radio images will be close to those of rotation axes or the minor axes of the optical galaxies. The magnetic field will be mainly parallel to the radio axes. It can be formed also radio lobes and hot spots near their outer edges, and also well collimated magnetic canals directed from the AGN to the lobs, which can assist for the formation of well collimated jets in case of the secondary permanent ejection of plasma lower energy density. Similar features we observe in extragalactic radio sources of FRII classes ((Fanaroff & Riley, 1974)).

(ii) If the ratio Q of energy densities is less than unity ($Q < 1$, the kinetic energy density of the plasma is less than the magnetic field energy density), the charged particles will move along the field lines of the dipole magnetic field of the galaxy. In the beginning of this process (in the younger radio sources) along the dipole axes will be observed the long, jet like features with relatively large opening angles, like to the jets classified as FRI type.

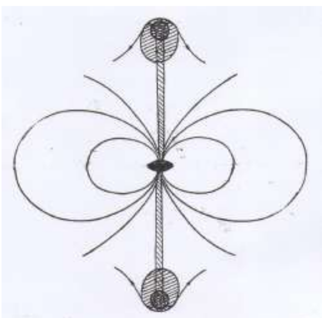

Figure 1. The ratio Q is greater than unity ($Q > 1$).

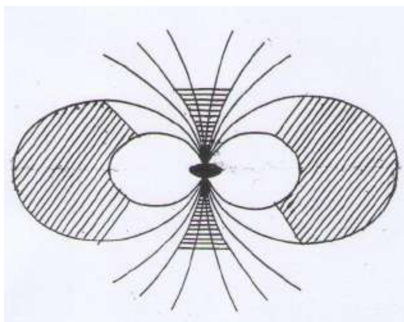

Figure 2. The ratio Q is less than unity ($Q < 1$).

Relativistic charged particles, moving along the field lines of the dipole, after some time will be trapped in the dipolar magnetic field. In result of this all particles finally will execute oscillations in the direction of magnetic lines between magnetic mirrors, and drift in a plane perpendicular to the dipole axis, as it takes place in the Van Allen belts of the Earth (Fig. 2). In this case will be formed less elongated radio sources with the radio axes perpendicular to the dipole axes, and correlated with optical major axes. Also we will observe mainly the edge darkened FRI type. As it was shown, in the case of $Q < 1$ it can be formed two type edge darkened radio sources; the relatively older Van Allen belts type sources, elongated perpendicular to the dipole axes, and the younger jet like radio sources along the dipole axes. These two types of extragalactic radio sources can be classified as FRI type, though they have different radio orientations relatively to the parent galaxies. It must be noted that such two types of relatively older and younger radio sources with different orientations can be observed near the same optical galaxy. Then we will observe misalignments of radio sources of different size scale, as was found by Appl et al. (1996), or the X shape radio sources (see for example Cheung (2007)).

It must be noted that in the literature some authors use the name "Jet" for radio sources that can have different forms and shapes, sometimes for objects that have not any elongation. Here, following to Bridle & Perley (1984), we will use the name "Jet" for the radio source that has the elongation parameter $K > 4$, where K is the ratio of the largest dimension of radio image to the perpendicular dimension. In Andreasyan (1983) parallel to the well known Fanaroff-Riley classification we bring also a simple classification of extragalactic radio sources by the elongation parameter K. In the case when the charged relativistic particles will be trapped in a dipolar magnetic field, the largest value of the parameter K can be obtained from the equation of the line of force of the dipole field. This ratio is near to 2.5. Thus, one can introduce a quantitative criterion for separating the extragalactic radio sources by their elongation parameter. So, following to this classification, there are:

1) Extragalactic radio sources for which $K > 2.5$ in the case of $Q > 1$ (FRII type), and for younger jet like radio sources of FRI type in case of $Q < 1$;

2) Extragalactic radio sources for which $K < 2.5$ in the case of relatively older Van Allen belts type sources ($Q < 1$).

As it will be seen in the next paragraphs there are some correlations between FR and this classification by the elongation parameter K. The statistical analyses of observational data were done parallel for the FR and K classification.

3. The Fanaroff-Riley Dichotomy of extragalactic radio sources

As it was mentioned above, the Fanaroff & Riley (1974) classification of extragalactic radio sources was done using the morphological features, the edge darkened-FRI, and edge brightened, relatively more luminous FRII types. Probably one can wait also some other morphological and physical differences between the different FR classes of extragalactic radio sources. The study of Fanaroff-Riley (FR) Dichotomy of extragalactic radio sources is very important for understanding and choosing of the mechanism of their formation and evolution. The FR Dichotomy is studying now very intensively, and there are found many other observational differences between the physical properties of these two morphological classes: in the total luminosity, in radio core powers, in ratio of core to lobe radio power, in the relationships between emission-line luminosity and radio power etc. (Zirbel & Baum (1995); Gopal-Krishna & Wiita (2000); Gendre et al. (2011), etc.). From the mechanism of formation of extragalactic radio sources, discussed above, it is clear that there can be a lot of other differences between different classes of extragalactic radio sources. Here we bring some other observational differences between the different FR types as well as between the types classified by their elongation parameter K.

4. Observational data

For this study we have used data for 267 nearby radio galaxies identified with elliptical galaxies brighter than 18th magnitude (sample1) (Andreasyan & Sol, 1999), and 280 extragalactic radio sources with known position angles between the integrated intrinsic radio polarization and radio axes (sample 2) (Andreasyan et al., 2002). For nearby radio sources, we have data: on the position angles of the optical images (oPA) of elliptical galaxies, found mainly from the Palomar maps, the position angles of radio image (rPA), angles between optical and radio axes (dPA), and FR classes taken from the literature. The radio galaxies were also classified as a function of their elongation parameter K using the published radio maps. For the objects of sample 2 also are found FR classes and have been determined elongation parameter K. In samples 1 and 2 we have 289 extragalactic radio sources with known both, FR classification and K parameters.

For statistical analysis we use also the data from sample 3, consisting of extragalactic radio sources from the CoNFIG (Combined NVSS-FIRST Galaxy) catalog of (Gendre et al., 2010), which includes radio charts and other observational data for 859 extragalactic radio sources. We used these radio charts to determine the radio elongation parameters K of the objects in sample 3 for which the FR classes are also given. There are 373 radio objects of this kind in sample 3; of these 52 are type FRI and 321, FRII. The low-frequency ($178MHz < n < 1.4GHz$) spectral indices also are given for many of the radio sources from sample 3 (57 of type FRI and 429 of type FRII).

Here we bring some results (physical and morphological differences in different classes of extragalactic radio sources) obtained in our early study (Andreasyan & Sol (1999); Andreasyan & Sol (2000); Andreasyan et al. (2002); Andreasyan et al. (2013)) as well as some new results. The samples 1 and 2 with the references can be found in Andreasyan (2012), while sample 3 is in Andreasyan et al. (2013)

5. The correlation of radio axis with the optical axis in nearby radio galaxies

Data from sample of 267 nearby radio galaxies were used to study the correlations of radio axes with the optical axes of parent galaxies. Were constructed histograms separately for radio galaxies classified by elongation (Fig. 3) and for radio galaxies with FR classes (Fig. 4). On the figures the difference between the radio and optical position angles (dPA) is laid out along the horizontal axis and the number of radio galaxies along the vertical axis. On the histograms we bring also the expected distribution of dPA. The continuous lines show the best fits obtained from primary distributions of intrinsic angles, described by a delta-function, taking into account the orientation effect. The fit of observed histograms of these relative orientations have been done using the method developed by Appl et al. (1996).

From the figures we found, that more elongated and FRII type radio galaxies are in most cases directed as minor axes or rotation axes of host elliptical galaxies, while the less elongated and FRI ones are directed perpendicular to these axes. This result is in a good agreement with conclusions of section 2. The weaker correlation for radio sources of FRI type can be explained by our mechanism. As it was shown, if $Q < 1$ It can be formatted two type radio sources; the relatively older Van Allen belts type sources (with $K < 2.5$), and the younger jet like radio sources along the dipole axes (with $K > 2.5$). These two types of extragalactic radio sources are classified as edge darkened FRI type, though they have different radio orientations relatively to parent galaxies

6. The ellipticity of elliptical galaxies identified with the different types of extragalactic radio sources

In the Sample 1 we have data of the optical ellipticity (E) of 154 elliptical galaxies. For all of them we have the elongation parameters K and for 95 - the Fanaroff-Riley classes. We use this data to study the distribution of ellipticities of parent optical galaxies for different FR types and for different classes of our K classification (Fig. 5).

From the Fig. 5 it is clear that the host elliptical galaxies of less elongated extragalactic radio sources and radio sources of FRI type have less ellipticity (E ≈ 1 to 2) than these of radio sources of large elongation and radio galaxies FRII type (E ≈ 3 to 4). The similar result we see for the

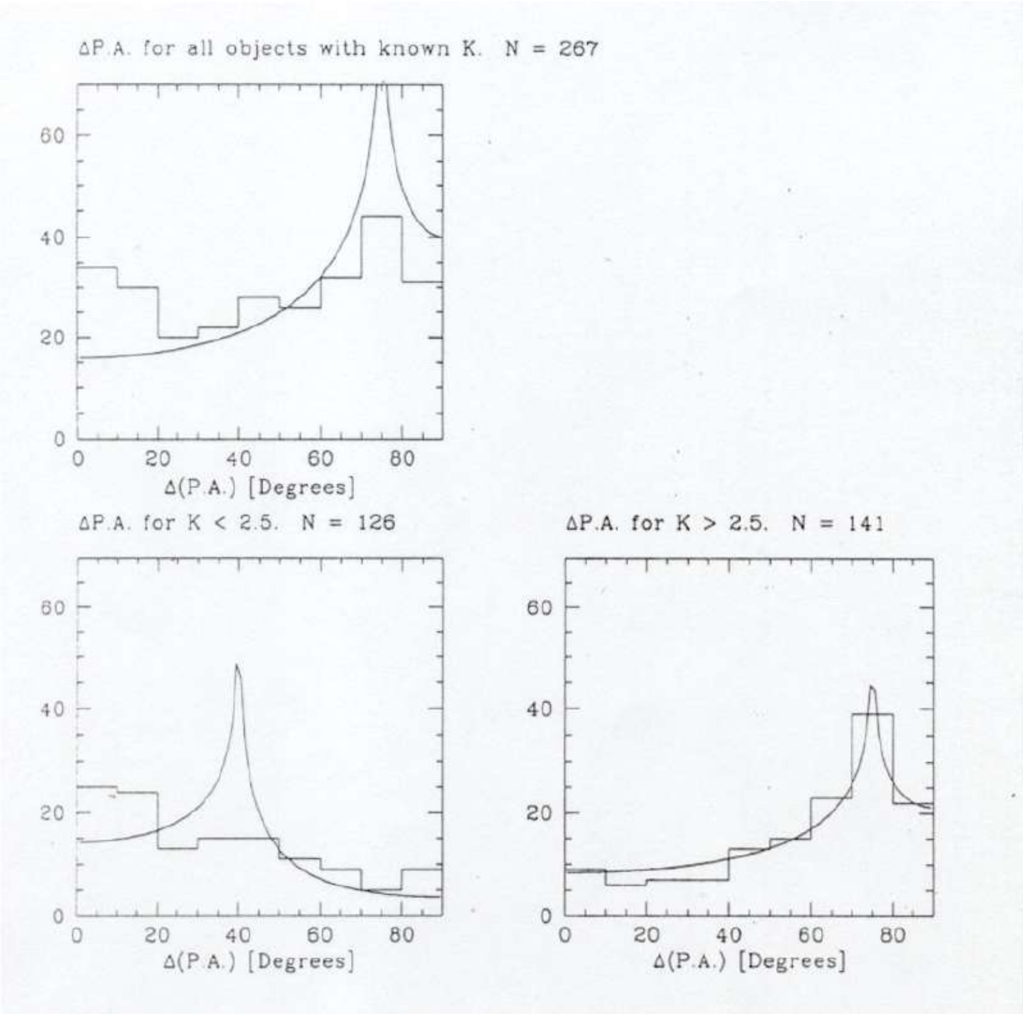

Figure 3. The distribution of (dPA) for K classes.

classification by K parameter. The fact that host elliptical galaxies of FRI type radio sources have less ellipticities can be explained in two ways: It is primordial and in some way is responsible for the formation of FRI types, or it is from the orientation effect. In both cases, the fact of different ellipticities of different FR types is interesting for the understanding of formation of radio sources.

7. The correlation of the radio polarization angle with the radio axes of extragalactic radio sources

The data of 280 extragalactic radio sources of sample 2 were used for the study of distribution of angles $\triangle(PA)$ between directions of integrated intrinsic radio polarization and the major axes for different type radio sources, classified by their elongation and FR classification. The histograms of angles between radio and polarization axes are shown in (Fig. 6) and (Fig. 7).

The fit of histograms for relative orientations also have been done using the method developed by Appl et al. (1996), taking into consideration the projection effects. The continuous line shows the best fits obtained from primary distributions of intrinsic angles described by a delta-function. This method describes rather well the case of elongated and FRII sources, which suggests that their intrinsic integrated polarization is perpendicular to their intrinsic major radio axes. Conversely the less elongated and FRI radio sources do not show any specific intrinsic angle and cannot be fitted by such a simple scenario. As the magnetic fields in optically thin synchrotron radio sources are perpendicular to the polarization of electric vector, the main result of this study is that integrated magnetic fields can be described as intrinsically aligned with major radio axes for elongated and FRII

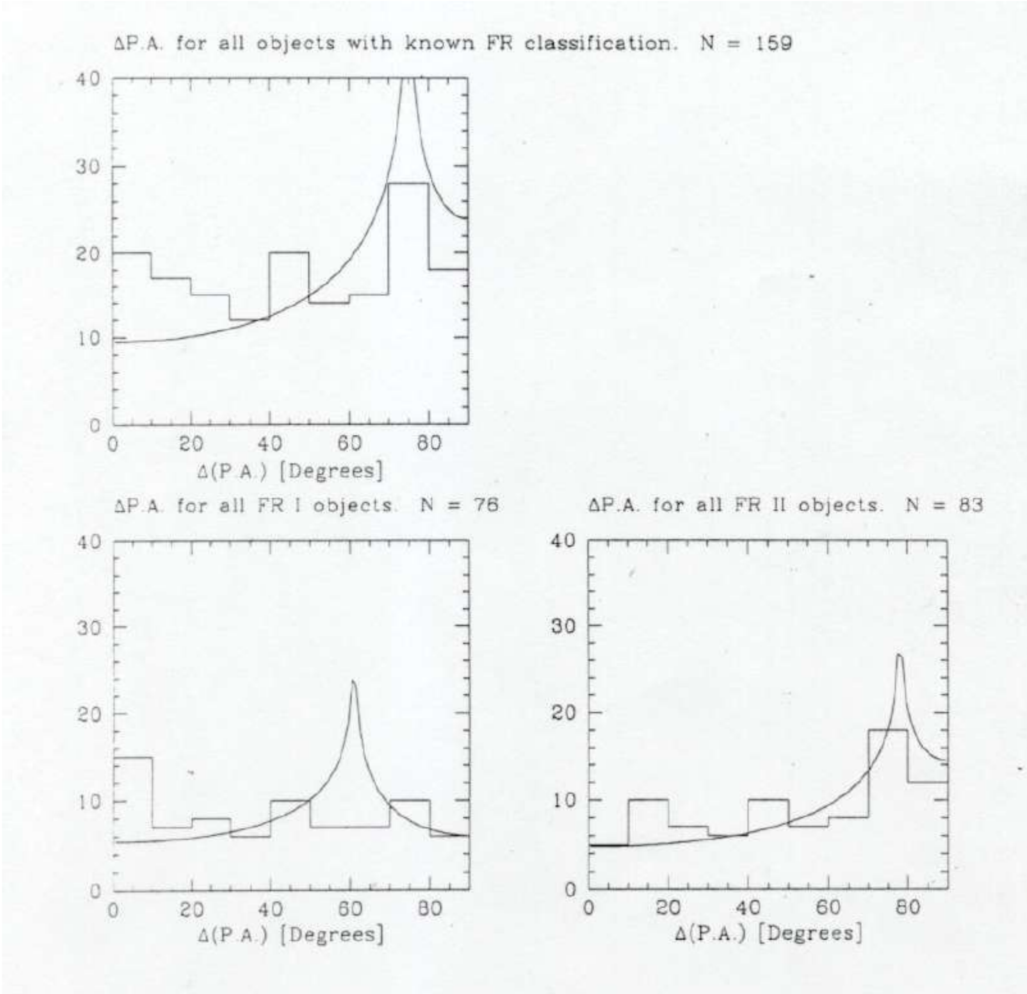

Figure 4. The distribution of (dPA) for K classes.

radio sources, while they are not correlated with radio axes for stocky and FRI radio sources.

8. Distribution of the elongation parameter of the extragalactic radio sources for the different FR classes

In this section we study the distribution of the elongations of the radio images for radio sources in the two FR classes. Data from samples 1, 2, and 3 are used to construct the distribution functions f (K) of the elongation parameter K which are shown in the following figures. Data from sample 1 were used to plot the distributions in Fig. 8. These figures show that the peak of the distribution of FRII radio sources is at about K ≈ 2.8 , while for the FRI sources the peak is at roughly K ≈ 2.2 . We believe that another important difference between the distributions of FRI and FRII extragalactic radio sources is that the FRI distribution has two peaks. For clarity of the differences between the FRI and FRII distributions the two distributions are plotted on a single scale in Fig. 9.

Roughly the same distribution is obtained if the data from sample 2 are used. Since, as noted above, sample 2 contains only 14 FRI radio sources, which differ from the FRI sources from sample 1, here we use the data from samples 1 and 2 together. The combined catalog lists 292 objects, of which 96 are FRI sources and 196 are FRII sources. Since the distributions of FRI and FRII extragalactic radio sources from the combined catalog do not differ greatly from the distributions of the objects in sample 1 (Fig. 1 and Fig. 2), in Fig. 10 we show just the distributions of the two types of radio sources in a single plot. A comparison of Fig. 2 (using 161 radio sources) with Fig. 10 (292 radio sources) shows that there are no great differences in the distributions of the elongation parameter K.

As pointed out above, the maximum of the distribution of the FRII radio sources lies at K $\approx$ 2.8

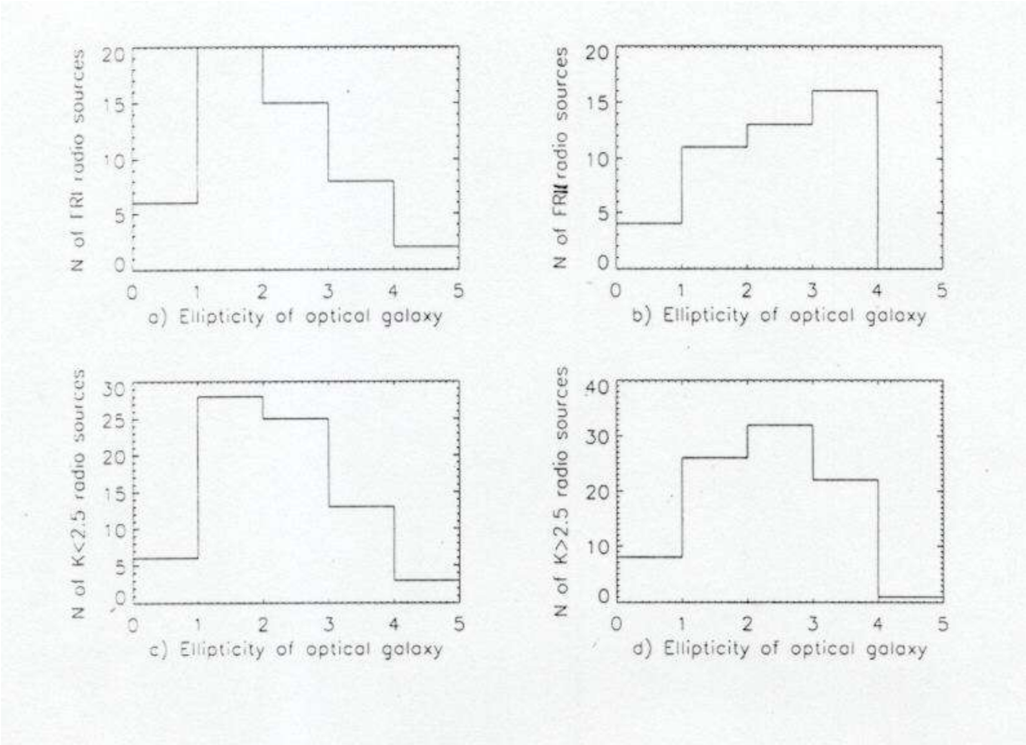

Figure 5. The ellipticities of optical parent galaxies for different FR types and for different classes of K classification.

and the peak for the FRI sources is at K $\approx$ 2.2 ; that is, the FRII radio sources are, on the average, more elongated than the FRI sources. Figure 10 also shows that, as in Figs. 1 and 2, there are two peaks in the distribution of the FRI extragalactic radio sources. Distributions of the elongation parameter K for the extragalactic radio sources have also been constructed using data from sample 3. Figure 11 shows the distributions for the FRI and FRII radio sources on a single scale.

Figure 11 shows that the distribution function for K of the FRI extragalactic radio sources from sample 3, as well as the distributions of the objects from sample 1 of the combined catalog (the combination of sample 1 and sample 2, Figure 10) have two peaks. The presence of two maxima in the distribution functions for the FRI radio sources can probably be explained if we assume that the FRI extragalactic radio sources can be divided into two subtypes that have different distributions of K with different maxima. Adding the two distributions yields the observed distribution function for these objects. It should be noted that we predicted the existence of two subtypes of FRI extragalactic radio sources before (Andreasyan, 2012). As stated in the Introduction, we have proposed (Andreasyan & Sol (1999), Andreasyan & Sol (2000); Andreasyan et al. (2002)) a mechanism for the formation of extragalactic radio sources involving features of the dynamics of clouds of relativistic electrons with different densities ejected from the central region of the parent galaxy in the assumed dipole magnetic field of the galaxy. According to this mechanism, depending on the ratio Q of the density of the kinetic energy of the relativistic electrons to the energy density of the magnetic field ($Q > 1$ or $Q < 1$), extragalactic radio sources of types FRI or FRII, respectively, can develop. However, in the second case two subtypes of the radio sources can be formed, where the radio brightness, as in FRI, decreases toward the edges of the radio image. These are young, streaming jet sources directed along the axis of the magnetic dipole and older residues of these formations which, as they move along the dipole magnetic field lines may have arbitrary orientations to the dipole axis. Here we use the term “radio jet” after Bridle & Perley (1984). Thus, a radio jet must have an elongated shape (in (Bridle & Perley, 1984) the elongation parameter $K > 4$). Older and wider formations may be much less elongated shapes than the radio jets. These two types of radio sources will be assigned to type FRI according to the Fanaroff-Riley classification, since the radio brightness decreases from the center toward the edge in them. However, they will have different distributions of the elongation parameter K and different orientations relative to the dipole axis. These are precisely the distributions of K

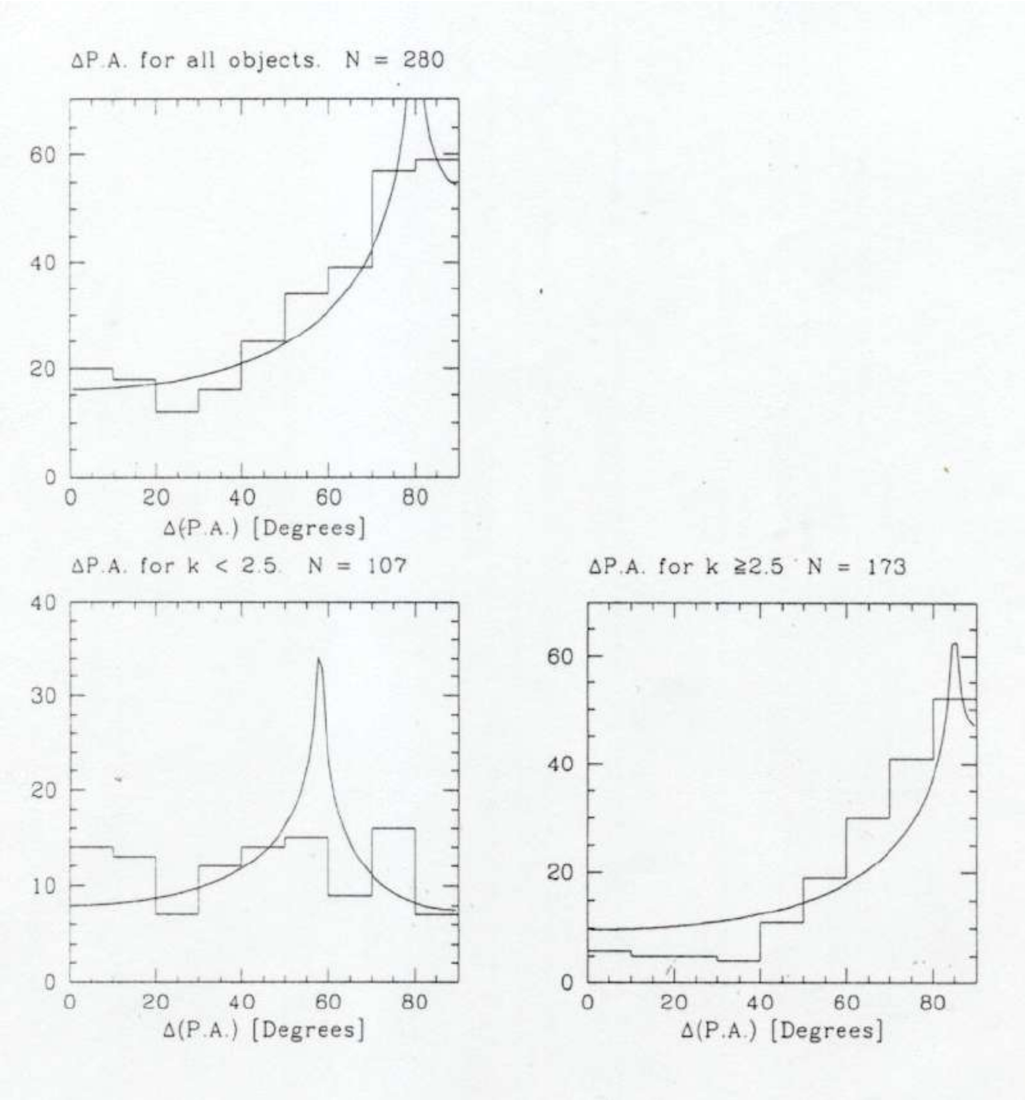

Figure 6. The ellipticities of optical parent galaxies for different FR types and for different classes of K classification.

obtained here for the extragalactic radio sources. It should be noted that these two subtypes of radio images with different elongations can be observed simultaneous in a single galaxy. Then different orientations of the radio images may be observed for different scales (Appl et al., 1996) and so-called X-shaped radio sources (currently under widespread discussion (Cheung (2007); Gopal-Krishna et al. (2012)) may develop.

9. Distribution of the spectral indices of extragalactic radio sources for the different FR classes

In this section we study the distribution of the spectral indices of the different FR types of extragalactic radio sources. Data on the spectral indices of 151 radio sources from sample 1 and 486 from sample 3 are used. These data are used to construct plots of the distributions of the spectral indices for the radio sources in the different FR classes. Figure 12 shows the distributions of the spectral indices of the extragalactic radio sources of the different types separately for samples 1 and 3. Figure 13 shows the distributions for the combined samples 1 and 3.

These figures show that the distributions of the spectral indices for the different FR classes of extragalactic radio sources are essentially the same. This can be seen for the objects from the separate samples 1 and 3, as well as for the objects after these samples are combined.

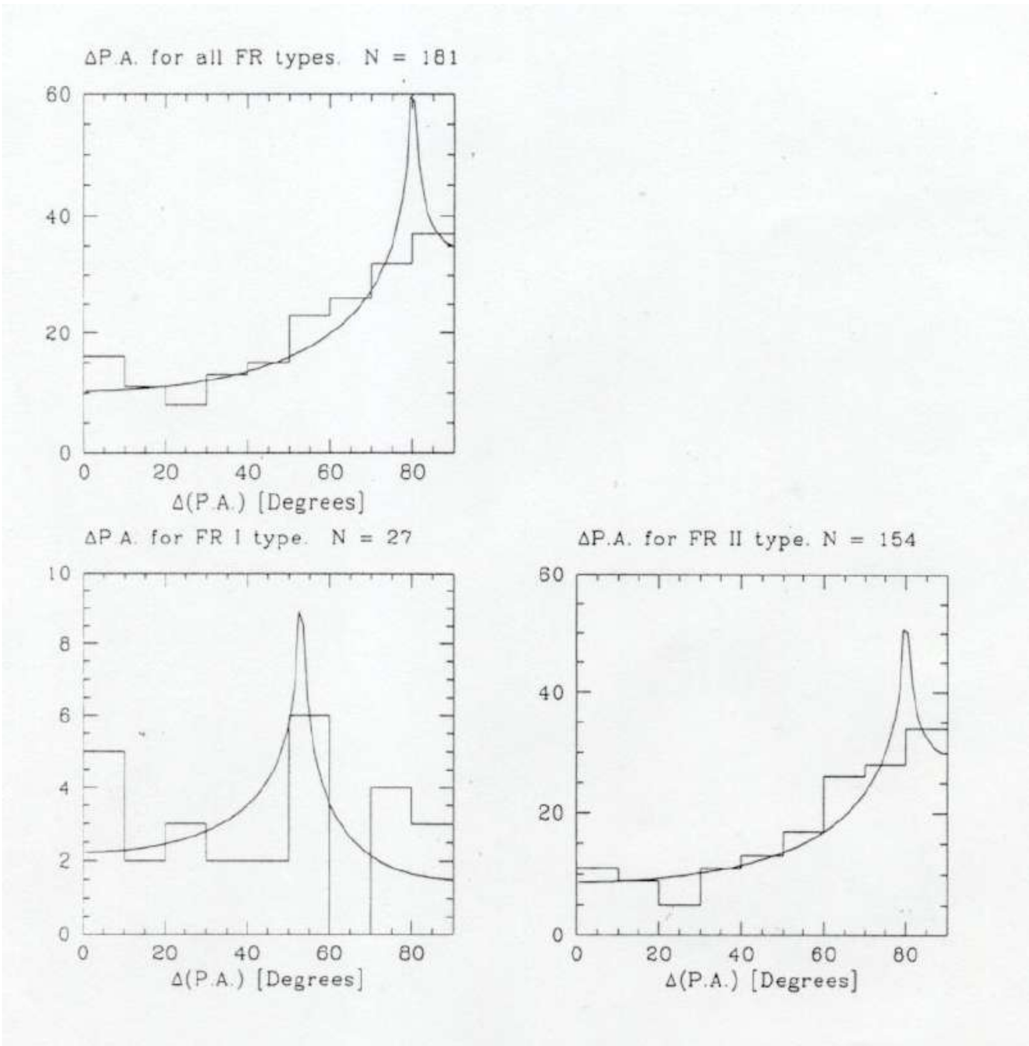

Figure 7. The ellipticities of optical parent galaxies for different FR types and for different classes of K classification.

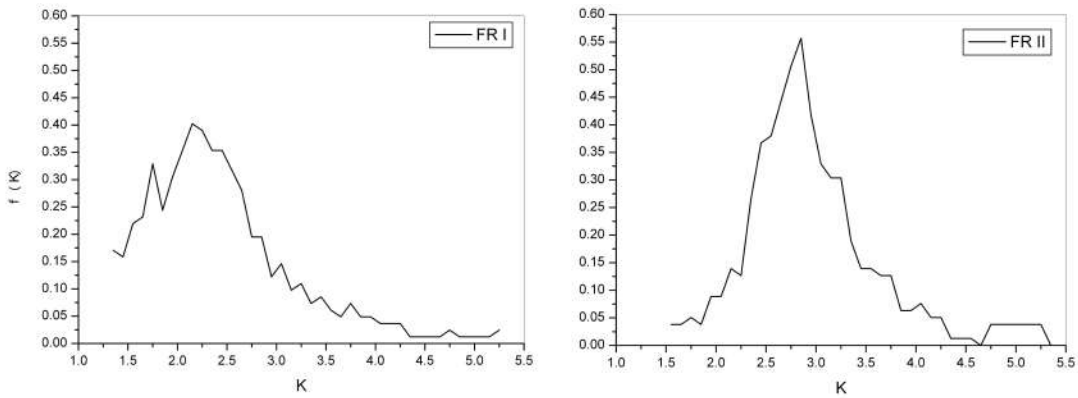

Figure 8. Distribution functions of the elongation parameter K for FRI (left panel) and FRII (right panel) extragalactic radio sources from sample 1.

10. Conclusions

The results, obtained above from the analyses of observational data are in good agreement with the suggested mechanism of formation of extragalactic radio sources. Almost all main observed physical and morphological properties of extragalactic radio sources can be qualitatively explained in terms of mentioned scenario, varying the parameter Q as well as the environment of radio sources. It must be

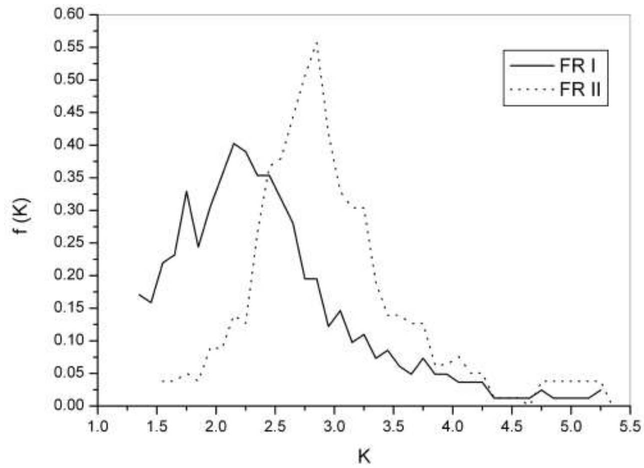

Figure 9. The distribution functions of the parameter K (using 82 FRI radio sources and 79 FRII radio sources).

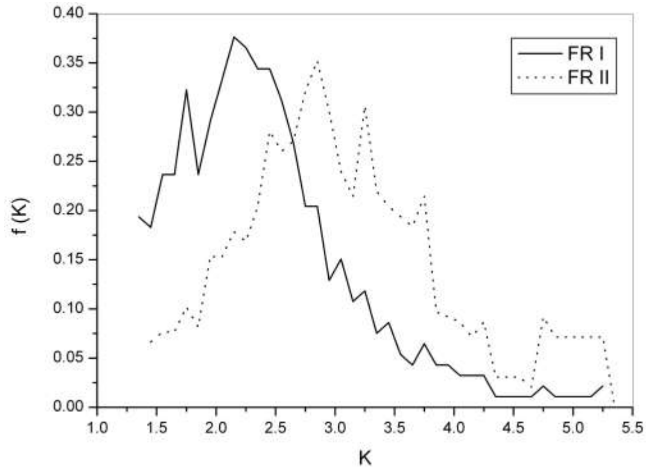

Figure 10. The distribution functions of the elongation parameter K for objects in the combined catalog (96 FRI radio sources and 196 FRII radio sources were used).

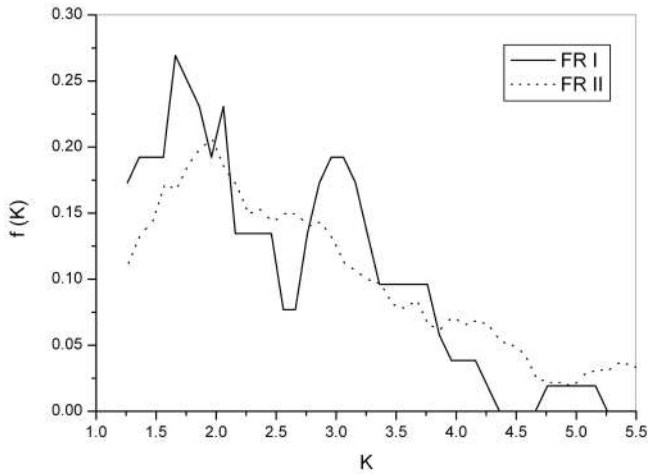

Figure 11. The distribution functions for the elongation parameter K for the objects from sample 3 (52 FRI and 321 FRII radio sources were used).

noted that mentioned above correlations of FR classification with physical parameters will be better,

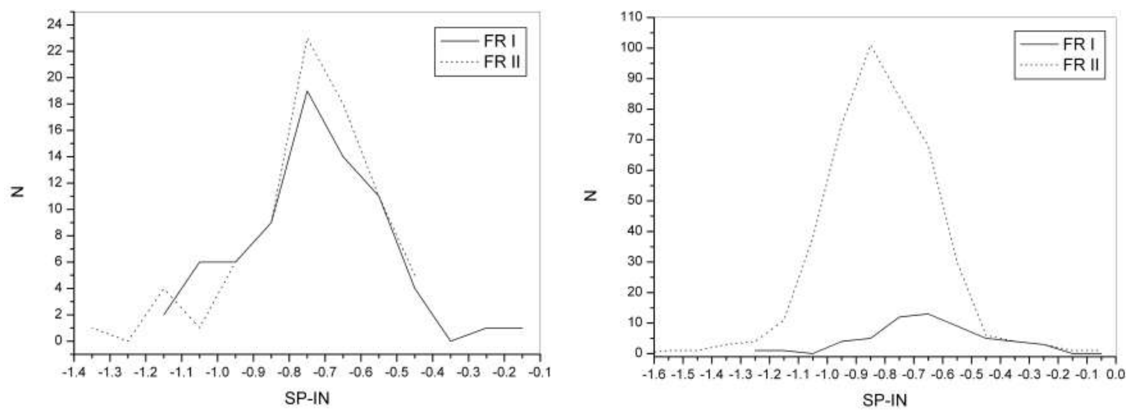

Figure 12. The distribution of the spectral indices of extragalactic radio sources from the two FR classes for samples 1 and 3.

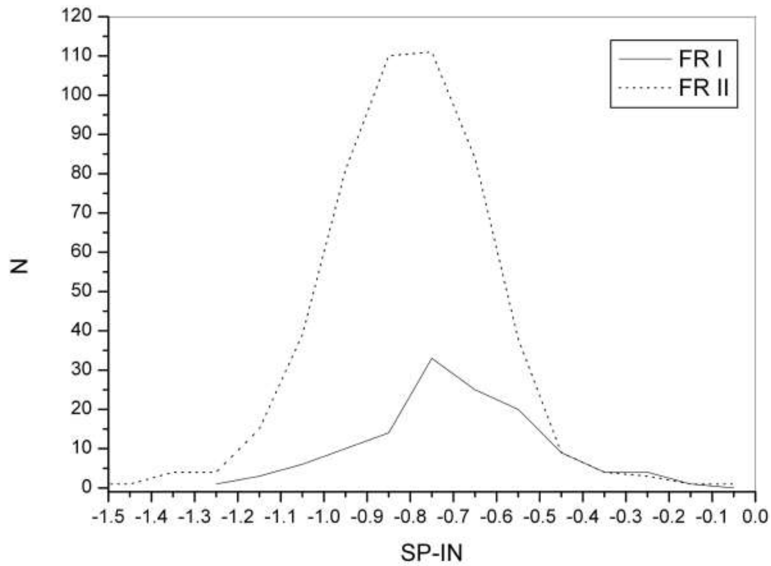

Figure 13. The distribution of the spectral indices of extragalactic radio sources from the different FR classes after samples 1 and 3 are combined.

if we divide the FRI type of extragalactic radio sources in two types:

(i) the more elongated jet like edge darkened radio sources

(ii) the less elongated ($K < 2.5$, Van Allen belts type sources) and probably more older edge darkened radio sources.

11. References

Ambartsumian, V. 1966, Transactions of the International Astronomical Union, Series B, 12, 578

Andreasyan, R. R., Hovhannisyan, M. A., Paronyan, G. M., & Abrahamyan, H. V. 2013, Astrophysics, 56, 382

Andreasyan, R. R. 2012, arXiv:1203.6549

Andreasyan, R. R., Martin, J.-M., & Paronyan, G. M. 2008, Astrophysics, 51, 454

Andreasyan, R. R., Appl, S., & Sol, H. 2002, Astrophysics, 45, 198

Andreasyan, R. R., & Sol, H. 2000, Astrophysics, 43, 413

Andreasyan, R. R., & Sol, H. 1999, Astrophysics, 42, 275

Andreasyan, R. R. 1996, Astrophysics, 39, 58

Appl, S., Sol, H., & Vicente, L. 1996, A&A, 310, 419

Andreasyan, R. R., & Makarov, A. N. 1989, Astrophysics, 30, 101

Andreasyan, R. R. 1983, Astrophysics, 19, 245

Biermann, L. 1950, Zeitschrift Naturforschung Teil A, 5, 65

Blandford, R. D., & Znajek, R. L. 1977, MNRAS, 179, 433

Bridle, A. H., & Perley, R. A. 1984, , 22, 319

Cheung, C. C. 2007, AJ, 133, 2097

Dumke, M., Krause, M., Wielebinski, R., & Klein, U. 1995, A&A, 302, 691

Fanaroff, B. L., & Riley, J. M. 1974, , 167, 31P

Gendre, M., Wall, J. V., & Best, P. N. 2011, Bulletin of the American Astronomical Society, 43, 317.02

Gendre, M. A., Best, P. N., & Wall, J. V. 2010, MNRAS, 404, 1719

Gopal-Krishna, & Wiita, P. J. 2000, A&A, 363, 507

Gopal-Krishna, Biermann, P. L., Gergely, L. Á., & Wiita, P. J. 2012, Research in Astronomy and Astrophysics, 12, 127

Han, J. L., Manchester, R. N., Berkhuijsen, E. M., & Beck, R. 1997, A&A, 322, 98

Lesch, H., Crusius, A., Schlickeiser, R., & Wielebinski, R. 1989, A&A, 217, 99

Luhmann, J. G. 1979, , 282, 386

Morganti, R., Oosterloo, T., Tadhunter, C., & Emonts, B. 2003, , 47, 273

Oosterloo, T. A., Morganti, R., Emonts, B. H. C., & Tadhunter, C. N. 2004, The Interplay Among Black Holes, Stars and ISM in Galactic Nuclei, 222, 353

Soida, M., Krause, M., Dettmar, R.-J., & Urbanik, M. 2011, A&A, 531, A127

Zirbel, E. L., & Baum, S. A. 1995, A&A, 448, 521

Saw-type shock fronts in several HII regions of southern hemisphere

A. L. Gyulbudaghian*

NAS RA V. Ambartsumian Byurakan Astrophysical Observatory (BAO), Armenia

Abstract

Radiation shock fronts at the heads of non adiabatic cooling jets are considered. Decay of these shock fronts leads to the origin of groups of HH objects, and of groups of bright condensations in the jets expelled from the nuclei of galaxies, e.g. from the nucleus of NGC5128. Several examples of saw-type radiation shock fronts, found in the Southern Hemisphere, are presented.

Keywords: *shock front: HH objects: galaxy NGC5128*

1. Introduction

Highly-collimated outflows, or jets, are rather common among young stars and active galaxies. Much work has been devoted to adiabatic jets, though there has been little attention to nonadiabatic or "cooling" jets. Radiation cooling due to collisional excitation and recombination can be important to the energy budget of jets associated with young stellar objects and HH objects. In Blondin et al. (1990) is presented detailed investigation of cooling jets, using numerical modeling for cylindrically symmetric non adiabatic jets. Stellar jets have been observed in many regions of low mass star formation. These jets are detected through low excitation line emission, e.g., [SII], which is believed to be originated in gas that has been heated in oblique shocks within a supersonic beam. These jets are well collimated, with opening angles of only a few degrees, and highly supersonic, with a Mach number of $M \sim 20$ for an assumed jet temperature of $10^4\,K$ (Blondin et al., 1990). These outflows are intimately connected with HH objects. Many, if not most, HH objects are in some way related to jets. Giving density ($10 - 100\,cm^{-3}$) and shock front velocity ($50 - 200\,km/s$), which are typical for stellar jets and HH objects, in Blondin et al. (1990) was received, that the cooling time of gas, heating by shock front, often is less than the dynamic age of these objects, hence they have a conclusion that suggestion about adiabatic gas is invalid, it is necessary to consider the radiation shock fronts.

2. Radiation shock fronts

Interpretation of HH objects using radiation fronts, as was suggested by Schwartz (Schwartz, 1975), gave good coincidence with observed lines ratio. Several HH objects are seen as evident bow shock fronts at the top of bright stellar jets. The calculations show (Blondin et al., 1989), that some of these complicating, often divided in cloudlets, emission objects can be associated with active surface in the head of stellar jets. The dynamic envelope at the head of jet often is transforming into several small condensations of high density, creating a group of emission objects, resembling a group of HH objects. When the envelope begins to be destroyed, the condensations, which are actually formed out of the same envelope, continue to be associated with the active surface of the jet. In Blondin et al. (1989) was obtained, that the evolution can lead to the separate emission condensations, which show a rather big difference in their own velocities, though they were formed from the same envelope. The similar mechanism of disintegration of the envelope can be due to the Rayleigh-Taylor instability, as a

*agyulb@bao.sci.am

DOI: 10.52526/25792776-2019.66.1-20

result of propagation of the jet through the gas medium having a high density gradient. It is possible to suppose that the jet at the edge of HH 2 recently has reached the region of low density, that is why the envelope of the jet was destroyed, creating several condensations with a high difference in their velocities (these condensations are forming now the object HH 2 itself) (Blondin et al., 1989). In Gyul'Budagyan (1984) we have considered the objects HH 1, HH 2 and HH 39, which are representing groups of condensations (the velocities of condensations in each group are rather different).We have received there, that in the center of inertia system the velocities of condensations in the same group originate from one center. This is in favor of mentioned above theory of formation of HH objects by decay of the envelope of the jet. If we suppose, that HH objects were obtained by decay of some bodies, then the values of velocities of these bodies, as was shown in Gyul'Budagyan (1984),are rather close to each other: 240 km/s for HH 1, 175 km/s for HH 2 and 218 km/s for HH39 (these velocities are close to the given above velocity of maximal shock front, $\sim 200\,km/s$). The condensations mean velocities in the center of inertia system are also close to each other: 63 km/s for HH 1, 71 km/s for H,2 and 114 km/s for HH 39 (Gyul'Budagyan, 1984). A case of existence of two differing by 200 km/s radial velocities in the object HH 46, was described in Dopita (1978). It is possible, that the object HH 46 consists of two condensations, which have not yet divided.

In the jet, ejected from the nucleus of the galaxy NGC5128, a group of emission condensations with remarkable difference in velocities is situated (Osmer, 1978). It is possible to imagine, that this group has also formed by decay of ionization front in the head of supersonic jet, ejected from the nucleus of the galaxy.

The morphology of supersonic jets (adiabatic or cooling) can be divided into several structures:the supersonic beam, a cocoon of shocked gas of the beam, shocked ambient gas and a leading bow shock. The term “jet” is used rather loosely, usually for describing of the whole structure, but sometimes for only the supersonic gas (Blondin et al., 1990). The prevailing property of the cooling gas (it is the surprising result of simulations) is the dynamic instability of dense envelope in the head of the jet. Fig.4 in Blondin et al. (1990) shows typical decay of the jet envelope due to dynamic instability. Inclined jet is entering into the beam with high density in the cocoon, forming a ring of more dense gas around the edges of the beam. It makes the cooling distance behind the jet shock front less at the edge of the beam, than in its center. Rapid cooling of ambient gas leads to the formation of a ring of dense matter in the post shock region, forming a hole, through which more tenuous, cooled gas is pushed away by the post shock pressure. When this hole is compressed, it behaves as de Laval nozzle, accelerating hot gas up to ultra sound velocities. During the process of acceleration of the envelope, Rayleigh-Taylor instabilities begin to grow, forming irregularities in the envelope (see Fig.4 in Blondin et al. (1990)). In Fig.4 from Blondin et al. (1990) it is possible to see different profiles of jet head, in Fig.4d that profile is saw-type. As is mentioned in Blondin et al. (1990), the age of such a profile is about 1500 years.

3. Saw-type shocks, found in Southern Hemisphere

During systematic inspection of high quality film copies of the ESO B, R, ESO/SRC J and EJ plates of Southern Hemisphere, we have found several saw-type shocks indifferent H II regions of Southern Hemisphere. In Table 1 the data on these shock fronts are summarized. In Table 1 in the first column the number of objects is given; in columns 2 and 3 – the coordinates of objects; in column 4 – the names of the stars, which are in the same distance as the objects;in column 5 – the distance to these stars, taken from (Gaia, 2018); in column 6 – the width of saw-type shock fronts.

From Table 1 we can conclude, that the smallest width is at object N 3, which is situated near the star with spectrum GO, and the biggest width is at the object 4, which is situated near the star with spectrum O5. If we suppose, that the shock fronts were ejected from the stars from Table 1, we can conclude, that the width of the shock front depends on the spectra – if the spectrum of the star is earlier, the width of the shock front is broader. In Fig.1 – Fig.4 we give the DSS2 R images of objects from Table 1.

Table 1. Saw-Type shock fronts, found in southern hemisphere

NN	$\alpha(2000)$	$\delta(2000)$	Star	Spectrs	Distance (pc)	Width (pc)
1	07 29 55	-46 53 55	HD61391	B9	140	2.1
2	07 31 03	-48 25 00			0.92	
3	17 00 52	-38 18 57	HD153330	GO	100	0.09
4	17 02 56	-37 41 50	SAO208356	O5	1280	4,5
5	17 03 03	-37 54 19				1.1
6	17 18 33	-38 33 33	HD156232	AOIV	270	0.48

References

Blondin J. M., Konigl A., Fryxell B. A., 1989, ApJL, 337, L37

Blondin J. M., Fryxell B. A., Konigl A., 1990, ApJ, 360, 370

Dopita M. A., 1978, ApJS, 37, 117

Gyul'Budagyan A. L., 1984, Astrophysics, 20, 75

Osmer P. S., 1978, ApJL, 226, L79

Schwartz R. D., 1975, ApJ, 195, 631

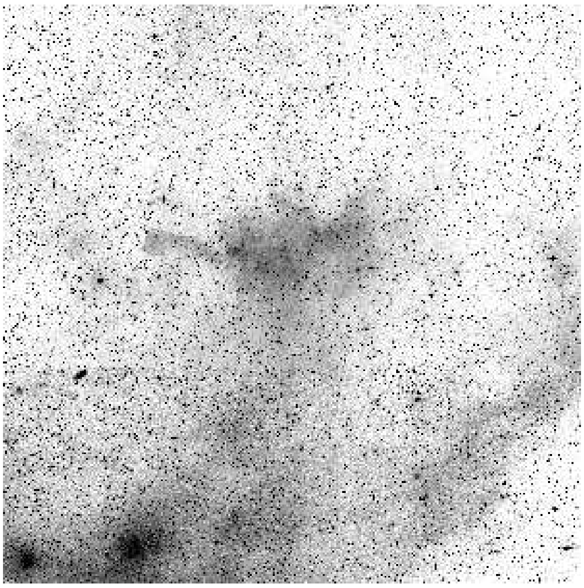

Figure 1. DSS2 R image, including the objects N 1 and N 2 from Table 1. Object N 1 is in the center of image, object N 2 is near the southern edge of image. North is to the top, south to the bottom. The sizes of image are $3^{\circ} \times 3^{\circ}$.

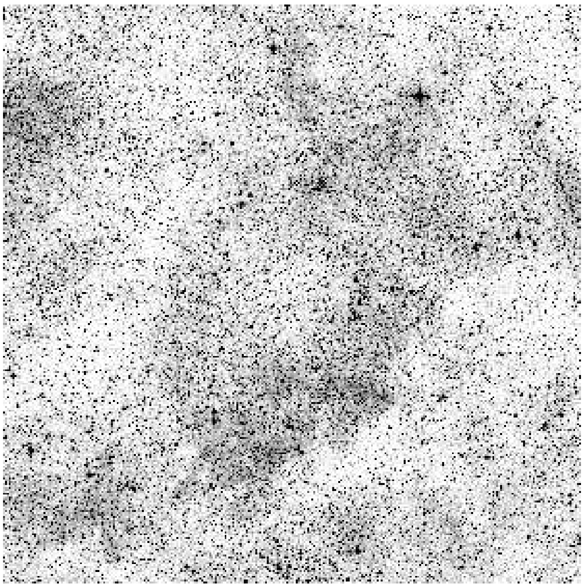

Figure 2. DSS2 R image of the object N 3 from Table 1. The object is situated a little to the south from the center. The sizes of image are $0.8^{\circ} \times 0.8^{\circ}$.

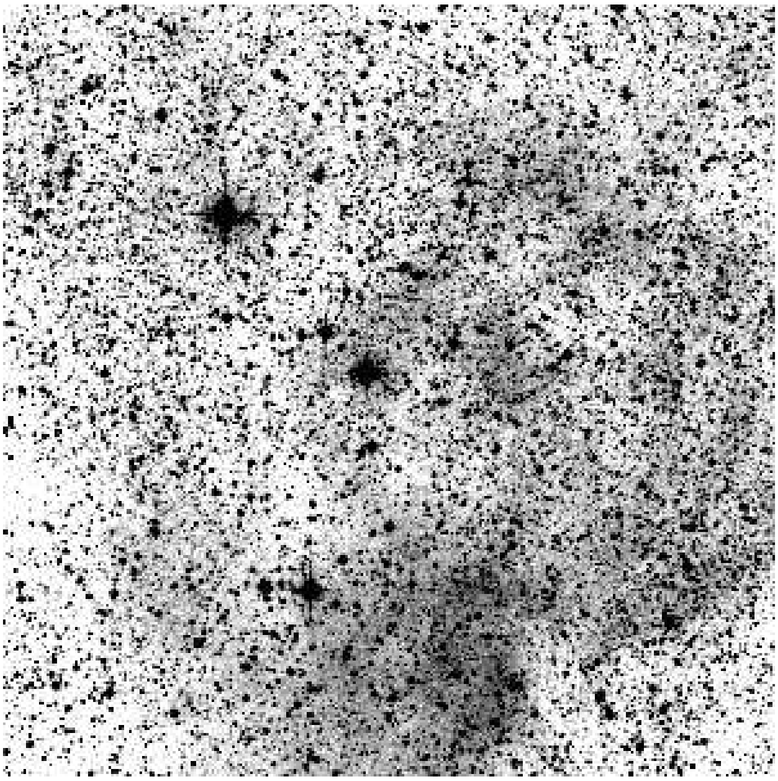

Figure 3. DSS2 R image of the object N 4 from Table 1. The object is situated a little to the SW from the center. The sizes of image are 0.4° × 0.4°.

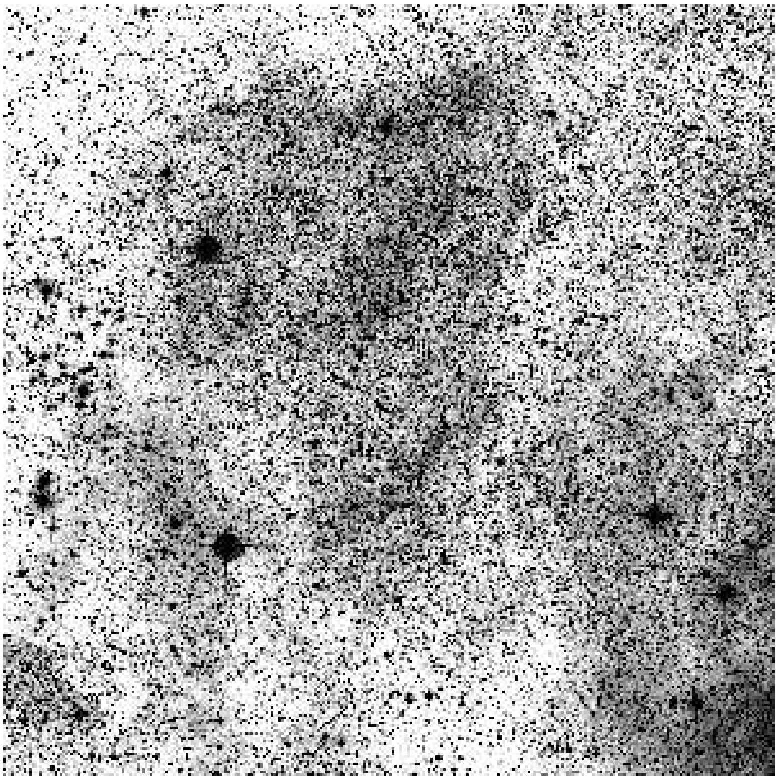

Figure 4. DSS2 R image of the objects N 5 and N 6. The object N 5 is situated to the N from the center, near the edge of the image. The object N 6 is also situated to the N from the center, but closer to the center than the object N 6. The sizes of image are 0.8° × 0.8°.

On the correlation between average velocities of galaxies and their average luminosities in the closest large clusters of galaxies

H. A. Harutyunian*[1], A. M. Grigoryan†[1], and A. Khasawneh‡[2]

[1]NAS RA V. Ambartsumian Byurakan Astrophysical Observatory (BAO), Armenia
[2]Royal Jordanian Geographical Center, Jordan

Abstract

The evolution of baryonic matter caused by the interaction with the dark energy carrier and its possible influence on the spectral characteristics of atoms are considered. Taking into account the earlier conclusion about the secular growth of mass of atomic nuclei and (perhaps) elementary particles due to interaction with the dark energy carrier, we reach a conclusion that in the course of evolution the spectral series of chemical elements should undergo blueshift. The longer is the evolution path, the higher is blueshift. We show here that galaxies of the two nearest clusters of galaxies exhibit a luminosity-redshift negative correlation which was expected in the frame of this deductive reasoning.

Keywords: *Galaxies: lumnosity, redshift, galaxies: giant, dwarf, metallicity.*

1. Introduction

It is evident that all the cosmic objects and their systems evolve in the course of time. They start their lives at any moment of time, transforming from a principally different state of a proto-object, continue their lives in the new stage and then finish it completing thus their life cycles. That is the natural evolution process. Scientists may argue about possible evolutionary scenarios, about the physical essence of a proto-object, or about what it turns into, but the very existence of the life cycle of any object can hardly be in doubt.

However, the axioms of modern physics and corresponding experimental data consider representatives of a distinct type to be unchangeable in the sense of evolution. Those are the elementary particles, atomic nuclei, and atoms themselves. There is no hint explicitly evidencing the change of these objects.In fact, even if these objects actually are subjects to secular change or in some way evolve, the corresponding changes are very difficult to detect. One should find some non-trivial way of considering the problem.

What kind of evolution can undergo quantum-mechanical objects, such as elementary particles or atomic nuclei? For modern physics, all the similar particles or nuclei are indistinguishable, i.e. if one replaces one proton with another no one will notice this replacement in any way. This is one of the fundamental axioms of quantum mechanics. On the other hand, it is well known that baryons change their mass being part of the atomic nucleus to make it stable enough for existing. Moreover, the same neutron or proton losses different amounts of mass being part of different nuclei. What does it mean? First, the baryon mass variation depending on the nucleus type might mean that any baryon is changeable and changes at least its mass obeying the surrounding physical conditions. Thus, one of the most essential issues necessary to clarify for answering the question on the evolution of quantum-mechanical objects is associated with the change of physical conditions in the course of time.

*hhayk@bao.sci.am, Corresponding author
†anigrigg@gmail.com
‡awni@yahoo.com

DOI: 10.52526/25792776-2019.66.1-25

2. Evolution of baryonic matter

In a series of papers Harutyunian (2014, 2017), Harutyunian & Grigoryan (2018), we consistently develop the idea of the unavoidability of the physical interaction between baryonic matter and the carrier of dark energy, settling within the framework of generally accepted laws of physics. This process should have several very significant physical consequences one has to take into account when considering the associated processes. In Harutyunian & Grigoryan (2018), we used the same ideology to interpret the growth of the Astronomical Unit (AU) hypothesizing that the dark energy carrier interacts with the baryonic matter at all scales and that the laws of thermodynamics remain valid in the process of interaction.

The logical chain based on our knowledge of physics leads then to the conclusion that owing to the mentioned interaction, if any, gradually decreases the nuclear binding energy. Such a result follows from the second law of thermodynamics if one takes into account that nuclear binding energy is a negative one and dark energy is a positive one. This means that due to the interaction of atomic nuclei with a carrier of dark energy, the latter receives a certain portion of energy and reduces the absolute value of the deficit of its energy. It is obvious, that we arrive at the same conclusion if we consider the interaction between gravitationally bound objects and the carrier of dark energy. As a primary result, in both cases, the predicted energetic change of baryonic objects gradually diminishes their stability. On the other hand, due to the decrease of nuclear binding energy one should expect an increase in nuclear mass, which results inan increase in the mass of all baryonic objects.

In Harutyunian & Grigoryan (2018), we attempted to calculate the Sun's mass change using the observational data concerning the value of the AU annual growth. To this end, we proceeded from the fact that instead of the speed of the Earth's removal from the Sun, which we predicted using the Hubble expansion rate for the scale under consideration, one observes a value of two orders of magnitude smaller, because of the increase in the mass of the Sun. This information is enough for calculating the necessary amount of the additional mass transformed from the dark energy storage into the ordinary matter. For the Sun's mass growth we got $\Delta M \sim 7 \times 10^{-11} M_{\odot}\, yr^{-1}$, which is equal to $4.5 \times 10^{15} g/s$. In energy units,it amounts to $4.05 \times 10^{36} erg/s$. One can compare this value with the Sun luminosity to obtain it in solar luminosities $\sim 1000 L_{\odot}$.

Remaining in this framework, one can mention another observational effect of the mass growth of atomic nuclei and elementary particles. One can predict this effect based on the famous formula giving the wavelength of spectral lines for hydrogen or hydrogen-like ions:

$$\frac{1}{\lambda_{mn}} = RZ^2 \left(\frac{1}{m^2} - \frac{1}{n^2} \right), \tag{1}$$

where R is the Rydberg constant:

$$R = \frac{\mu e^4}{8 \varepsilon_0^2 h^3 c}, \tag{2}$$

and $\mu = m_e M_n/(m_e + M_n)$ is the reduced mass of electron and nucleus, m_e and M_n are the masses of electron and nucleus. For the hydrogen atom $R = 1.09677583 \times 10^7 m^{-1}$. It is obvious that if increases either electron's, or nucleus' mass, or both of them, the Rydberg constant gets larger. It does mean, that owing to the gradual increase of the masses of elementary particles spectral lines should undergo blueshift.

Of course, the idea concerning the evolutionary blueshift is not new, it was developed more consistently in quasi-stationary cosmology. However, in the current paradigm, we can point out the mechanism of the mass growth, which we assume to be linked with the gradual mass birth due to the interaction between the ordinary baryonic matter and the carrier of dark energy. It seems that during the evolution of the baryonic Universe constantly works a self-consistent mechanism, transferring dark energy into the baryonic mass.

3. The cosmic objects' evolution rate depending on their mass

For evolutionary purposes, it is very important to know the consequences of the interaction between the carrier of dark energy and much larger cosmic objects. Physical intuition suggests that more massive objects are more difficult to be affected by dark energy than low-mass ones.Using the example of a spherical object,it is easy to verify this assumption. Such an object's gravitational potential energy is given by the following formula:

$$U = -G\frac{M^2}{R}. \tag{3}$$

It is evident, that the same physical justification used above for the gradual decreasing of the nuclear binding energy might be used here for the gravitational potential energy issue. Then one arrives at the conclusion that the absolute value of goes down in the course of time. Hence, one can see that in (3) either the numerator should reduce, or the denominator should enlarge.

We saw in the previous section that the mass increases due to a decrease in the binding energy in the microworld. Therefore, one can conclude, that the size of the object gets larger faster than the square of its mass. If we consider the Universe as such an object, we can conclude that its size and mass are growing. The first conclusion is obvious since the Universe is expanding. The second one follows from our deduction on the mass growth in general. There is also another cosmological interpretation for this: the much younger Universe could not have been expanding if it would have the same mass as today.

For checking the influence of dark energy on the baryonic objects of different masses one can use the ratio of the gravitational and dark energy densities. Denoting dark energy density by ρ_{DE} and the mass density of the object by ρ_M, one can find that within the radius these energies ratio is

$$k_E = \frac{U}{\frac{4\pi}{3}R^3\rho_{DE}} \approx \frac{M}{R}\frac{\rho_M}{\rho_{DE}}. \tag{4}$$

It is obvious from (4) that the more massive are objects, the bigger is the ratio if only the baryonic objects' density does not decrease inversely proportional to the square of the radius or faster. The objects belonging to the same type (stars or galaxies or planets),such dependence is not observed.What does it mean? This dependence can be interpreted in favor of the fact that massive objects evolve more slowly, that is, the more accumulated baryon mass, the more difficult it is for dark energy to carry it along the path of evolution.

Therefore, one can assume that objects of different masses formed together apparently would be at different stages of evolution. It does mean that for testifying the consistency of the conclusions made above, one should find the appropriate objects.

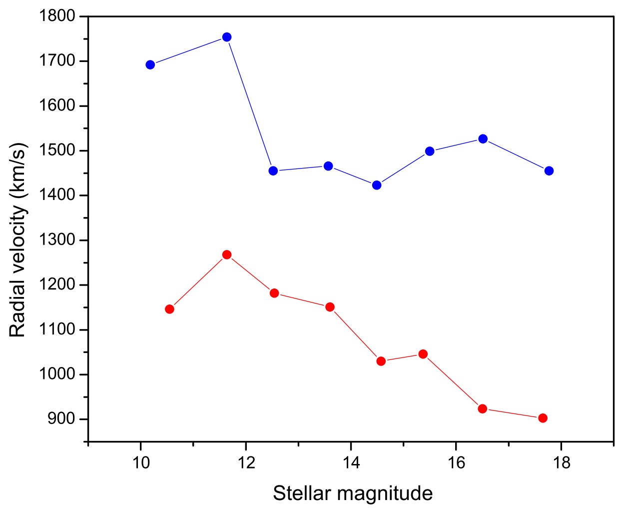

Figure 1: Radial velocities vs. stellar magnitudes for Virgo (red line) and Fornax clusters (blue line). The correlation coefficient for the 400 Virgo galaxies is -0.90. For the Fornax 125 galaxies, the correlation coefficient is -0.64.

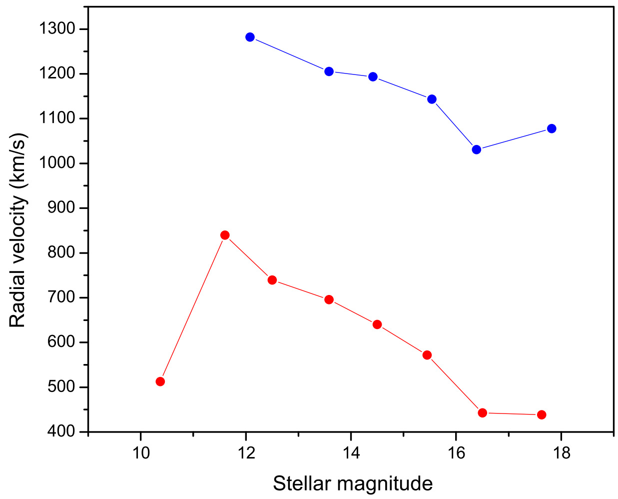

Figure 2: Radial velocities vs. stellar magnitudes for galaxies from Virgo (red line) and Fornax (blue line) clusters with radial velocities lower than the average. The correlation coefficient for the Virgo galaxies is -0.60 and for Fornax galaxies is -0.91.

4. Galaxy clusters

Galaxy clusters are the best laboratories to test the conclusions derived in the previous sections of this paper. The point is that the masses of dwarf and giant galaxies can differ up to a million times. Therefore, using galaxies of various luminosities belonging to the same cluster, we can compare their baryonic matter properties, which we believe are depending on the length of the evolutionary path.

One such difference between the features of the baryonic matter of dwarf and giant galaxies is well known. We are talking about the dependence of luminosity-metallicity or, which is the same, mass-metallicity.A correlation between the galaxies metallicity and blue luminosity was demonstrated by Garnett & Shields (1987) and extended by various authors (Brodie & Huchra, 1991, Skillman, 1989, Zaritsky et al., 1994) to include a range of Hubble types and to span over 11 magnitudes in luminosity and 2 dex in metallicity.

Traditional cosmology explains this dependence as the selective loss of metals from galaxies with shallow potential wells via galactic winds, an idea rst introduced by Larson (1974). Nevertheless, this mechanism is not satisfactory for explaining the observed correlation. Unfortunately, one needs to construct far too artificial models for reaching the observed metallicities for the given baryonic masses.

When interpreting the mass-metallicity correlation in the frame of the paradigm we develop here,one has a much more unambiguous physical mechanism leading to the formation of different chemical abundances in the galaxies of different masses.The longer the evolution, the lower metallicity in the baryonic matter.

Indeed, taking into account the conclusion about the evolution rate dependence on the mass of a galaxy one arrives at the conclusion that the baryonic matter in dwarf galaxies easier enriches with light elements including the hydrogen. It decreases the metallicity of dwarf galaxies much rapidly than in the giant ones. So, the most essential result one derives from this logical chain is that the rate of evolution of dwarf galaxies is higher, and therefore they undergo longer evolution in course of the same time than giant ones. The longer is the evolution, the less is the metallicity.

On the other hand, as was mentioned in the previous paragraph the mass increase of atomic nuclei leads to the blueshift of the spectral series of the atoms. It does mean, that the longer is the evolution process, the shorter should be spectral lines wavelengths. If this logical chain is correct, one should expect that the redshifts of dwarf galaxies are smaller than those of giants. We checked it for two clusters, using the data published for the famous galaxy clusters in Virgo (Binggeli et al., 1985)

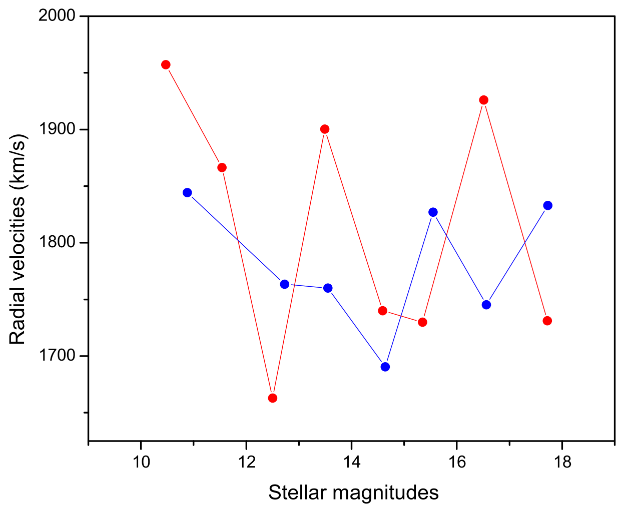

Figure 3: Radial velocities vs. stellar magnitudes for galaxies from Virgo (red line) and Fornax (blue line) clusters with radial velocities higher than the average. The correlation coefficient for the Virgo galaxies is -0.04 and for Fornax galaxies is -0.06.

and Fornax (Ferguson, 1989). Only the galaxies marked as cluster members have been used for the analysis. All the data is taken from the mentioned papers, and no changes or corrections had been done for the data improving purposes.

In order to verify the result obtained above concerning the possible blueshift of spectral lines caused by the baryonic matter evolution, we first constructed the luminosity distribution of galaxies for both lists separately. Then the galaxies have been divided into bins of one stellar magnitude width. For each bin, the average redshift and average magnitude of galaxies were calculated. In Fig. 1 the results of these calculations are shown. At first glance, it can be seen that there is a tight negative correlation between luminosities and redshifts. The correlation coefficient for the 400 Virgo galaxies amounts -0.90, which is really high. If one excludes the first point, which refers to the most massive galaxies, one finds for the correlation coefficient the value of -0.98. For the Fornax 125 galaxies, the correlation coefficient is -0.64, which is also a rather high bat not as significant as for the Virgo cluster.

Next, we divided the samples of galaxies into two subsamples – having a speed lower and higher than the average of the cluster. It is interesting that the two subsamples have different behavior. The graphs are shown in Fig. 2 and Fig. 3. In both clusters, the correlation we are looking for is sharper for the galaxies possessing speeds lower than the average for the given cluster. The Virgo sample gives for the correlation coefficient -0.60 (-0.99) for the first subsample and -0.04 for the second subsample. The same coefficients for the Fornax subsamples are -0.91 and -0.06, correspondingly.

One can see that the galaxies of our neighboring two large clusters show the expected luminosity-redshift correlation. This correlation is caused mainly by the galaxies possessing redshifts which are lower than the cluster average redshift. In other words, the correlation is well noticeable for galaxies “blueshifted” with regard to the cluster mean recession speed.

5. Conclusion

Owing to the interaction with dark energy carrier the baryonic matter undergoes evolution process, changing some structural parameters, which can be manifested through observational shreds of evidence. We consider here the possible physical changes of atomic nuclei and predict blueshift of spectral series due to the evolutionary changes. Actually, one of the predicted changes is the well-known mass-metallicity relation observed for galaxies, which finds a completely new interpretation. In order to verify or reject the second one, we were looking for a correlation between galaxy luminosities and redshifts.

Analyzes of the relevant data for the Virgo and Fornax clusters alow to exhibit the expected correlation. It is interesting that galaxies of the chosen samples fit the predicted correlation at the expense of the subsample having lower speeds than the average for the cluster redshift. In both cases, galaxies having larger the average redshift do not show any correlation. We believe that this issue has some physical meaning which will be considered later.

References

Binggeli B., Sandage A., Tammann G. A., 1985, AJ, 90, 1681

Brodie J. P., Huchra J. P., 1991, ApJ, 379, 157

Ferguson H. C., 1989, AJ, 98, 367

Garnett D. R., Shields G. A., 1987, ApJ, 317, 82

Harutyunian H. A., 2014, in "Instability and Evolution of Stars", Proceedings of the Byurakan-Abastumani Colloquium dedicated to Ludwik Mirzoyan's 90th anniversary, Eds.: Harutyunian, H. A.; Nikoghosyan, E. H.; Melikian, N. D.. pp 89–93

Harutyunian H. A., 2017, Astrophysics, 60, 572

Harutyunian H. A., Grigoryan A. M., 2018, ComBAO, 65, 268

Larson R. B., 1974, MNRAS, 169, 229

Skillman E. D., 1989, ApJ, 347, 883

Zaritsky D., Kennicutt Robert C. J., Huchra J. P., 1994, ApJ, 420, 87

Communications of BAO, Vol. 66, Issue 1, 2019, pp. 31-40

Observations and Study of Byurakan-IRAS Galaxies: Summary

G. A. Mikayelyan*, A. M. Mickaelian, H. V. Abrahamyan, G. M. Paronyan, and M. V. Gyulzadyan

NAS RA V. Ambartsumian Byurakan Astrophysical Observatory, Armenia

Abstract

The paper is a summary and general analysis of optical spectroscopic data on 257 Byurakan-IRAS Galaxies (BIG objects) obtained with the BAO 2.6-m, SAO 6-m, OHP 1.93-m telescopes and taken from SDSS spectroscopic database. 149 star-formation regions galaxies, 42 galaxies with active nuclei, and 28 galaxies with a composite spectrum were identified. The spectra of 21 galaxies show signs of emission, but without the possibility of more precise determination of their activity type, 13 galaxies appear to have star formation rates that do not exceed normal, and 3 are absorption galaxies.

Keywords: *galaxies: spectra: active galactic nuclei: starburst galaxies*

1. Introduction

The InfraRed Astronomical Satellite (IRAS) was the first space-based observatory that performed a survey of the entire sky at infrared (IR) wavelengths. It mapped 96% of the sky in four bands: 12, 25, 60, and 100 μm. IRAS point sources are published in two large catalogues, IRAS Point Source Catalog (PSC; IRAS 1988) and IRAS Faint Source Catalog (Moshir et al., 1990). Though FSC contains fainter sources and is deeper, however, it misses the Milky Way area b < |10°|. In 2015, Abrahamyan et al. (2015) cross-correlated these two catalogues and the Combined Catalogue of IRAS point sources was published containing 345,163 sources. However, many of these sources are still left without any identification, that is, their physical nature remains unclear. Thus, the question of identifying these objects in the visible and obtaining optical spectra for classifying them has arisen. This may lead to a revision of previous ideas regarding the relative distribution of various types of galaxies. About 75,000 of them are believed to be starburst (SB) galaxies, still undergoing their star-formation phase. IRAS sources have increased our understanding of objects in Our Galaxy (stars and nebulae), especially star formation processes in galaxies, activity of galactic nuclei, and galaxy interactions. In particular, there is a special interest in the discovery of galaxies with high IR luminosity: LIRG (Luminous InfraRed Galaxies), ULIRG (Ultra-Luminous InfraRed Galaxies), and HLIRG (Hyper-Luminous InfraRed Galaxies) (Sanders and Mirabel, 1996). Latest IR surveys have shown that ULIRGs are vastly more numerous at high redshifts. Understanding the physics and evolution of ULIRGs, the contribution of high redshift ULIRGs to the cosmic IR background and the global history of star formation, and the role of ULIRGs as diagnostics of the formation of massive galaxies and large-scale structures are important questions still to be clarified. Though a number of recent IR (especially near-IR and mid-IR) surveys appeared: 2MASS (Cutri et al., 2003, Skrutskie et al., 2006); AllWISE (Cutri et al., 2013); AKARI (Ishihara et al., 2010, Yamamura et al., 2010), IRAS catalogues are still useful for studies at far-IR (FIR) wavelengths (60 and 100 μm), i.e., for extragalactic studies, and IRAS galaxies provide homogeneous samples of IR-selected AGN and SB.

There have been a number of studies on identifications of IRAS galaxies since the release of IRAS catalogs: IRAS Revised Bright Galaxy Sample (Sanders et al., 2003); Far-InfraRed (FIR) sources

*gormick@mail.ru, Corresponding author

DOI: 10.52526/25792776-2019.66.1-31

(Bertin et al., 1997); IRAS galaxies towards the Boötes void (Strauss and Huchra, 1988); IRAS point sources in the area of Fornax, Hydra I and Coma clusters (Wang et al., 1991); IRAS 1.2 μm survey (Fisher et al., 1995); IRAS galaxies in Virgo cluster area (Yuan et al., 1996); and some others.

About half of all IRAS sources are still not identified and there is a need for optical identifications. Since 1995, a project of optical identifications has been carried out in the Byurakan Astrophysical Observatory (Mickaelian, 1995), in order to detect new galaxies with bursts of star formation in their central regions (SB, or Starburst galaxies) (Weedman et al., 1981), galaxies with active nuclei (AGN, active galactic nuclei) (Ambartsumian, 1958), interacting pairs, and galaxies with high IR luminosity (ULIRG, Ultra-Luminous IR Galaxies), which resulted in revealing 1178 galaxies and 399 stars, named Byurakan-IRAS Galaxies (BIG) (Mickaelian and Sargsyan, 2004) and Byurakan-IRAS Stars (BIS) (Mickaelian and Gigoyan, 2006), respectively. Identifications using low-dispersion spectra of the First Byurakan Survey (FBS or Markarian survey) (Markarian et al., 1989) and its digitized version, DFBS (Mickaelian et al., 2007, Massaro et al., 2008) guaranteed better selection of optical counterparts compared to other identification works.

BIG objects have been studied spectroscopically using BAO 2.6 m (Mickaelian et al., 2003, Sargsyan and Mickaelian, 2006), Special Astrophysical Observatory (SAO, Russia) 6 m (Mickaelian et al., 1998, Balayan et al., 2001), Observatoire de Haute-Provence (OHP, France) 1.93 m (Mickaelian, 2004) telescopes and the Sloan Digital Sky Survey (Abolfathi et al., 2018) (Mickaelian et al., 2018). Altogether 255 BIG objects have been studied and classified. The spectroscopic studies of BIG objects facilitate the concurrent solution of several problems. These problems range from confirming the extragalactic nature of objects and determining their redshifts to detailed analyses of the objects' structure, which proved to be of greatest interest, such as galaxies with enhanced IR luminosities and/or with nuclear or starburst activity.

2. BIG Sample

A total of 257 spectra were obtained: 56 with the BAO telescope, 54 with the SAO telescope, 64 with the OHP telescope and 83 from the SDSS. The list of all objects with their parameters are given in Table 1. The columns list spectra source (telescope name or SDSS), the IRAS names for the objects, stellar magnitudes close to V (for objects from SDSS the r band was taken), the radial velocities (v_r) determined from the emission z (and calculated using the relativistic formula), the corresponding distances of the objects calculated for $H = 71\ km/(s\times Mpc)$, the absolute stellar magnitudes (M), the redshifts determined from the emission lines (z_{em}), and the type of activity of the objects (":" denotes objects with uncertain classifications).

Table 1: **The list of all observed BIG objects with their parameters**

IRAS source	**m$_V$**	**Spectra source**	**z$_{em}$**	**v$_r$** (km/s)	**R** (Mpc)	**M**	**Activity type**
03304+8456a	16.8	OHP 1.93m	0.0509	14868	209	-19.80	HII
03304+8456b	16.4	BAO 2.6m	0.0500	14625	206	-20.16	Abs
03333+7851	15.0	OHP 1.93m	0.0561	16347	230	-21.81	HII
03347+7748	15.5	OHP 1.93m	0.0346	10209	144	-20.29	Composite
03386+7909	15.9	OHP 1.93m	0.0559	16313	230	-20.91	Sy2
03424+8424	16.0	SAO 6m	0.0744	21492	303	-21.41	LINER:
03424+8713	15.4	BAO 2.6m	0.0249	7365	104	-19.67	HII
03485+7703	15.6	OHP 1.93m	0.0701	20281	286	-21.68	HII
04033+6942	15.9	OHP 1.93m	0.0161	4803	68	-18.25	LINER
04079+7033	14.5	OHP 1.93m	0.0132	3934	55	-19.22	HII
04140+7448	16.0	OHP 1.93m	0.0338	9972	140	-19.74	AGN
04183+7457	14.7	OHP 1.93m	0.0325	9589	135	-20.95	Composite
04574+7639	17.1	BAO 2.6m	0.1209	34081	480	-21.29	Em
05097+7954	15.2	OHP 1.93m	0.0570	16602	234	-21.64	HII

Table 1 – continued from previous page

IRAS source	m_V	Spectra source	z_{em}	v_r (km/s)	R (Mpc)	M	Activity type
05126+6516	15.4	OHP 1.93m	0.0402	11824	167	-20.71	HII
05196+7257	17.4	OHP 1.93m	0.1030	29303	413	-20.68	Sy2
05214+7741	16.3	OHP 1.93m	0.0769	22194	313	-21.17	AGN
05229+6826	14.5	OHP 1.93m	0.0166	4950	70	-19.72	HII
05275+6600	16.0	OHP 1.93m	0.0306	9037	127	-19.52	AGN:
05395+7550	15.0	OHP 1.93m	0.0248	7342	103	-20.07	HII
05401+6435	15.2	SAO 6m	0.0539	15735	222	-21.53	HII
05475+7449	16.0	OHP 1.93m	0.0515	15061	212	-20.63	Composite
05577+6141	16.1	OHP 1.93m	0.0306	9034	127	-19.42	Em
06022+7559	16.8	OHP 1.93m	0.0817	23509	331	-20.80	HII
06028+6734a	15.9	BAO 2.6m	0.0169	5015	71	-18.33	HII
06028+6734b	15.9	BAO 2.6m	0.0168	4983	70	-18.31	HII
06038+6239	14.4	SAO 6m	0.0413	12134	171	-21.76	Norm.
06261+7818a	18.4	BAO 2.6m	0.0939	26855	378	-19.45	HII
06261+7818b	17.4	BAO 2.6m	0.0940	26883	379	-20.48	LINER:
06273+6858a	17.2	BAO 2.6m	0.0664	19252	271	-19.96	Em
06273+6858b	16.4	OHP 1.93m	0.0665	19299	272	-20.77	HII
06273+6858c	15.7	OHP 1.93m	0.0656	19022	268	-21.44	Sy2
06319+7536	18.1	OHP 1.93m	0.0915	26210	369	-19.74	Composite
06432+8551	19.0	BAO 2.6m	0.0898	25743	363	-18.80	HII
06432+8551b	16.5	SAO 6m	0.0891	25544	360	-21.28	HII
06545+6647	16.1	OHP 1.93m	0.0160	4765	67	-18.03	HII
06584+6716a	17.0	BAO 2.6m	0.0734	21214	299	-20.38	Composite
06584+6716b	17.9	BAO 2.6m	0.0710	20546	289	-19.41	Unknown
07007+8242	16.9	SAO 6m	0.0586	17066	240	-20.00	HII
07021+7349	14.0	OHP 1.93m	0.1031	29335	413	-24.08	LINER:
07158+7706	15.5	OHP 1.93m	0.0485	14198	200	-21.00	HII
07205+7842	16.3	OHP 1.93m	0.0866	24859	350	-21.42	Sy2
07225+7653	16.1	OHP 1.93m	0.0484	14160	199	-20.40	AGN
07479+7832	18.3	OHP 1.93m	0.1734	47577	670	-20.83	Em
08036+7211	15.4	BAO 2.6m	0.0387	11374	160	-20.63	Em
08054+6824	14.1	OHP 1.93m	0.0413	12123	171	-22.06	Composite
08095+6445	14.1	SAO 6m	0.0294	8690	122	-21.34	Norm.
08142+6821	16.0	OHP 1.93m	0.0388	11414	161	-20.03	HII
08247+7311	14.9	OHP 1.93m	0.0655	19013	268	-22.24	HII
08259+7427	17.3	OHP 1.93m	0.1232	34685	489	-21.14	HII
08303+6118	16.8	SDSS	0.0865	24831	350	-20.89	HII
08317+7602	17.0	OHP 1.93m	0.0931	26632	375	-20.87	HII
08339+6517	14.4	BAO 2.6m	0.0190	5634	79	-20.12	HII
08379+6753	16.0	BAO 2.6m	0.0363	10687	151	-19.89	HII
08410+6124	16.3	SDSS	0.0769	22189	313	-21.18	HII
08567+6325	15.7	SDSS	0.0386	11347	160	-20.31	HII/Sy2
09002+8106	16.6	SAO 6m	0.0494	14454	204	-19.94	HII
09020+6751a	16.7	BAO 2.6m	0.0505	14754	208	-19.89	LINER
09020+6751b	16.1	BAO 2.6m	0.0564	16435	231	-20.74	Em
09037+6937	16.8	OHP 1.93m	0.0125	3738	53	-16.81	HII
09056+6538	16.3	BAO 2.6m	0.0652	18910	266	-20.88	Composite
09056+6538	16.3	SDSS	0.0649	18829	265	-20.80	HII
09062+8134a	16.8	SAO 6m	0.0495	14483	204	-19.75	LINER:
09062+8134b	17.9	SAO 6m	0.0491	14369	202	-18.63	HII
09103+8326	17.1	SAO 6m	0.0497	14540	205	-19.46	HII

Table 1 – continued from previous page

IRAS source	m_V	Spectra source	z_{em}	v_r (km/s)	R (Mpc)	M	Activity type
09162+6539	14.6	SDSS	0.0379	11143	157	-21.35	HII
09162+6539	15.5	OHP 1.93m	0.0379	11160	157	-20.48	HII
09173+6231	15.6	SDSS	0.0473	13859	195	-20.90	HII
09176+6544	15.2	SDSS	0.0190	5640	79	-19.26	HII
09180+6532	16.0	OHP 1.93m	0.0382	11230	158	-20.00	HII
09229+7731	15.0	BAO 2.6m	0.0092	2741	39	-17.93	HII
09233+7825	14.7	OHP 1.93m	0.0747	21586	304	-22.71	Em
09244+7405	17.2	OHP 1.93m	0.1586	43847	618	-21.75	Sy2
09273+6232	16.3	SDSS	0.0420	12350	174	-19.89	AGN:
09305+6813	15.7	OHP 1.93m	0.0710	20548	289	-21.61	Sy2:
09343+6450	15.8	SDSS	0.0710	20542	289	-21.53	Sy2:
09363+6655	15.9	SDSS	0.0596	17355	244	-21.04	HII
09386+6240	15.6	SDSS	0.0397	11661	164	-20.48	Em
09406+6840	15.6	SDSS	0.0118	3506	49	-17.89	HII
09406+6840	16.3	OHP 1.93m	0.0119	3561	50	-17.20	HII
09418+8124	16.0	SAO 6m	0.0398	11703	165	-20.09	Abs
09427+7528	17.6	BAO 2.6m	0.1099	31168	439	-20.61	HII
09477+7050a	18.5	SAO 6m	0.1268	35645	502	-20.00	Norm.
09477+7050b	18.0	SAO 6m	0.1270	35698	503	-20.51	HII
09477+7050c	17.5	SAO 6m	0.1277	35881	505	-21.02	HII
09571+8435	16.5	SAO 6m	0.0924	26444	372	-21.36	HII
10045+7502b	16.0	BAO 2.6m	0.0481	14083	198	-20.49	LINER
10172+7548	16.2	OHP 1.93m	0.0592	17235	243	-20.73	HII
10210+7528	15.5	OHP 1.93m	0.0279	8245	116	-19.82	HII
10228+6227	17.2	SDSS	0.1163	32871	463	-21.17	HII
10252+7013	16.0	OHP 1.93m	0.1180	33319	469	-22.36	HII
10270+7302	12.5	OHP 1.93m	0.0224	6654	94	-22.36	HII
10272+6953	14.5	OHP 1.93m	0.0387	11391	160	-21.53	Composite
10276+7443	17.3	OHP 1.93m	0.0576	16769	236	-19.57	AGN
10298+6119	15.2	SDSS	0.0293	8666	122	-20.22	HII
10331+6338	15.9	SDSS	0.0381	11202	158	-20.04	HII
10361+7952a	15.9	BAO 2.6m	0.0388	11414	161	-20.16	HII
10361+7952b	15.5	BAO 2.6m	0.0394	11587	163	-20.56	HII/Comp:
10383+7637	16.2	OHP 1.93m	0.0315	9293	131	-19.38	AGN
10486+6558	16.7	SDSS	0.0338	9960	140	-18.99	HII
10527+7136	16.4	BAO 2.6m	0.1011	28790	405	-21.68	Composite
10529+7144	14.0	OHP 1.93m	0.0619	17996	253	-23.02	HII
10541+6614	17.3	SDSS	0.1306	36641	516	-21.22	Em
10589+6515	16.1	SDSS	0.0775	22362	315	-21.40	Sy2
11008+7915a	16.7	OHP 1.93m	0.0620	18013	254	-20.32	HII
11008+7915b	16.5	OHP 1.93m	0.0620	18013	254	-20.52	HII
11053+7037	14.0	OHP 1.93m	0.0412	12097	170	-22.16	HII
11059+7117	17.9	OHP 1.93m	0.1388	38761	546	-20.79	Composite
11067+7024a	15.5	BAO 2.6m	0.0389	11443	161	-20.54	HII/Comp:
11067+7024b	16.0	BAO 2.6m	0.0389	11443	161	-20.04	HII
11069+7438	16.2	OHP 1.93m	0.0395	11602	163	-19.87	HII
11085+7712a	15.6	OHP 1.93m	0.1003	28574	402	-22.42	Composite
11085+7712b	18.0	OHP 1.93m	0.0996	28404	400	-20.01	AGN
11161+6629	15.5	SDSS	0.0431	12663	178	-20.78	HII
11201+6305	16.9	SDSS	0.1905	51799	730	-22.41	Em
11201+6305	15.7	SDSS	0.0111	3311	47	-17.66	HII

Table 1 – continued from previous page

IRAS source	m_V	Spectra source	z_{em}	v_r (km/s)	R (Mpc)	M	Activity type
11371+8106	16.7	BAO 2.6m	0.0445	13053	184	-19.60	HII
11401+6642	15.4	SDSS	0.0554	16169	228	-21.36	HII
11436+7438	14.8	OHP 1.93m	0.0560	16333	230	-22.01	Composite
11462+6424	15.3	SDSS	0.0414	12169	171	-20.87	HII
11472+6647	15.3	SDSS	0.0402	11809	166	-20.78	Sy2
11497+6139	16.0	SDSS	0.0427	12530	176	-20.21	HII
11587+6124	17.4	SDSS	0.1638	45166	636	-21.66	HII
12008+6141	15.6	SDSS	0.0644	18689	263	-21.48	HII/LINER
12040+8158	17.7	BAO 2.6m	0.0903	25858	364	-20.14	HII
12069+6753	17.1	SDSS	0.0585	17026	240	-19.83	HII
12077+8131	16.5	BAO 2.6m	0.0397	11671	164	-19.56	HII
12119+6117	17.3	SDSS	0.1630	44948	633	-21.72	Em
12120+6838	15.5	SDSS	0.0602	17512	247	-21.48	HII
12120+6838	15.5	SDSS	0.0606	17643	248	-21.44	Sy1.9
12120+6838a	15.8	BAO 2.6m	0.0581	16924	238	-21.09	HII
12120+6838b	16.2	BAO 2.6m	0.0604	17574	248	-20.77	HII
12120+6838c	15.6	BAO 2.6m	0.0597	17376	245	-21.34	Composite
12138+7537a	16.9	BAO 2.6m	0.0497	14540	205	-19.67	HII
12138+7537b	15.5	BAO 2.6m	0.0468	13712	193	-20.93	Em
12138+7537c	16.5	BAO 2.6m	0.0525	15337	216	-20.17	LINER
12147+6306	15.4	SDSS	0.0501	14656	206	-21.14	HII
12147+6306	13.9	SAO 6m	0.0505	14768	208	-22.69	Norm.
12164+6437	15.0	SDSS	0.0308	9104	128	-20.57	HII
12207+6329	15.0	SDSS	0.0589	17154	242	-21.87	HII
12226+6630	17.4	SDSS	0.0865	24819	350	-20.37	Em
12226+6630	16.4	SDSS	0.0899	25762	363	-21.45	HII
12235+6253	16.6	SDSS	0.0672	19479	274	-20.60	AGN
12267+6540	16.4	SDSS	0.0504	14728	207	-20.15	HII
12312+6939	15.4	OHP 1.93m	0.0692	20035	282	-21.85	HII
12395+6238	14.2	SAO 6m	0.0342	10085	142	-21.56	Composite
12395+6238	15.7	SDSS	0.0338	9959	140	-20.08	HII
12470+6705	17.4	SDSS	0.1295	36345	512	-21.14	HII
12477+7936a	14.7	OHP 1.93m	0.0338	9972	140	-21.04	HII
12483+7332	14.9	OHP 1.93m	0.0314	9269	131	-20.68	HII
12502+7625	16.5	OHP 1.93m	0.0634	18424	259	-20.57	HII
13014+6146	15.3	SDSS	0.0269	7968	112	-19.93	HII
13014+6146	14.0	SAO 6m	0.0272	8049	113	-21.27	Norm.
13030+6102	15.4	SAO 6m	0.0698	20211	285	-21.87	HII
13045+7016a	16.2	OHP 1.93m	0.0646	18752	264	-20.91	Em
13045+7016b	16.4	OHP 1.93m	0.0645	18736	264	-20.71	HII
13121+6646	16.0	SDSS	0.0677	19627	276	-21.20	HII
13209+6353	17.5	SDSS	0.1997	54016	761	-21.91	Sy2
13234+6239	16.0	SDSS	0.0418	12272	173	-20.17	HII
13286+7258	14.0	OHP 1.93m	0.0305	8996	127	-21.51	AGN
13291+6524	17.3	SDSS	0.0365	10738	151	-18.62	LINER:
13300+6652	17.4	SDSS	0.1044	29694	418	-20.71	AGN
13300+7219	15.2	OHP 1.93m	0.0360	10594	149	-20.67	Composite
13367+6703	17.2	SDSS	0.0933	26680	376	-20.68	HII
13386+6557	16.2	SDSS	0.0480	14047	198	-20.26	HII
13410+7837	16.0	BAO 2.6m	0.0580	16905	238	-20.93	Composite
13503+6104	16.6	SDSS	0.0880	25230	355	-21.11	HII

Table 1 – continued from previous page

IRAS source	m_V	Spectra source	z_{em}	v_r (km/s)	R (Mpc)	M	Activity type
13513+6616	15.9	SDSS	0.0702	20331	286	-21.38	HII
13524+6213	16.5	SDSS	0.0729	21076	297	-20.86	HII
13524+6213	16.8	SDSS	0.0730	21111	297	-20.53	HII
14004+7445a	15.9	BAO 2.6m	0.0670	19422	274	-21.28	HII
14004+7445b	16.5	BAO 2.6m	0.0673	19523	275	-20.67	Composite
14013+6520	16.0	SDSS	0.0345	10173	143	-19.74	HII
14129+6111	17.8	SDSS	0.1514	42024	592	-21.11	HII
14132+6552	15.4	SDSS	0.0325	9585	135	-20.22	HII
14190+6432	17.2	SDSS	0.1525	42288	596	-21.70	LINER
14196+7734	16.6	BAO 2.6m	0.0469	13732	193	-19.87	AGN
14230+6158	16.4	SDSS	0.1112	31523	444	-21.80	Sy2
14244+6435	17.8	SDSS	0.1130	31992	451	-20.49	HII/Sy1.9
14263+6116	15.7	SDSS	0.0618	17967	253	-21.28	HII
14271+6437	17.7	SDSS	0.1411	39375	555	-20.98	HII
14360+6129	14.5	SAO 6m	0.0521	15223	214	-22.16	HII
14370+6254	16.6	SDSS	0.1154	32622	459	-21.75	HII
14386+6113	16.0	SDSS	0.0934	26721	376	-21.88	HII
14418+6131A	15.0	SDSS	0.0480	14044	198	-21.53	HII/LINER
14418+6131A	15.7	SDSS	0.0492	14410	203	-20.88	HII/LINER
14418+6131A	17.5	SDSS	0.0477	13958	197	-18.93	Em
14418+6131A	17.1	SDSS	0.0494	14458	204	-19.49	HII
14436+6258	14.9	SDSS	0.0375	11036	155	-21.07	HII
14445+7003	17.0	BAO 2.6m	0.0518	15138	213	-19.65	Em
14458+7926	16.5	BAO 2.6m	0.0316	9330	131	-19.09	Sy2:/Comp
14464+6119	16.9	SDSS	0.1364	38151	537	-21.76	Sy1.2
14501+6212	14.9	SAO 6m	0.0429	12594	177	-21.34	Abs
14501+6212	15.0	SDSS	0.0431	12666	178	-21.23	HII
14561+6312	14.7	SAO 6m	0.0432	12680	179	-21.56	Norm.
14561+6312	15.2	SDSS	0.0426	12510	176	-21.08	Sy2
14570+6339	16.2	SAO 6m	0.0475	13912	196	-20.26	LINER
14574+7641a	16.5	BAO 2.6m	0.0446	13082	184	-19.83	HII
15356+6119a	16.4	SAO 6m	0.0886	25407	358	-21.37	HII
15356+6119b	14.4	SAO 6m	0.0882	25297	356	-23.36	HII
15374+6822	15.7	BAO 2.6m	0.0578	16851	237	-21.17	HII
15427+6141	17.6	SAO 6m	0.0573	16698	235	-19.26	Norm.
15449+6459	15.3	SAO 6m	0.0373	10981	155	-20.65	Norm.
16030+6312a	16.8	SAO 6m	0.0548	15990	225	-19.96	Norm.
16030+6312b	15.9	SAO 6m	0.0569	16585	234	-20.94	HII
16044+6727	16.1	BAO 2.6m	0.0233	6906	97	-18.85	HII
16049+8802	16.8	BAO 2.6m	0.0541	15803	223	-19.95	Sy2
16101+6345	16.5	SAO 6m	0.0563	16415	231	-20.32	HII
16118+6231	13.3	SAO 6m	0.0321	9476	133	-22.33	Composite
16119+8551	17.1	BAO 2.6m	0.0847	24335	343	-20.54	HII
16358+6709a	15.0	BAO 2.6m	0.0534	15593	220	-21.69	Em
16358+6709b	15.0	BAO 2.6m	0.0537	15687	221	-21.70	HII
16365+6403a	15.7	SAO 6m	0.0628	18250	257	-21.35	HII
16365+6403b	17.5	SAO 6m	0.0628	18250	257	-19.55	HII
16365+6403c	12.6	SAO 6m	0.0632	18362	259	-24.46	HII
16452+6418a	16.3	SAO 6m	0.0697	20183	284	-20.97	Sy2
16452+6418b	16.6	SAO 6m	0.0684	19820	279	-20.63	HII
16452+6418c	14.2	SAO 6m	0.0685	19848	280	-23.03	HII

Table 1 – continued from previous page

IRAS source	m_V	Spectra source	z_{em}	v_r (km/s)	R (Mpc)	M	Activity type
16452+6418d	17.1	SAO 6m	0.0697	20183	284	-20.17	HII
16533+6216	16.1	SDSS	0.1059	30089	424	-22.03	HII
16588+6357	15.6	SDSS	0.0604	17568	247	-21.40	Em
17008+6444	15.0	SDSS	0.0273	8076	114	-20.26	HII
17008+6444	12.6	SAO 6m	0.0278	8224	116	-22.72	HII
17017+6416	15.2	SDSS	0.0843	24238	341	-22.43	HII
17017+6416	14.1	SAO 6m	0.0848	24365	343	-23.58	HII
17037+6207	17.2	SDSS	0.1558	43138	608	-21.73	Em
17037+6207	15.8	SDSS	0.0823	23669	333	-21.86	HII
17046+6255	16.4	SDSS	0.0883	25318	357	-21.39	HII
17046+6255	20.6	SDSS	0.0874	25086	353	-17.17	HII
17062+7544	16.1	BAO 2.6m	0.0654	18974	267	-21.02	Em
17089+6558	17.3	SDSS	0.0278	8238	116	-18.04	HII/LINER
17089+6558a	17.6	BAO 2.6m	0.0279	8256	116	-17.73	HII
17089+6558b	15.6	BAO 2.6m	0.0282	8335	117	-19.75	HII
17102+6442	16.1	SDSS	0.0789	22735	320	-21.42	HII
17102+6442	14.4	SAO 6m	0.0789	22739	320	-23.13	HII
17173+6119	15.7	SDSS	0.0717	20732	292	-21.67	HII
17173+6119	14.7	SAO 6m	0.0735	21242	299	-22.68	Composite
17190+6219	16.7	SDSS	0.0803	23117	326	-20.84	AGN
17190+6219	17.0	SAO 6m	0.0808	23264	328	-20.58	Norm.
17207+6307	15.4	SDSS	0.0338	9972	140	-20.30	HII
17207+6307	15.3	SAO 6m	0.0336	9911	140	-20.42	HII
17330+7619	17.2	BAO 2.6m	0.0769	22185	312	-20.26	HII
17349+6139a	16.2	SAO 6m	0.0858	24639	347	-21.50	HII
17349+6139b	18.8	SAO 6m	0.0862	24749	349	-18.91	Norm.
17442+6130	14.0	SAO 6m	0.0365	10750	151	-21.90	Norm.
17469+6416	14.6	SAO 6m	0.0355	10461	147	-21.24	HII
17552+6209	16.4	SAO 6m	0.0836	24035	339	-21.25	Sy2
17591+8628	15.2	BAO 2.6m	0.0233	6917	97	-19.72	HII
18116+6328	13.9	SAO 6m	0.0481	14083	198	-22.59	Norm.
18169+6433c	12.4	SAO 6m	0.0208	6175	87	-22.30	HII
18169+6433d	15.1	SAO 6m	0.0209	6204	87	-19.61	HII
18192+8650	16.3	BAO 2.6m	0.0655	19002	268	-20.88	HII
18247+6102	15.7	SAO 6m	0.0732	21158	298	-21.67	LINER
18252+6315	15.9	SAO 6m	0.0838	24090	339	-21.75	HII
18380+8640b	16.1	BAO 2.6m	0.0778	22435	316	-21.43	HII
18380+8640c	16.0	BAO 2.6m	0.0779	22451	316	-21.46	HII
20537+8737	14.8	BAO 2.6m	0.0195	5784	81	-19.77	Em

The objects have redshifts in the range $0.0092 < z < 0.1997$ and absolute stellar magnitudes in the range $-16.81 < M < -24.46$. The distribution of redshifts is given in Fig. 1 and the distribution of absolute magnitudes is given in Fig. 2.

3. Summary and conclusion

Spectral observations of BIG objects at the BAO 2.6-m, SAO 6-m, OHP 1.93-m telescopes and taken from SDSS database have yielded a fairly rich set of data for studying IR galaxies. These data can be used to study the BIG sample, and also to compare these objects with IR galaxies from other samples. A total of 257 BIG objects were observed; of these 149 were identified as galaxies with star formation regions, 42 as AGN, 28 as galaxies with a composite spectrum (referred below

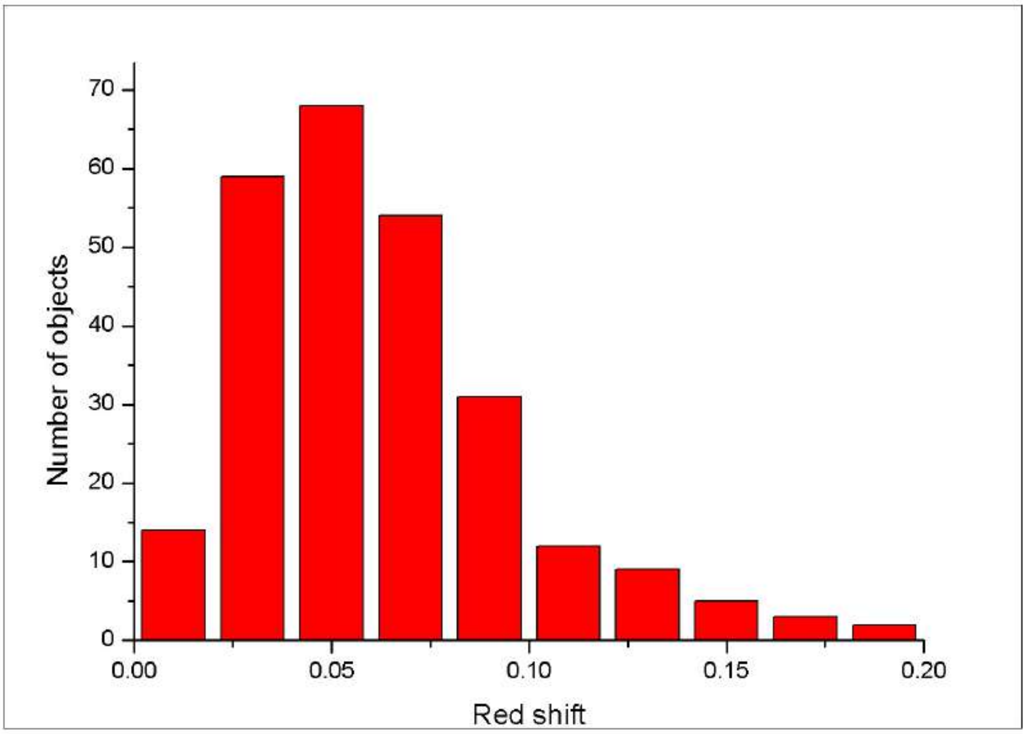

Figure 1. Distribution of redshifts

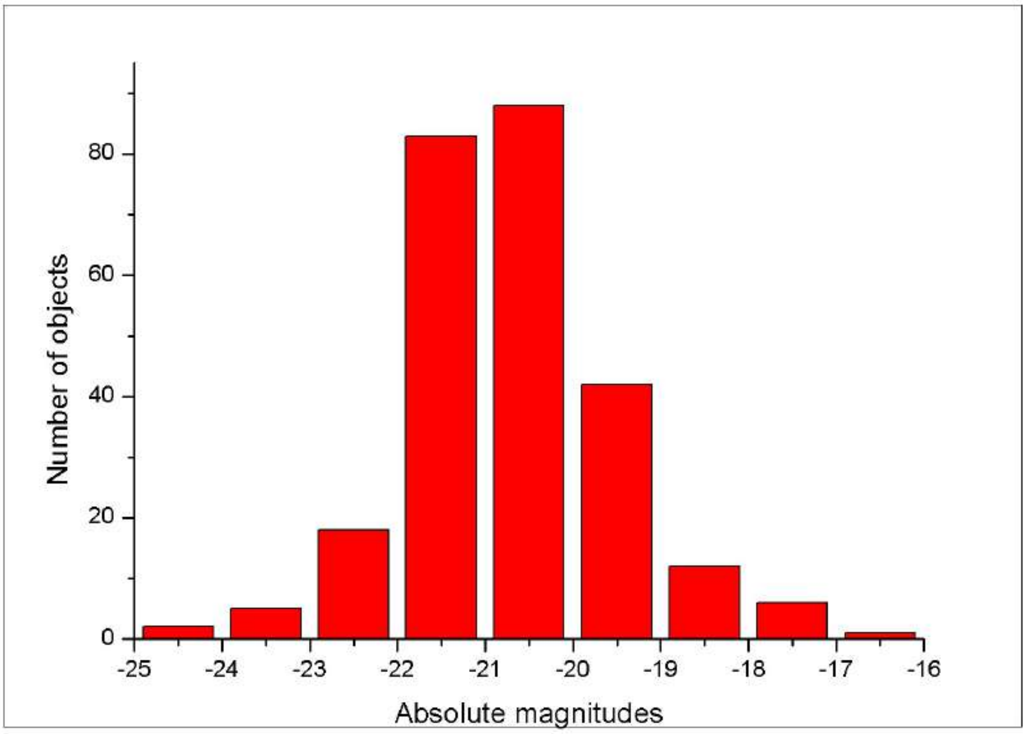

Figure 2. Distribution of absolute magnitudes

to Composite or Comp), 21 as "Em" galaxies (this type refers to a spectrum with signs of emission without the possibility of a more precise determination of the activity class of the galaxy), 13 as galaxies represented as Norm (galaxies for which the rate of star formation does not exceed the normal), 3 as absorption galaxy and one object without the possibility of classification (unknown). In Table 2 the distribution of all objects by activity types is given.In Fig. 3 absolute magnitude (M) vs redshift (z) is given.

Table 2: The distribution of 257 BIG objects by activity types

Activity type	Number of objects	%	Activity type	Number of objects	%
HII	149	58.0	AGN	13	5.1
Composite	22	8.6	Em	21	8.2
HII / LINER	4	1.5	Norm	13	5.1
HII / Sy	2	0.8	Abs	3	1.1
LINER	12	4.6	Unknown	1	0.4
Sy	17	6.6	**All**	**257**	**100.0**

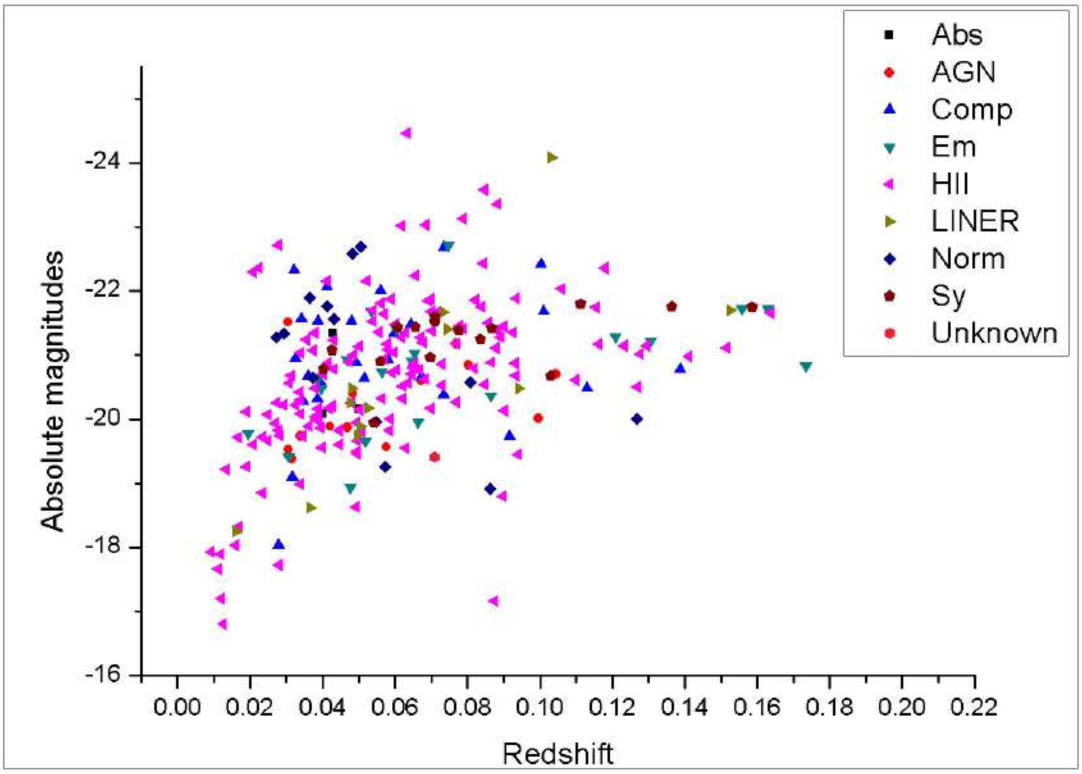

Figure 3. The distribution of absolute magnitudes vs redshifts

Besides isolated galaxies, the observed objects include some binary and multiple systems. This makes it possible to establish their physical coupling, to determine the true IR source more precisely (as an individual galaxy or the system as a whole), and to study the interrelation between star formation activity, the interactions of galaxies, and the activity of their nuclei.

References

M. Moshir, G. Kopan, T. Conrow, and et al. *Infrared Astronomical Satellite Catalogs, The Faint Source Catalog, Version 2.0*, 1990.

H.V. Abrahamyan, A.M. Mickaelian, and A.V. Knyazyan. *Astron. Comput. 10, 99*, 2015.

D.B. Sanders and I.F. Mirabel. *Luminous Infrared Galaxies, Ann. Rev. Astron. Astrophys. 34, 749*, 1996.

R.M. Cutri, M.F. Skrutskie, S. van Dyk, and et al. *2MASS All-Sky Catalog, Univ. Mass. and IPAC/CalTech*, 2003.

M.F. Skrutskie, R.M. Cutri, R. Stiening, M.D. Weinberg, S. Schneider, J.M. Carpenter, C. Beichman, R. Capps, and et al. *Astron. J. 131, 1163*, 2006.

R.M. Cutri, E.L. Wright, T. Conrow, and et al. *WISE All-Sky DR, IPAC/Caltech*, 2013.

D. Ishihara, T. Onaka, H. Kataza, A. Salama, C. Alfageme, A. Cassatella, N. Cox, P.García-Lario, and et al. *Astron. Astrophys. 514, 1*, 2010.

I. Yamamura, S. Makiuti, N. Ikeda, Y. Fukuda, S. Oyabu, T. Koga, and G.J. White. *AKARI/FIS, ISAS/JAXA*, 2010.

D.B. Sanders, J.M. Mazzarella, D.-C. Kim, J.A. Surace, and B. T. Soifer. *Astron. J. 126, 1607*, 2003.

E. Bertin, M. Dennefeld, and M. Moshir. *Astron. Astrophys. 323, 685*, 1997.

M.A. Strauss and J.P. Huchra. *Astron. J. 95, 1602*, 1988.

G. Wang, S.K. Leggett, R.G. Clowes, H.T. MacGillivray, and A. Savage. *MNRAS 248, 112*, 1991.

K.B. Fisher, J.P. Huchra, M.A. Strauss, M. Davis, A. Yahil, and D. Schlegel. *Astrophys. J. Suppl. Ser. 100, 69*, 1995.

Q.R. Yuan, Z.H. Zhu, Z.L. Yang, and X.T. He. *Astron. Astrophys. Suppl. Ser. 115, 267*, 1996.

A.M. Mickaelian. *Astrophysics 38, 625*, 1995.

D.W. Weedman, F.R. Feldman, V.A. Balzano, and et al. *Astrophys. J. 248, 105*, 1981.

V.A. Ambartsumian. *XI Solvay Conference, Editions Stoops, Brussels*, 1958.

A.M. Mickaelian and L.A. Sargsyan. *Astrofizika 47, 109*, 2004.

A.M. Mickaelian and K.S. Gigoyan. *Astron. Astrophys. 455, 765. Catalog No. III/237a in Vizier, CDS, Strasbourg*, 2006.

B.E. Markarian, V.A. Lipovetsky, J.A. Stepanian, L.K. Erastova, and A.I. Shapovalova. *Comm. SAO 62, 5*, 1989.

A.M. Mickaelian, R. Nesci, C. Rossi, D. Weedman, G. Cirimele, L.A. Sargsyan, L.K. Erastova, K.S. Gigoyan, and et al. *Astron. Astrophys. 464, 1177*, 2007.

E. Massaro, A.M. Mickaelian, R. Nesci, and D. Weedman. *The Digitized First Byurakan Survey (Roma, Italy)*, 2008.

A.M. Mickaelian, L.R. Oganesyan, and L.A. Sargsyan. *Astrofizika 46, 221*, 2003.

L.A. Sargsyan and A.M. Mickaelian. *Astrofizika 49, 19*, 2006.

A.M. Mickaelian, S.A. Akopyan, S.K. Balayan, and A.N. Burenkov. *Pis'ma v Astron. zh. 24, 736*, 1998.

S.K. Balayan, S.A. Akopyan, A.M. Mickaelian, and A.N. Burenkov. *Pis'ma v Astron. zh. 27, 330*, 2001.

A.M. Mickaelian. *Astrofizika 47, 425*, 2004.

B. Abolfathi, D.S. Aguado, G. Aguilar, and et al. *The Astrophysical Journal Supplement Series, 235, issue 2, article id. 42, p. 19*, 2018.

A.M. Mickaelian, G.S. Harutyunyan, and A. Sarkissian. *Astronomy Letters, Volume 44, Issue 6, pp.351-361*, 2018.

Joint IRAS Science Working Group. *Infrared Astronomical Satellite Catalogs, The Point Source Catalog, Version 2.0, NASA RP-1190*, 1988.

Some New Results in the Group-theoretical Description of the Radiation Transfer

A. Nikoghossian*

NAS RA V.Ambartsumian Byurakan Astrophysical Observatory, Byurakan 0213, Aragatsotn Province, Armenia

Abstract

The paper presents some new results of investigation developing the approach aimed at applying the group theory methods to radiation transfer problems. It consists of two separate parts. In the first part we derive new properties of supersymmetry of fundamental supermatrices - representations of composition and translation groups. It is shown that these supermatrices, which determine the layers adding to the two opposite boundaries of inhomogeneous medium, are connected with each other by the procedure of parity transposition. It is also demonstrated that, by analogy with the common second order matrices, the considered supermatrices can be factorized yielding the product of triangular supermatrices. The second part generalizes and applies the concept of composition groups to the case of media with spherical symmetry.

1. Inroduction

The bases of application of the group theory methods in the problems of radiative transfer are given in a series of author's papers (Nikoghossian, 2014, 2019). The importance of such application is determined by at least two main factors. First of all, it must be noted its value at revealing symmetry and supersymmetry properties in problems of the transfer theory and in establishing the close connection between various problems of astrophysical importance, on one hand, and different classical methods of solution, on the another hand. The symmetry properties, in turn, has enabled to propose the Lagrange-Hamiltonian approach (Nikoghossian, 1999, 2013) and to derive conservation laws in many classical problems. Thanks to this approach, many of the basic physical properties of the problem under study can be established before the problem is solved. Finally, the found representations of composition and translation groups offer new simpler schemes of both analytical and numerical solution of realistic and then rather complex radiation transfer problems,

In this paper, we will first present some new relations between the basic supermatrices introduced by the author in connection with the symmetry properties of the problem of radiation transfer in the medium of finite optical thickness. Further on, we generalize some of the results obtained for the plane-parallel media to the case of media with spherical symmetry.

2. The symmetry properties of basic super-matrices.

In the mentioned fundamental works (Nikoghossian, 2011, 2014) we have obtained the representations of composition groups in the form of second order supermatrices, which establish the adding law for global optical properties (reflection and transmittance coefficients) of scattering and absorbing media when being they combined. It was also shown that these representations also describe the transition from one optical depth to the another, which, in determining the field of radiation inside the medium, can be considered as a law of translation between different depths. These laws obtained by applying the group theory, in fact, can be considered as a further development Ambartsumian's idea, which is the basis of his method of layers addition (Ambartsumian, 1944, Ambartsumyan, 1960). They

*nikoghoss@yahoo.com

DOI: 10.52526/25792776-2019.66.1-41

cover a wide range of various problems of radiation transfer theory, involving important problems of theoretical astrophysics.

In this section, we show how the forms of representations of composition groups are related with each other in the most general case of inhomogeneous medium. We remind that, when the inhomogeneous medium is illuminated from the side of one of its boundaries, the addition of global optical characteristics is carried out with the help of supermatrices as follows

$$\tilde{\mathbf{A}} = \begin{pmatrix} \mathbf{P} & -\bar{\mathbf{S}} \\ \mathbf{S} & \mathbf{M} \end{pmatrix}, \qquad \tilde{\mathbf{B}} = \begin{pmatrix} \mathbf{M} & -\mathbf{S} \\ \bar{\mathbf{S}} & \mathbf{P}. \end{pmatrix}. \tag{1}$$

where we have used the notations introduced in Nikoghossian (2014): $\mathbf{P} = \mathbf{Q^{-1}}, \mathbf{S} = \mathbf{RP}, \bar{\mathbf{S}} = \mathbf{P}\bar{\mathbf{R}}, \mathbf{M} = \mathbf{Q}^* - \mathbf{S}\bar{\mathbf{R}}$. Here $\mathbf{R}$ and $\bar{\mathbf{R}}$ are the reflectance of the medium of two mutually opposite sides and $\mathbf{Q}$, $\mathbf{Q}^*$ are corresponding transmission coefficients. As usual, the transposed matrices are supplied by asterisks. The properties of these supermatrices were studied in the mentioned papers and were particularly shown their invertibility given by

$$\tilde{\mathbf{A}}^{-1} = \begin{pmatrix} \mathbf{M}^* & \bar{\mathbf{S}}^* \\ -\mathbf{S}^* & \mathbf{P}^* \end{pmatrix}, \qquad \tilde{\mathbf{B}}^{-1} = \begin{pmatrix} \mathbf{P}^* & \mathbf{S}^* \\ -\bar{\mathbf{S}}^* & \mathbf{M}^* \end{pmatrix}. \tag{2}$$

Similarly, with the same designations and the same direction of reference, if the medium is illuminated from the opposite side, the supermatrixes of the compositions group are

$$\tilde{\mathbf{C}} = \begin{pmatrix} \mathbf{P}^* & -\mathbf{S}^* \\ \bar{\mathbf{S}}^* & \mathbf{M}^* \end{pmatrix}, \qquad \tilde{\mathbf{D}} = \begin{pmatrix} \mathbf{M}^* & -\bar{\mathbf{S}}^* \\ \mathbf{S}^* & \mathbf{P}^* \end{pmatrix}. \tag{3}$$

which are also non-singular

$$\tilde{\mathbf{C}}^{-1} = \begin{pmatrix} \mathbf{M} & \mathbf{S} \\ -\bar{\mathbf{S}} & \mathbf{P} \end{pmatrix}, \qquad \tilde{\mathbf{D}}^{-1} = \begin{pmatrix} \mathbf{P} & \bar{\mathbf{S}} \\ -\mathbf{S} & \mathbf{M} \end{pmatrix}, \tag{4}$$

These supermatrices are fundamental in the developed theory since they establish the laws of transformation of global optical characteristics in composing scattering and absorbing media. All of them have a number of common properties, of which, except invertibility, we note the equality to unity of their superdeterminants (Nikoghossian, 2014, 2019). Being the supermatrices of the second order, they, by analogy with usual matrices, can be represented in the form of the product of two triangular supermatrices. So, for example, in the case of the supermatrix $\mathbf{A}$, one can write an easily verifiable equality

$$\tilde{\mathbf{A}} = \begin{pmatrix} \mathbf{I} & \mathbf{0} \\ \mathbf{R} & \mathbf{I} \end{pmatrix} \begin{pmatrix} \mathbf{P} & -\bar{\mathbf{S}} \\ \mathbf{0} & \mathbf{Q}^*. \end{pmatrix}. \tag{5}$$

where $\mathbf{I}$ is the unit matrix. The supermatrices we have introduced, along with the inverse ones describe the same composition of the medium illuminated from two mutually opposite sides. This obviously means that there must be a relationship between these group representations with use of the concepts of supertransposition and transposition of parity

$$\begin{aligned} \left(\tilde{\mathbf{A}}^{st}\right)^{st} &= \tilde{\mathbf{D}}^{-1}, \qquad & \left(\tilde{\mathbf{B}}^{st}\right)^{st} &= \tilde{\mathbf{C}}^{-1}, \\ \left(\tilde{\mathbf{D}}^{st}\right)^{st} &= \tilde{\mathbf{A}}^{-1}, \qquad & \left(\tilde{\mathbf{C}}^{st}\right)^{st} &= \tilde{\mathbf{B}}^{-1}, \end{aligned} \tag{6}$$

where the upper index st means supertransposition. There are more simple relations which use the concept of the parity transposition marked by the upper index π

$$\tilde{\mathbf{A}}^{\pi} = \tilde{\mathbf{C}}^{-\mathbf{1}}, \qquad \tilde{\mathbf{B}}^{\pi} = \tilde{\mathbf{D}}^{-\mathbf{1}}, \qquad \tilde{\mathbf{C}}^{\pi} = \tilde{\mathbf{A}}^{-\mathbf{1}}, \qquad \tilde{\mathbf{D}}^{\pi} = \tilde{\mathbf{B}}^{-\mathbf{1}}. \tag{7}$$

Finally, the results obtained for representation of composition groups for two mutually opposite directions in the general case of inhomogeneous media can be presented as follows

$$\begin{pmatrix} \mathbf{A} & \mathbf{0} \\ \mathbf{0} & \mathbf{B} \end{pmatrix} \begin{pmatrix} \mathbf{C}^{\pi} & \mathbf{0} \\ \mathbf{0} & \mathbf{D}^{\pi} \end{pmatrix} = \begin{pmatrix} \mathbf{C} & \mathbf{0} \\ \mathbf{0} & \mathbf{D} \end{pmatrix} \begin{pmatrix} \mathbf{A}^{\pi} & \mathbf{0} \\ \mathbf{0} & \mathbf{B}^{\pi} \end{pmatrix} = \begin{pmatrix} \mathbf{I} & \mathbf{0} \\ \mathbf{0} & \mathbf{I} \end{pmatrix} \tag{8}$$

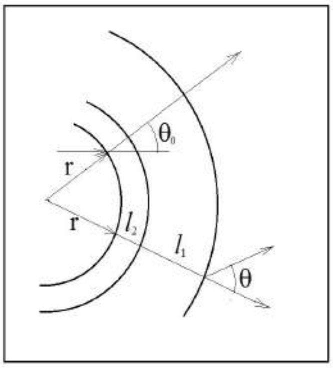

Figure 1. The schematic picture of radiating one-dimensional turbulent atmosphere

3. Representations of composition groups for media with spherical symmetry

We now show how the approach elaborated for plane-parallel media in Nikoghossian (2014, 2019) can easily be generalized to the case of media with spherical symmetry. Such generalization is of great aetrophysical interest, especially when we deal with extended atmospheres of stars. From mathematical point of view, the study of media with spherical symmetry generally is more complex because of appearance of additional parameters due to the curvature and its effects. Therefore, any progress that contributes to the solution of the problems of multiple light scattering in the media with spherical geometry is of great importance.

Let us start with considering the problem of radiation transfer through two spherical, generally inhomogeneous layers, which are illuminated from the inner spherical region with radius r. Each layer will be specified by its internal radius and optical thickness τ_0 with corresponding geometric thicknesses ℓ calculated along the normal. The incident radiation is supposed to be isotropic. The angles of incidence of radiation on the medium and its exit are correspondingly designated through ϑ_0 and ϑ (Fig. 1). We also suppose that the inner spherical core does not take part in the multiple scattering process, i.e., the photons reflected from the shells do not turn back to it from the core. Evidently, such assumption may be regarded as realistic for sufficiently distant shells. On the other hand, this assumption is crucial from the point of view of application of the developed theory to this simplified model case.

We are interested in global optical characteristics of the composite atmosphere, provided that these characteristics for constituent layers are known. In this formulation of the problem, it is possible to apply the procedure of combining the scattering spherical layers, which is in many respects similar to the composition of planar media considered in Nikoghossian (2014, 2019). Here also, as a binary operation we can choose the result of two successive transformations that present addition of new layers. Then it is easy to check that the group properties of the composition procedure are satisfied. The composition groups for spherical layers are characterized by their non-commutativity, which in contrast to plain-parallel media, occurs even if the added media are homogeneous. In general, the treated group of compositions is two-parametric, where as parameters can be chosen internal radius and optical or geometric thickness of the layer.

Following the approach suggested in Nikoghossian (2014), the reflection and transmission coefficients of the layer in the discrete space can be represented in the form of matrices, denoted as $\mathbf{R}\left(\mathbf{r}, \tau_{\mathbf{0}}\right)$ and $\mathbf{Q}\left(\mathbf{r}, \tau_{\mathbf{0}}\right)$. Now the elements of fundamental matrices $\mathbf{P}$, $\mathbf{S}$, $\bar{\mathbf{S}}$, $\mathbf{M}$ in the representation of the composition groups associated with the probability of reflection and transmission depend also on the thickness of the layer and its curvature. The process of radiation diffusion depending on the frequency will not be considered here.

Fig,1 schematically shows the composition of two spherical layers, with the layers numbering chosen in such a way that it together with the direction of the incident radiation coincide with those in the model used in Nikoghossian (2014). This will make it possible to preserve both the reasoning and resulting relations obtained for plane-parallel media. The reasoning used in the mentioned paper to obtain the representations of a group of compositions also remain valid. Referring the reader to this work for the course of argumentation, we point out that

$$\mathbf{Q_{1\cup 2}} = \mathbf{Q_1 T Q_2} \tag{9}$$

is also true for spherical media in our case. The reasoning also remains in force, in deriving the first important relation, which connects the values of $\mathbf{P}, \mathbf{S}, \bar{\mathbf{S}}$ of the two media

$$\mathbf{P_{1\cup 2}} = \mathbf{P_2 P_1} - \bar{\mathbf{S}}_\mathbf{2} \mathbf{S_1} \tag{10}$$

In the expanded form the equation (10) for our case will be rewritten as

$$\mathbf{P}(\mathbf{r}, \ell_\mathbf{1} + \ell_\mathbf{2}) = \mathbf{P}\left(\mathbf{r}, \ell_\mathbf{2}\right) \mathbf{P}\left(\mathbf{r} + \ell_\mathbf{2}, \ell_\mathbf{1}\right) - \bar{\mathbf{S}}\left(\mathbf{r}, \ell_\mathbf{2}\right) \mathbf{S}\left(\mathbf{r} + \ell_\mathbf{2}, \ell_\mathbf{1}\right) \tag{11}$$

Analogously, we have

$$\mathbf{S}(\mathbf{r}, \ell_\mathbf{1} + \ell_\mathbf{2}) = \mathbf{S}\left(\mathbf{r}, \ell_\mathbf{2}\right) \mathbf{P}\left(\mathbf{r} + \ell_\mathbf{2}, \ell_\mathbf{1}\right) + \mathbf{M}\left(\mathbf{r}, \ell_\mathbf{2}\right) \mathbf{S}\left(\mathbf{r} + \ell_\mathbf{2}, \ell_\mathbf{1}\right) \tag{12}$$

Thus, in this formulation of the problem, the transformation of the basic matrices is carried out by means of the supermatrix which is the natural generalization of that of the same name in the case of the planar geometry

$$\tilde{\mathbf{Y}}\left(\mathbf{r}, \ell_\mathbf{1} + \ell_\mathbf{2}\right) = \tilde{\mathbf{A}}\left(\mathbf{r}, \ell_\mathbf{2}\right) \tilde{\mathbf{Y}}\left(\mathbf{r} + \ell_\mathbf{2}, \mathbf{l_1}\right), \tag{13}$$

where, as before in [1]

$$\tilde{\mathbf{Y}} = \begin{pmatrix} \mathbf{P} \\ \mathbf{S} \end{pmatrix} \qquad \tilde{\mathbf{A}} = \begin{pmatrix} \mathbf{P} & -\bar{\mathbf{S}} \\ \mathbf{S} & \mathbf{M} \end{pmatrix} \tag{14}$$

For simplicity, we will conduct further reasoning for homogeneous layers, i.e. we assume that the physical parameters determining the elementary act of scattering does not vary throughout of the medium. Then, for the infinitesimal operator of the two-parametric group under consideration, we have

$$\tilde{\Xi}\left(r, 0\right) = \lim_{\Delta\ell \to 0} \frac{\tilde{\mathbf{A}}\left(r, \Delta\ell\right) - \mathbf{E}}{\Delta\ell} = \begin{pmatrix} \mathbf{m} & -\mathbf{n} \\ \mathbf{n} & -\mathbf{m} \end{pmatrix}, \tag{15}$$

where we have introduced notations

$$\mathbf{m} = \frac{\mathbf{1}}{\xi}\left[\mathbf{I} - \frac{\lambda}{\mathbf{2}}\mathbf{x}\left(\gamma\right)\right], \qquad \mathbf{n} = \frac{\lambda}{\mathbf{2}\xi}\mathbf{x}\left(\gamma\right), \qquad \tilde{\mathbf{E}} = \begin{pmatrix} \mathbf{I} & 0 \\ 0 & \mathbf{I}, \end{pmatrix} \tag{16}$$

and $\xi = \cos\theta_0$, $\eta = \cos\theta$, $\mathbf{x}\left(\gamma\right)$ is the diffusion indicatrix dependent on the scattering angle γ, and λ is the coefficient of re-radiation of quantum in the elemetary act of scattering.

With use of (16) the relations (12), (13) can be written in the differential form. To this end we replace ℓ_2 by infinitesimal thickness $\Delta\ell$ and ℓ_1 by ℓ. Then passing to the limit when $\Delta\ell \to 0$, we find

$$\frac{\partial\mathbf{P}}{\partial\ell} - \frac{\partial\mathbf{P}}{\partial r} = \mathbf{m}\mathbf{P}(r, \ell) - \mathbf{n}\mathbf{S}(r, \ell) \tag{17}$$

$$\frac{\partial\mathbf{S}}{\partial\ell} - \frac{\partial\mathbf{S}}{\partial r} = \mathbf{n}\mathbf{P}(r, \ell) - \mathbf{m}\mathbf{S}(r, \ell) \tag{18}$$

with the initial conditions $\mathbf{P}\left(\mathbf{r}, \mathbf{0}\right) = \mathbf{I}/\xi$, $\mathbf{S}(\mathbf{r}, \mathbf{0}) = \mathbf{0}$. Thus, we are led to a set of two partial differential linear equations which with the proper parametrisation may be reduced to a set of ordinary differential equations for the functions $\bar{\mathbf{P}}(t) \equiv \mathbf{P}(r, t+\ell)$, $\bar{\mathbf{S}}(t) \equiv \mathbf{S}(r, t+\ell)$. This kind of two-parametric equations we have already obtained in considering the model non-stationary transfer problem as well as the problem of multiple scattering in the turbulent media (see Nikoghossian (2019)). There are standard classical methods used equation of characteristics (see e.g., Courant & Hilbert (1962), Rojdenstvenski & Yanenko (1968)upon which we do not dwell here. In the case of the model problem treated in the present paper, the curvature of the medium mathematically affects only the form of the resulted equation, meanwhile the solution of the problem we are led is equivalent to that for the plain-parallel atmosphere of geometrical thickness ℓ (Nikoghossian, 2012). The approach we adopt in the paper can be applied to the more general problem of astrophysical interest when the target value is the observed intensity, i.e., that along the line of sight. This leads to appearance of the new parameter denoting the angle between direction of the photons exit and the line of sight (see e.g., Mihalas (1978), Sobolev (1963). This three-parametric problem will be serve as a subject of one of our future works.

References

Ambartsumian V. A., 1944, Izv. Akad. Nauk ArmSSR, N 1, 2

Ambartsumyan V. A., 1960, Scientific Works, V. I, Yerevan,Izd. Acad. Nauk ArmSSR

Courant R., Hilbert D., 1962, Methods of Mathematical Physics, V. II

Mihalas D., 1978, Stellar atmospheres, San-Francisco, Freeman

Nikoghossian A. G., 1999, JQSRT, 61, 345

Nikoghossian A. G., 2011, Astrophysics, 54, 553

Nikoghossian A. G., 2012, Astrophysics, 55, 261

Nikoghossian A. G., 2013, Light Scat. Reviews, 55, 377

Nikoghossian A. G., 2014, Astrophysics, 57, 272

Nikoghossian A. G., 2019, Astrophysics, 62, 92

Nikoghossian A. G., 2014a, Astrophysics, 57, 375

Rojdenstvenski B. L., Yanenko N. N., 1968, Systems of Quasi-linear Equations and Their Application to Gas Dynamics, M., Nauka,

Sobolev V. V., 1963, A Treatise on Radiative Transfer, Princeton: van Nostrand.,

Some observational manifestations of the periodic inhomogeneity of absorbing and scattering atmospheres

A. Nikoghossian*

NAS RA V.Ambartsumian Byurakan Astrophysical Observatory, Byurakan 0213, Aragatsotn Province, Armenia

Abstract

We consider frequency and directional features of the reflectance and transmittance of an inhomogeneous scattering and absorbing atmosphere with the scattering albedo periodically varying with depth. The dependence of global optical properties of such media on optical thickness is found. Two different kind of problems are considered dependent on that by monochromatic or continuum, mono-directional or diffuse radiation illuminate the medium. The numerical results show how the observed intensities and line-profiles respond to the medium inhomogeneity with an uniform increase in optical thickness. Astrophysical aspects of these features are discussed.

1. Introduction

It is well established that at some stages of their evolution the stars exhibit the matter outflow in the form of a more or less dense wind forming extended envelops. Luminous Blue Variables (LBVs), Ae, Be He and T Tau stars are good examples of this kind intensively studied astronomical objects. Especially exotic are luminosity variations of LBV stars which may change their spectral class under almost constant value of bolometric luminosity. As it was shown by (Israelian & Nikoghossian, 1996, Nikoghossian & Israelian, 1996), this effect can be explained by appearing of some centers coherently scattering in the continuum (e.g., free electrons) leading to an increase in optical thickness of winds.

The temporal irregularity of the luminosity variation is usually interpreted by changes in the temps of outflow and other non-stationary phenomena as the matter accretion from companion stars. It must be, however, noted that in the majority of cases the ejected matter is assumed homogeneous which hardly is realisable in the reality. This insists on considering the general case of inhomogeneous envelopes with irregular variations of global thermodynamic parameters which determine the radiation scattering process in the medium.

The paper may be considered as an attempt to fill this gap by revealing how and at what extent observational characteristics mimic the changes in physical papameters inside the radiating medium.

2. Formulation of the problem and basic equations.

For simplicity's sake, we consider the ID frequency-dependent and 3D mono-chromatic problems of the line-radiation transfer in scattering and absorbing media of different optical thicknesses. The inhomogeneity of the medium is supposed to be due to that of the scattering coefficient (particle albedo or the probability of re-radiation in the elementary act of scattering denoting by λ) changes within the medium according to a certain periodical law of the form $\lambda(\tau) = 0.5\,(1 + \sin 3\tau)$. This choice of the function $\lambda(\tau)$ is due to easier tracking the observational effect of changes in the physical state in the medium. We limit ourselves by treating *periodically* varying inhomogeneity, however, its results evidently allow to make an idea on effects expected in the case of any *irregular* variation of this parameter.

*nikoghoss@yahoo.com

DOI: 10.52526/25792776-2019.66.1-46

Thus, we are interested in the behavior of the reflectance of the medium from the side of $\tau = \tau_0$ and its transmittance with increasing the optical thickness τ_0.

We begin with treating the ID problems of the frequency-dependent radiation transfer for different values of optical thickness. We limit ourselves with considering the case of complete redistribution of radiation over frequencies. Two cases are of interest: the medium is illuminated by monochromatic radiation of a given frequency and it illuminated by radiation of unit intensity in the continuum.

The basic equations for determination of the reflectance $r(x', x)$ and transmittance $q(x', x)$ are obtained with use of invariant imbedding approach (see,for instance, Ambartsumian (1944), Ambartsumyan (1960), Bellman et al. (1960), Chandrasekhar (1960), Nikoghossian (2012), Sobolev (1963)). In our case the coefficient r determines the reflectance of the medium from the side of the boundary τ_0 dependent on frequencies x', x of incident and reflected quanta (as usual, we deal with dimensionless frequencies, defined as the displacement from the line center measured in Doppler widths).

We have

$$\frac{dr}{d\tau_0} = -\left[\alpha\left(x\right) + \alpha\left(x'\right)\right] r\left(x', x, \tau_0\right) + \frac{\tilde{\lambda}\left(\tau_0\right)}{2}\varphi\left(x, \tau_0\right)\varphi\left(x', \tau_0\right) \tag{1}$$

where α is the profile of the absorption coefficient and

$$\varphi\left(x, \tau_0\right) = \alpha\left(x\right) + \int_{-\infty}^{\infty} r\left(x, x', \tau_0\right)\alpha\left(x'\right)dx' \tag{2}$$

Equation (1) satisfies the physically evident initial condition $r(x', x, 0) = 0$.

Turning to the transmittance q, we separate its direct and diffuse parts as follows

$$q\left(x', x, \tau_0\right) = \delta\left(x - x'\right)\exp\left[-\alpha\left(x\right)\tau_0\right] + \sigma\left(x', x, \tau_0\right), \tag{3}$$

where δ is the Dirac δ -function. Being applied the invariant imbedding procedure leads to integral-differential equation for the function $\sigma(x'x, \tau_0)$

$$\frac{d\sigma}{d\tau_0} = -\alpha\left(x\right)\sigma\left(x', x, \tau_0\right) + \frac{\tilde{\lambda}\left(\tau_0\right)}{2}\varphi\left(x, \tau_0\right)\psi\left(x', \tau_0\right), \tag{4}$$

with an initial condition $\sigma(x', x, 0)$=0. The function ψ appeared in Eq.(3) is given by the formula

$$\psi\left(x', \tau_0\right) = \int_{-\infty}^{\infty} q\left(x', x'', \tau_0\right)\alpha\left(x''\right)dx''. \tag{5}$$

Analogous integral-differential equation can be easily derived also for the reflectance of the medium from the side of the boundary $\tau = 0$. This quantity, however, is not of interest by its physical content in this particular case of inhomogeneity, especially for large optical thicknesses.

Let's turn now to analogous equations obtained by the same way for the 3D transfer problem where of primary interest for us is the spatial distribution of the reflected and transmitted radiation. Consider the diffuse reflection and transmission of monochromatic radiation for a plane-parallel finite atmosphere assuming, for simplicity, that the scattering is isotropic.

Following the notations adopted in Nikoghossian (2012), we introduce the reflection coefficient for the boundary τ_0, $\rho(\eta, \xi, \tau_0)$, where ξ is cosine of the angle of incidence and η is cosine of the reflection angle (the angles are counted from direction of the outward normal). It is introduced in such a way that the quantity $\rho(\eta, \xi, \tau_0)/\xi$ has a probabilistic meaning.

The function $\rho(\eta, \xi, \tau_0)$ satisfies the equation (see, Chandrasekhar (1960), Sobolev (1963))

$$\frac{d\rho}{d\tau_0} = -\left(\frac{1}{\eta} + \frac{1}{\xi}\right)\rho\left(\eta, \xi, \tau_0\right) + \frac{\lambda\left(\tau_0\right)}{2}\varphi\left(\eta, \tau_0\right)\varphi\left(\xi, \tau_0\right), \tag{6}$$

where

$$\varphi\left(\eta, \tau_0\right) = 1 + \int_{-\infty}^{\infty} \rho\left(\eta, \eta', \tau_0\right)\frac{d\eta'}{\eta'}. \tag{7}$$

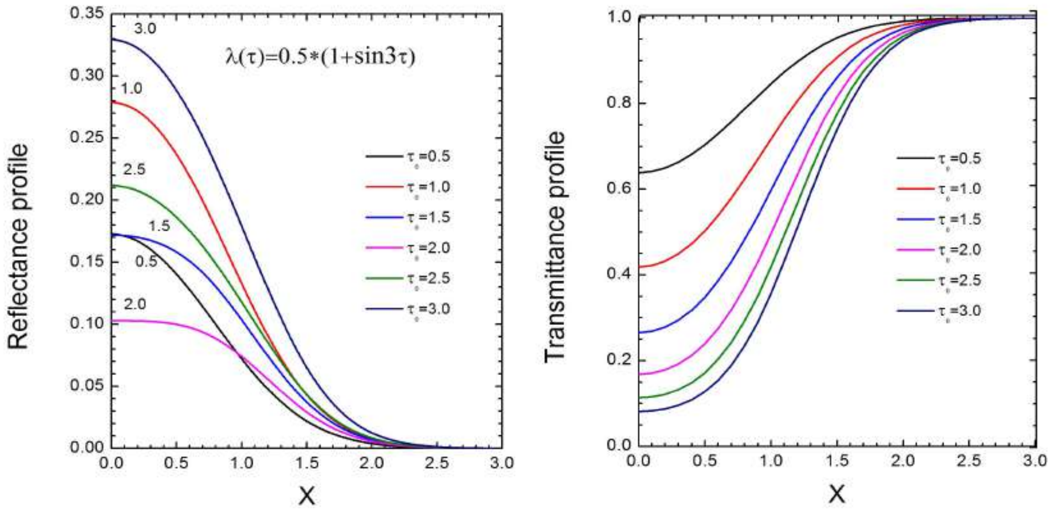

Figure 1. Reflected and transmitted lines profiles for media of different optical thicknesses illuminated by radiation in continuum.

with $\rho(\eta,\xi,0)=0$

Separating again the direct and diffuse parts in the transmission coefficient

$$q(\eta,\xi,\tau_0)=\xi\delta(\eta-\xi)\exp\left[-\tau_0/\xi\right]+\sigma(\eta,\xi,\tau_0)\,, \tag{8}$$

we arrive at the following differential-integral equation for the function σ

$$\frac{d\sigma}{d\tau_0}=-\frac{1}{\xi}\sigma(\eta,\xi,\tau_0)+\frac{\lambda(\tau_0)}{2}\psi(\eta,\tau_0)\,\varphi(\xi,\tau_0)\,, \tag{9}$$

where

$$\psi(\eta,\tau_0)=\int\limits_0^1 q(\eta,\eta',\tau_0)\,\frac{d\eta'}{\eta'}=\exp\left(-\frac{\tau_0}{\eta}\right)+\int\limits_0^1 \sigma(\eta,\eta',\tau_0)\,\frac{d\eta'}{\eta'} \tag{10}$$

The initial condition obviously is $\sigma(\eta,\xi,0)=0$

3. Numerical results.

We begin with results concerned the 1D frequency-dependent problem for the case when the boundary τ_0 of finite medium is illuminated by the continuum radiation of unit intensity. Fig 1 shows the evolution of observed reflected and transmitted profiles with increasing optical thickness. It is striking variations in the reflected profiles which change in unison with the changes in the scattering level within the medium. The oscillations remain discernable even for pretty thick media ($\tau_0\approx 3$). This effect is of interest in the sense that oscillations in the observed profiles are not related with any temporary changes in physical properties of the scattering and absorbing medium. Here the effect is due to inhomogeneity of the medium and to continuously varying opacity which in reality can be imagined as a stationary outflow of the matter from a star. The effect of inhomogeneity on transmitted profiles (right panel) is not so remarkable especially for high values of the optical thickness, which is tractable on the physical grounds.

Graphs of numerical results for monochromatic problem are depicted on Fig.2. We limit ourselves by demonstrating observed profiles only for the case when the medium is illuminated by monochromatic radiation in the center of the line. We see that the effect in the reflected profiles are similar to those discussed above.

Significant impact is discernable in transmitted emission profiles. The profiles response to the medium inhomogeneity is now both quantitative and qualitative. It is striking the appearance of

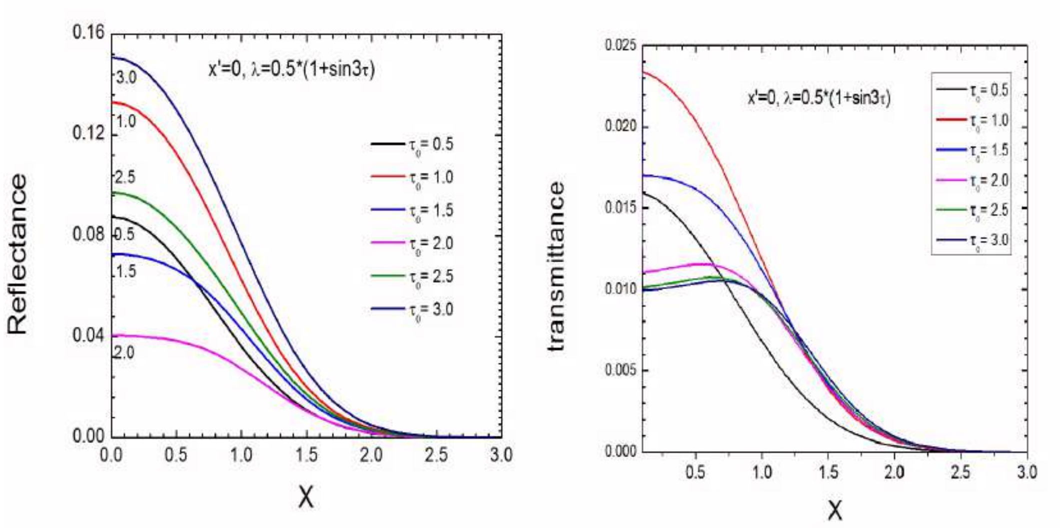

Figure 2. Reflected and transmitted lines profiles for media of different optical thickness illuminated by mono-chromatic radiation in the center of the line.

double-picked profiles. Now oscillations are observable not only in reflected but also in transmitted profiles. It is reasonable to expect such pictures are feasible in the cases of any kind irregular variations in physical properties of scattering medium.

Let us turn now to Figs.3, 4 and follow the spatial effect of scattering inhomogeneity. Fig. 3 exhibits the spatial distribution of the reflected and transmitted radiation for the case of mono-directional illumination of the boundary τ_0. It is supposed that the radiation falls in direction of the normal to the surface of the medium. Being plotted in polar coordinates the curves show the nature of aperture oscillations of observed radiations. We see that the effect is significant for both the reflected and transmitted radiation.

Similar calculations were performed assuming that the medium is illuminated by diffuse radiation of unit intensity. The results are depicted in Fig.4. Plots in Cartesian coordinates allow to better trace spatial oscillations of observed radiation with an increase of the optical thickness. it is noticeable that the character of the observed radiation changes depending on the angle of deflection from the normal direction is different for opaque and optically thin media.

4. Discussion

The paper may be regarded as a first attempt to find out the response of the observed line-radiation to inhomogeneity of the scattering and absorbing medium. We exemplify it by taking the scattering coefficient as a depth-varying characteristics of inhomogeneous medium. The periodic functional form of the law of its variation was chosen for reasons of clarity of the observed effect and, in principle, can be replaced by any other law describing irregular variations in physical characteristics of the medium. The importance of obtained results is due to the fact that, as we saw, the oscillatory radiation is not necessarily due to any kind of non-stationary phenomenon, but may be caused by some specific variations of physical conditions in the medium. We have seen that significant oscillations are subject to both reflected and transmitted fluxes. Astrophysical aspect of this problem is a matter of separate investigation involving radiation scattering in the continuum

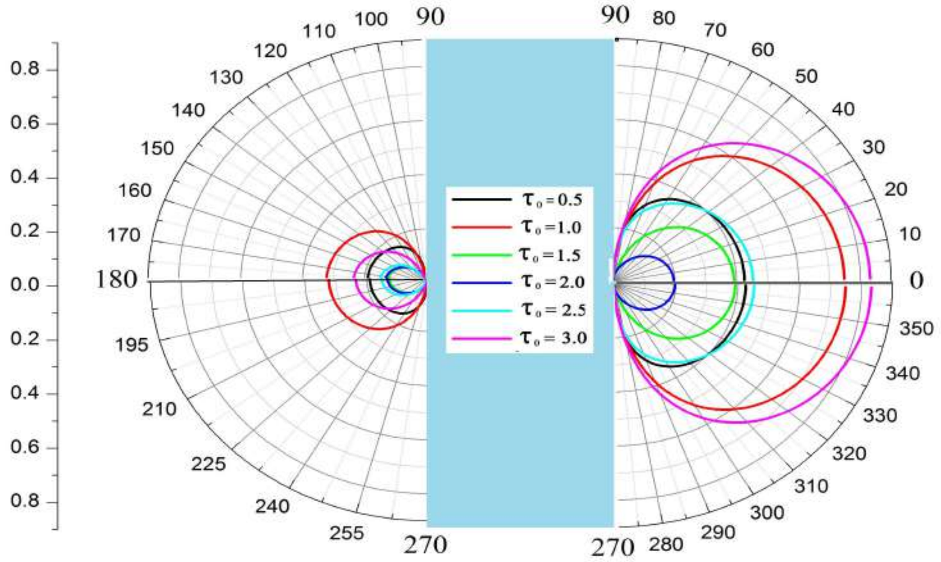

Figure 3. Spatial distribution of reflected and transmitted radiation for media illuminated by diffuse radiation.

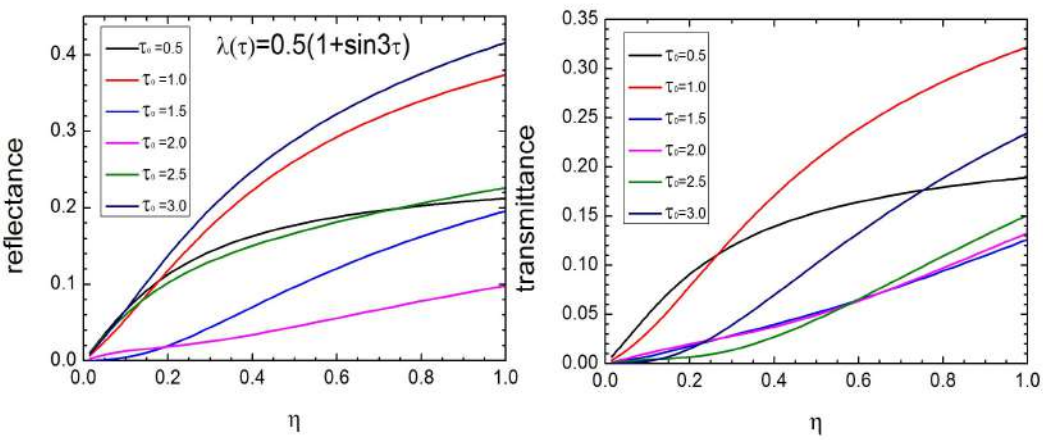

Figure 4. Spatial distribution of reflected and transmitted radiation for media illuminated by mono-directional radiation in direction of the normal to the surface.

References

Ambartsumian V. A., 1944, Izv. Akad. Nauk ArmSSR, N 1, 2

Ambartsumyan V. A., 1960, Scientific Works, V. I, Yerevan,Izd. Acad. Nauk ArmSSR

Bellman R., Kalaba R., Wing G. M., 1960, Journal of Mathematical Physics, 1, 280

Chandrasekhar S., 1960, Radiative transfer

Israelian G., Nikoghossian A., 1996, JQSRT, 56, 509

Nikoghossian A. G., 2012, Astrophysics, 55, 261

Nikoghossian A., Israelian G., 1996, JQSRT, 56, 501

Sobolev V. V., 1963, A Treatise on Radiative Transfer, Princeton: van Nostrand.,

Distribution of Elements Inside Stars

Alecian, G.*

LUTH, Observatoire de Paris, PSL, CNRS, Université Paris Diderot, 5 Place Jules Janssen, 92190 Meudon, FRANCE

Abstract

The chemical composition measured in stellar atmospheres is not necessarily the same as in deeper layers (outside the core). Indeed, for a significant fraction of main-sequence G to B types stars the discrepancies between superficial and internal abundances go from a few percent (for the coldest of these stars) to huge factors (for hot chemically peculiar stars). This is due to atomic diffusion process, which may produces elements segregation at some stages of the stellar evolution.

Keywords: *Stars, Abundances, Atomic diffusion*

1. Introduction

In standard modelling of stellar envelopes and atmospheres, abundance stratification in main-sequence stars was until recently generally neglected. This was often justified because mixing processes due to turbulence, convection, or large-scale circulation (including mass loss) keep the abundances uniform. Element stratification is due to atomic diffusion (see the pioneering work of Michaud 1970 for Ap stars), and proceeds with very large time scales in stellar interiors, but yet smaller than the structure's evolution time scale. For a *normal* and cool star like the Sun, the changes of abundances due to atomic diffusion below the outer convection zone, at the present age of the Sun, is estimated to be at most around 10% (Turcotte et al., 1998), which is very small (but not negligible) in comparison to what is observed for hot chemically peculiar stars (CP stars). However, even such a small effect leads, for instance, to reconsider previous estimates of the age of globular clusters. The abundance stratification build-up in the atmosphere is much faster (from a year to centuries according to the depth in the atmosphere and to the element) and stronger, provided that mixing processes are weak enough. In A and B type main-sequence stars, mixing processes are often weak enough (in particular for slow rotating stars and/or magnetic stars) to allow very effective element separation in upper envelopes and atmospheres. Many stellar types may be concerned by this process, but, here, we consider essentially main-sequence CP stars for which observational effects are striking. A large number of papers about atomic diffusion in stars have been published since 1970, the reader can find a complete presentation and discussion in the recent monograph by Michaud et al. (2015).

The chemically peculiar stars of the main sequence are divided in different groups (AmFm, ApBp, HgMn, etc.), their effective temperatures extend from about 7500K to 16000K, and more if one considers the hotter He-rich stars. About 10-30% of stars in this temperature range are concerned. Their abundance peculiarities are generally connected to atomic diffusion. Outside this temperature domain, convective motions are too strong for lower temperatures, and stellar wind too strong for higher temperatures to allow element segregation to occur. Actually, because abundance stratification build-up is extremely sensitive to physical conditions, these various groups correspond to various specific physical properties of them (mixing, mass loss, magnetic fields etc.). Figure 1 shows an overview of the peculiarities measured in each group. We may see for instance that in some HgMn stars, Hg may be overabundant by more a factor of 10^6. Of course, these peculiarities are located in some superficial layers, the total amount of an element inside the star being close to the solar one. When the star evolves and leaves the main-sequence, strong convective motions occur, all the matter is mixed and

*georges,alecian@obspm.fr

DOI: 10.52526/25792776-2019.66.1-52

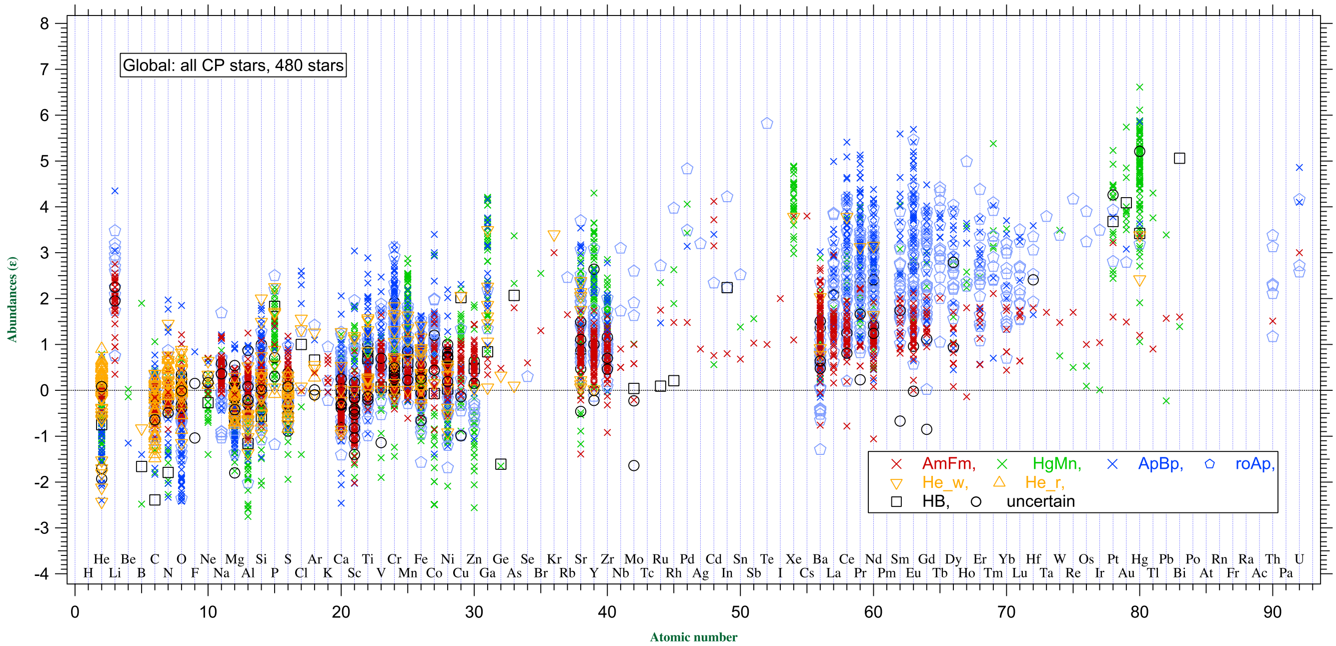

Figure 1. Abundance peculiarities vs. atomic number. Each point is the abundance measured in a CP star for a given element (480 CP stars measured with high resolution spectroscopy are shown here). Abundances (ϵ) are the logarithm of the abundances divided by the solar ones, the zero line corresponds to solar abundances (from the database of Ghazaryan et al., 2018, Ghazaryan et al., 2019). Notice that most of the dispersion of abundances from star to star are not due to errors of measurements.

no more peculiarities survive. This is why CP stars appear essentially on the main-sequence. Later in the evolution, it happens that mixing processes disappear close enough to the superficial layers, which causes element segregation to proceed again. This is the case for some horizontal branch stars and some white dwarfs.

2. The atomic diffusion process

Atomic diffusion is a microscopic process which, inside an anisotropic medium, results in relative average velocities of chemical elements with respect to hydrogen. These velocities are different from one species to the other, and they are generally very small compared to those of large scale motions. Therefore, this physical process that is calculated from first principles, requires a very stable medium to produce observable effects. One knows that this requirement is satisfied in many stars[1], not only because numerical models including diffusion are the only ones explaining some observed properties of stars, but because abundance stratifications are now well observed (Ryabchikova, 2005, Thiam et al., 2010). Such stratifications imply that the medium is not mixed, and so, atomic diffusion acts necessarily.

2.1. The diffusion velocity

The diffusion velocity in the formalism of Chapman & Cowling (1970) and for plane-parallel geometry may be expressed in simple algebraic form. In general case, it has a vectorial form. The relative velocity of a trace ion (with mass $A_i m_p$, where A_i is the ion atomic mass and m_p the proton mass) with respect to protons, in a very schematic and approximate way (only the dominant term is shown), may be written as:

[1]Radiative zones are, of course, theoretically predicted since a long time through the various stability criteria depending on local plasma condition, but hydrodynamic instabilities are also caused by rotation. In addition, the stellar mass loss, if strong enough, causes continuous matter flux that impedes abundance stratifications to appear.

$$V_{Di} \approx D_{ip} \left[A_i \frac{m_p}{kT} \left(g_i^{rad} - g \right) \quad + \quad \ldots \right], \tag{1}$$

where D_{ip} is the diffusion coefficient, g_i^{rad} the radiative acceleration, and g gravity. Because each element in a given layer, is generally in several ionization stages, an average diffusion velocity must be computed (weighted by the relative ions population). Notice the minus sign in front of g, which expresses the fact that radiative acceleration and gravity act generally in opposite directions. For detailed expression and discussion, see Chapter 2 of Michaud et al. (2015) (see also Alecian, 2014). Radiative acceleration accounts for the momentum transfer from the radiation field to atoms. It is due to absorption of photons by atomic transitions and is specific to each ion. In the absence of photoabsorption, one is left with gravitational settling. Strictly speaking, this only occurs in complete ionisation, very deep in the star, where diffusion time scales are often larger than stellar lifetimes on the main sequence. Radiative acceleration is generally in the range $10^{-2} < g_i^{rad}/g < 10^{+3}$! So, the sign of the diffusion velocity may be negative (small g_i^{rad}) or positive (large g_i^{rad}). More often, for metals with solar abundance, the modulus of radiative acceleration is larger than gravity. Radiative accelerations should be estimated each time atomic diffusion is suspected to have a significant effect on stellar structure.

2.2. Radiative acceleration

The momentum given by the radiation field to particles goes mainly through bound-bound and bound-free interactions of atoms with photons. Because the momentum due to isotropic part of the radiation field cancels, only the net photon flux has to be considered in the computation. Radiative acceleration, in its simplest generic algebraical form may be written as:

$$g_{rad} = \frac{1}{m\,c} \int_0^\infty \sigma_\nu \, F_\nu \, d\nu \,, \tag{2}$$

where the net outward radiative energy flux (F_ν), multiplied by total monochromatic absorption cross-section (σ_ν) for the considered species with mass m, is integrated over the radiation frequency. In the case of magnetic atmospheres, due to the polarisation of light, the vectorial form is required. Actually, to compute radiative accelerations is not an easy task. It necessitates taking into account all atomic transitions contributing significantly to the momentum transfer in each stellar layer, for any ion. This implies to consider huge atomic databases and to spend a lot of computer time. We do not go here in the details of this question, the reader can refer to Chapter 3 of Michaud et al. (2015), and many publications starting from Michaud (1970), Watson (1971). Notice also that F_ν, for frequencies contributing to the g_{rad} of a given element, depends on the local abundance of that element (the abundance which is precisely modified by atomic diffusion...).

To illustrate the importance of radiative accelerations, let us consider the case of a main sequence star ($T_{\rm eff} = 12\,000$K). The left panel of Fig. 2 shows the radiative acceleration of iron (solar abundance) and gravity (dashed line). For $\log T \approx 5.5$, the radiative acceleration is almost 10 times larger than gravity. This means that radiative acceleration is able to support up to about 100 times[2] the solar Fe abundance in these layers. The right panel shows, for the same star, how much the Rosseland averaged opacity increases when iron abundance is multiplied by 10 (dotted line). It appears that iron has a dominant contribution to the Rosseland average in the same layers where large overabundances of Fe can be supported by the radiation field.

In stellar atmospheres, and especially magnetic atmospheres, the computation of radiative accelerations is much heavier to carry out than for internal layers where the diffusion approximation (Milne, 1927) may be applied safely. In optically thin cases, these computations require to solve in detail the radiation transfer equations along the line profiles in each depth of the atmosphere (including the Zeeman effect for magnetic cases Alecian & Stift, 2004).

[2]Radiative accelerations of abundant elements vary as the inverse of the square root of the abundance. This is due to saturation of lines when Lorentz profiles (Alecian & LeBlanc, 2000) are assumed. The final overabundance of iron should certainly be lower than that maximum value. The real abundance will result from the complex time dependent non-linear build-up of the iron stratification (Richer et al., 2000).

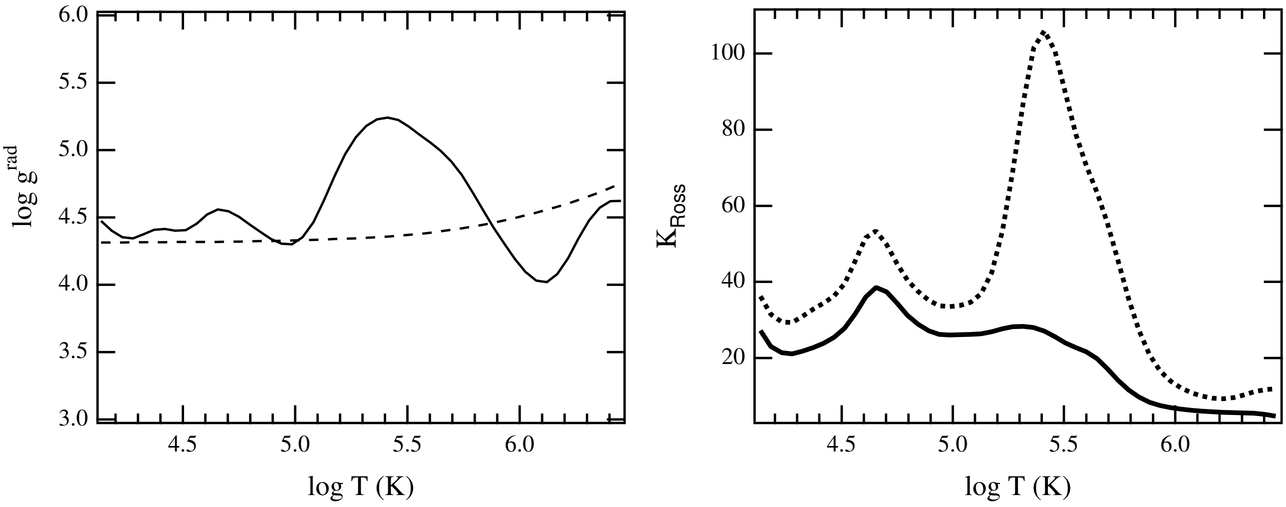

Figure 2. Left panel: radiative acceleration of Fe vs. layer's temperature (all in log). Dashed line is gravity. Right panel: Rosseland averaged opacity for solar (solid line) abundances and for 10 times the solar abundance of iron (dotted curve). The stellar model corresponds to a main sequence star with $T_{\rm eff} = 12\,000$K (from Alecian, 2007).

3. Build-up of abundance inhomogeneities and diffusion time scales

In stable medium, calculating the diffusion velocity of each element according to the depth is not enough in estimating what abundance may be found in a given stellar layer. In the 1970s, the first qualitative argument was to consider that elements that are strongly pushed up from deep layers to upper ones (positive velocity) may at least accumulate in the atmosphere. Indeed, some good correlations were found between elements with strong radiative acceleration and overabundances determined in the atmospheres of Ap stars (Michaud, 1970). Later on, more detailed calculations allowed in estimating for a given element, the maximum abundance that can be supported by the radiation field. This is equivalent to compute for each depth, for what abundance the radiative acceleration[3] has the same modulus as gravity. For such an abundance stratification, the diffusion velocity almost vanishes everywhere (and so also the particle flux). This is called the *equilibrium* solution.

3.1. Build-up of abundance inhomogeneities

Actually, to describe how abundances evolve according to the depth for an element k with particles number density n_k, one must solve the time dependent continuity equation that may be written as:

$$\partial_t n_k \; + \nabla \left[\mathrm{n_k} \cdot (\mathbf{V}_{\mathrm{D_k}} + \mathbf{V}_{\mathrm{M}}) \right] = 0\,, \tag{3}$$

where $\mathbf{V}_{\mathrm{D_k}}$ is the diffusion velocity specific to k, $\mathbf{V}_{\mathrm{M}}$ is the velocity of a macroscopic motion (the same for any k) like a wind, a large-scale circulation, etc. The *equilibrium* solution mentioned above is a particular stationary solution of this equation (assuming $\mathbf{V}_{\mathrm{M}} = 0$).

In stellar interiors, this equation (3) is solved all along the stellar evolution (see for instance Deal et al., 2016, Michaud et al., 2011, Théado et al., 2009).

For atmospheres, almost all quantitative results for abundance stratifications published before 2018, give *equilibrium* solutions (for instance Alecian & Stift, 2010, LeBlanc et al., 2009). Because these stratifications are simply solutions of Eq. 3 forcing $\partial_t n_k = 0$ and $\mathbf{V}_{\mathrm{M}} = 0$, there is no conservation of particle numbers. It corresponds just to the maximum abundance that can be supported by the radiation field in each layer. Actually, it is not trivial to know in which case, and for which element,

[3]Due to saturation effect on the line profiles, radiative acceleration decreases when element abundance increases.

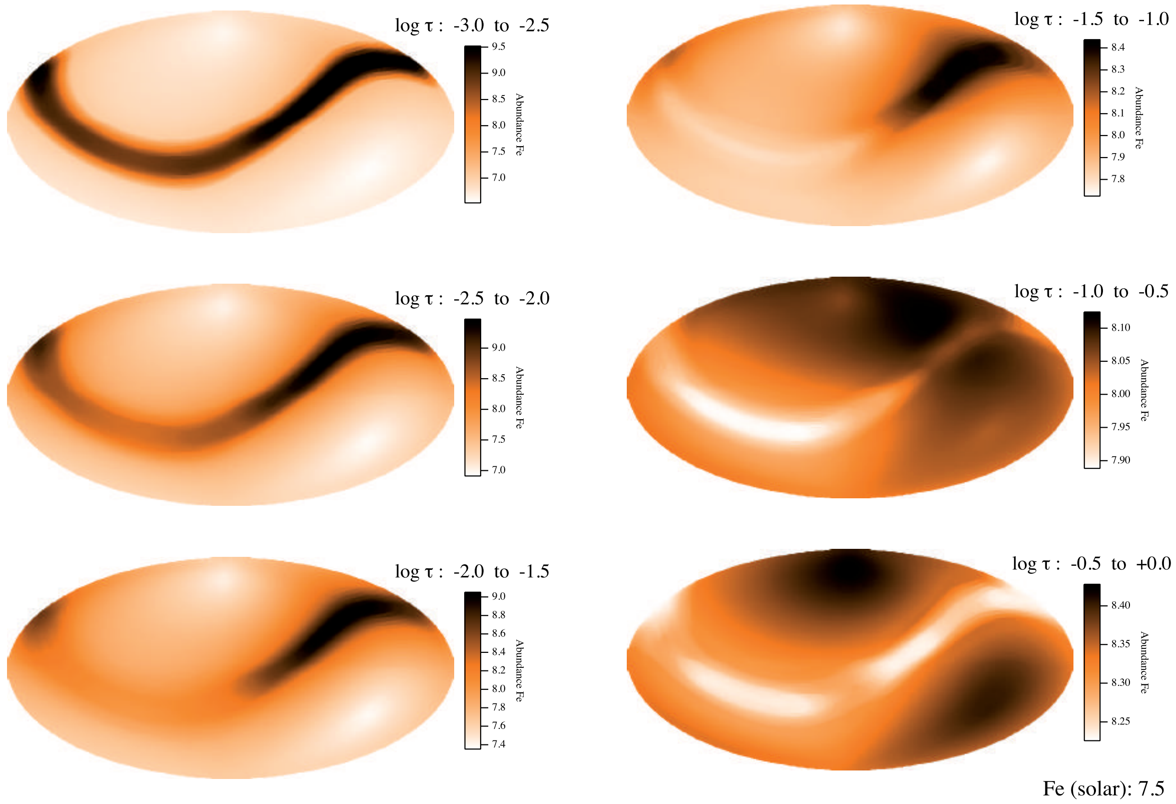

Figure 3. Tomographic view of the Fe abundance (Hammer equal-area projection) in a magnetic atmosphere (Alecian & Stift, 2017). Six slabs corresponding to six contiguous optical depth ranges (indicated above each projection) are shown. The solar abundance we adopted for Fe is 7.5.

equilibrium solution corresponds to what happens in real atmosphere. However, because these calculations of equilibria do not need extensive numerical resources, they allow to put more efforts in other aspects of the modelling, as for instance computation of the 3D abundances distribution in magnetic atmospheres for which some interesting results have been obtained (Alecian & Stift, 2017) as shown in Fig. 3.

A better approach, but numerically challenging and much more costly, is to solve the time dependent equation (with all the terms of Eq. 3) from an initial time when abundances are homogeneous, and let them evolve. This was done first for atmospheres (with and without magnetic fields) by Alecian et al. (2011), but still assuming $\mathbf{V}_{\mathrm{M}} = 0$. Stift & Alecian (2016) has shown that solutions of the time-dependent equation often converge (after a few decades of physical evolution time) towards stationary solutions (constant particle flux throughout the atmosphere). But these simulations never converge towards equilibrium, at least for the cases without numerical instabilities. Moreover these stationary stratifications are very different from those assuming equilibrium. One therefore wonders to what extent equilibrium solutions can be appropriate in describing real atmospheres. This question is still open. On another hand, one cannot exclude that some of the instabilities experienced during these numerical simulations are physical (Alecian et al., 2011) and could concern precisely evolution toward equilibrium solutions. Recently, a new step in these studies have been overcome by Alecian & Stift (2019) by introducing mass loss in that numerical simulations ($\mathbf{V}_{\mathrm{M}} \neq 0$) for atmospheres.

3.2. Time scales

It is interesting at this point to discuss the time needed for abundances to stratify. A characteristic diffusion timescale may be defined as the time needed for particles to diffuse along a pressure scale height. This quantity, which depends on the particle type and on local plasma conditions, is estimated after the computation of the diffusion velocity for that type of particle.

For atmospheres, typical atomic diffusion time scales are shown in Fig. 3.2 for Fe and Hg (from Alecian et al. 2011). One may notice that there is a large difference of the time scales of Hg compared to the one of Fe: mercury diffuses much faster than iron. This difference is mainly due to the fact that these timescales are computed at solar abundances: Hg has much lower abundance than Fe, and then has a stronger radiative acceleration. During the stratification process, the time scales will change according to the local abundances. Because the chemical stratifications build-up is strongly non-linear, the knowledge of these instantaneous time scales is not enough to estimate the time needed to form the observed concentrations of elements, but are helpful in estimating the efficiency of this transport process, especially if it has to be compared with macroscopic motions.

The timescales in Fig. 3.2 are strongly decreasing (several orders of magnitude) when one goes higher in the atmosphere (the higher the curves, the shorter the timescales). This is mainly due to the diffusion coefficient which varies as ${n_p}^{-1}$ (n_p is the number density of protons). Larger is the diffusion coefficient, shorter is the time scale. For Hg, one can see that the diffusion timescale at solar abundance is smaller than 1 month for $\log \tau < -3$. Therefore it seems possible that observed Hg overabundances in a HgMn stars could change significantly between two observations separated by a few years. Such a case was observed by Kochukhov et al. (2007). For deeper layers, the time scale continues to increase drastically, so much that it becomes larger than the age of the star (see an example in Alecian, 2009).

4. Conclusion

It is now well accepted in stellar community that the hypothesis of homogeneous abundances outside the stellar core for main-sequence stars was often wrong. Modelling stars with all processes involved in separating elements inside stellar medium is difficult since, atomic diffusion is a slow process and so, always confronted by several other mechanisms. However, a lot of theoretical/numerical works have been carried out since the 1970s, and this helped in much better understanding of elements distributions outside the core. For *normal* stars, discrepancies with standard models revealed by accurate asteroseismic observations are also better understood, since elements distribution change local opacities, which determine seismic behaviours.

Despite recent progress, atomic diffusion remains a difficult challenge for numerical modelling. It is not yet possible to reproduce theoretically the observed abundances of individual stars. However, theoretical models for atmospheres help in better explaining the strangeness of chemically peculiar stars: diversity inside a given group, stratification, horizontal inhomogeneity, dependence on magnetic fields, etc. Time-dependent simulation of atomic diffusion (including mass loss) appears to be very promising, and gives hope to be able to confront in a near future theoretical results in atmospheres with observations of CP stars.

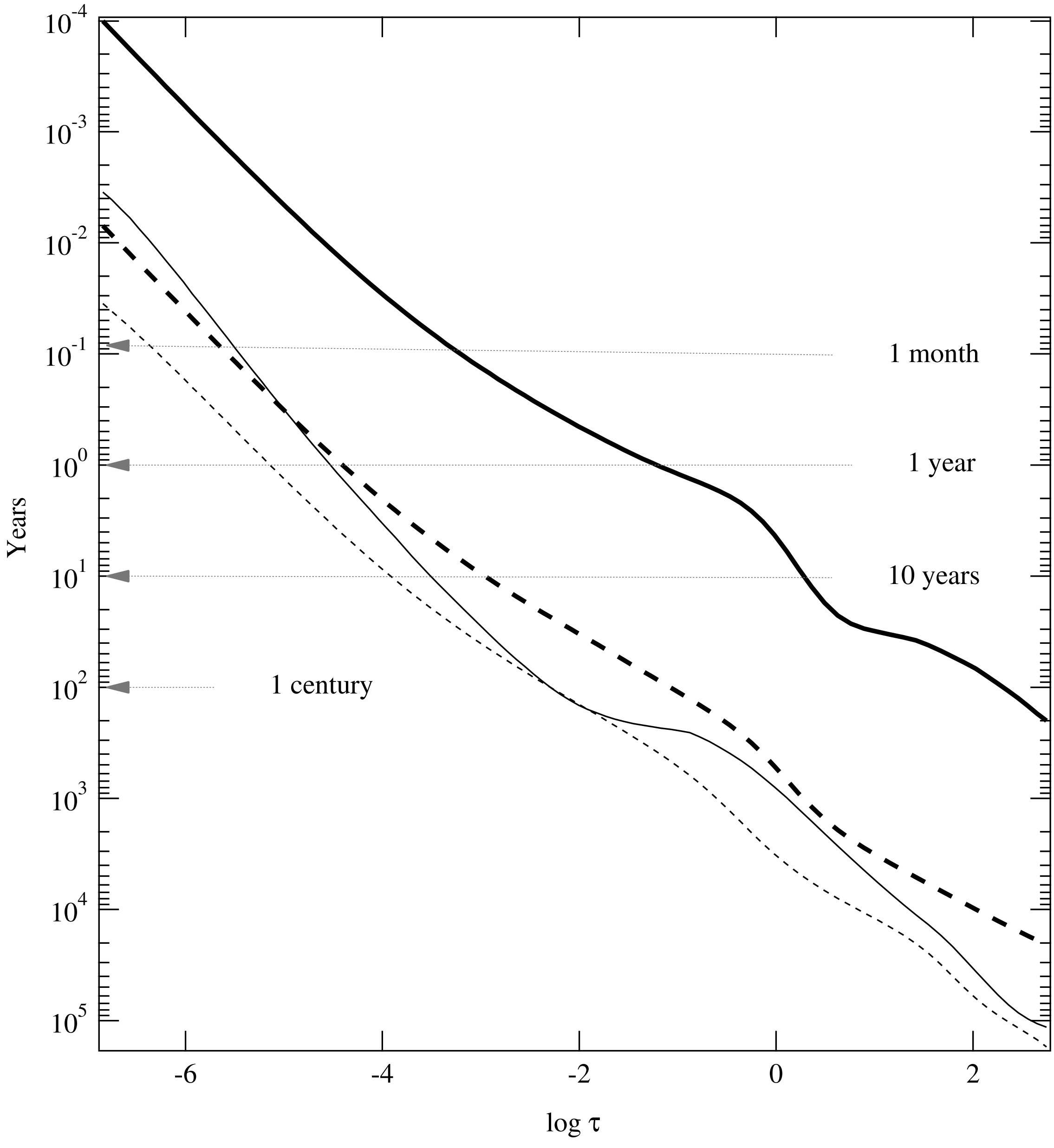

Figure 4. Diffusion time scales for Fe and Hg [log(years) vs. log(optical depth at 5000Å)] for a non-magnetic atmosphere with $T_{\rm eff} = 12000\,$K, $\log g = 4.0$. Solid lines correspond to the complete diffusion timescales, dashed lines to gravitational settling (diffusion without radiative acceleration). Heavy lines are for Hg, the others for Fe. (From Alecian et al. 2011).

Acknowledgements

The ComBAO would like to the thank the dedicated researchers who are publishing with the ComBAO.

References

Alecian G., 2007, in C. W. Straka, Y. Lebreton, & M. J. P. F. G. Monteiro ed., EAS Publications Series Vol. 26, EAS Publications Series. pp 37–48

Alecian G., 2009, Communications in Asteroseismology, 158, 34

Alecian G., 2013, in Alecian G. L. E. R. O. V. G., ed., EAS Publications Series Vol. 63, EAS Publications Series. pp 219–226

Alecian G., 2014, in Guzik J. A., Chaplin W. J., Handler G., Pigulski A., eds, IAU Symposium Vol. 301, IAU Symposium. pp 185–191

Alecian G., LeBlanc F., 2000, MNRAS, 319, 677

Alecian G., Stift M. J., 2004, A&A, 416, 703

Alecian G., Stift M. J., 2010, A&A, 516, A53+

Alecian G., Stift M. J., 2017, MNRAS, 468, 1023

Alecian G., Stift M. J., 2019, MNRAS, 482, 4519

Alecian G., Stift M. J., Dorfi E. A., 2011, MNRAS, 418, 986

Chapman S., Cowling T. G., 1970, The mathematical theory of non-uniform gases. an account of the kinetic theory of viscosity, thermal conduction and diffusion in gases

Deal M., Richard O., Vauclair S., 2016, A&A, 589, A140

Ghazaryan S., Alecian G., Hakobyan A. A., 2018, MNRAS, 480, 2953

Ghazaryan S., Alecian G., Hakobyan A. A., 2019, arXiv e-prints, MNRAS, in press

Kochukhov O., Adelman S. J., Gulliver A. F., Piskunov N., 2007, Nature Physics, 3, 526

LeBlanc F., Monin D., Hui-Bon-Hoa A., Hauschildt P. H., 2009, A&A, 495, 937

Michaud G., 1970, ApJ, 160, 641

Michaud G., Richer J., Richard O., 2011, A&A, 529, A60

Michaud G., Alecian G., Richer J., 2015, Atomic Diffusion in Stars, Astronomy and Astrophysics Library, Springer International Publishing, Switzerland.

Milne E. A., 1927, MNRAS, 87, 697

Richer J., Michaud G., Turcotte S., 2000, ApJ, 529, 338

Ryabchikova T., 2005, in Alecian G., Richard O., Vauclair S., eds, EAS Publications Series Vol. 17, EAS Publications Series. pp 253–262

Stift M. J., Alecian G., 2016, MNRAS, 457, 74

Théado S., Vauclair S., Alecian G., LeBlanc F., 2009, ApJ, 704, 1262

Thiam M., Leblanc F., Khalack V., Wade G. A., 2010, MNRAS, 405, 1384

Turcotte S., Richer J., Michaud G., Iglesias C. A., Rogers F. J., 1998, ApJ, 504, 539

Watson W. D., 1971, A&A, 13, 263

Study of variability of 2MASSJ10183905+0014078 stellar objects

E. C. Romas*

Observatory ISON-Kislovodsk, Russia

Abstract

This paper presents observational data for the star 2MASSJ10183905+0014078 (UCAC4 452-048383), in which so far no brightness variability has been detected. However, photometric observations made in 2015 allowed recording flare activity with an amplitude of 0.8 m for this star. The star parameters, namely magnitude and color index (V_0 = 7.59, $(B - V)_0$ = 1.19) and, therefore, the position on the Hertzsprung-Russell diagram, luminosity ($L_\odot$ = 0.1), spectral class (K7), mass ($M_\odot$ = 0.6), the spectral characteristics in the optical (Ca, Fe, Na D, Hα lines, Mg H, and TiO bands) and X-ray ranges allow us to classify the star as UVCet type object. The flash profile can be attributed to type II, with a relatively slow increase and decrease in brightness.

Keywords: *stars: variability - stars: UV Cet - stars: individual: 2MASSJ10183905 + 001407*

1. Introduction

Studies of such a phenomenon as stellar flare activity have a long history (Ambartsumyan et al., 1970, Gershberg & Shakhovskaya, 1973). At first the term "flare stars" has been used to designate dwarf K and M stars with transient optical brightening (UV Ceti stars). Further, improved detector performance and access to new spectral regions have led to detection of flare activity in many other kind of stars, including pre-main and post-main sequence stellar objects. From the point of view of modern concept about the physics of flare activity, it is believed that stellar flares are localized eruptions in magnetic fields, like on the Sun. In some cases, it is possible that we observe atmospheric reactions to mass transfer or other dynamic processes during flares. In all cases, the observations of flare stars never show any doubt that the cause of the observed light curve is the same as on the Sun. However, it cannot be ruled out that only the symptoms are similar, and at different stages of evolution, objects of different spectral types have different flash generation mechanisms (Pettersen, 1989).

A special place among the flare stars is assigned to UVCet-type dwarf stars with late K - M spectral classes, whose flares are similar to solar, but the energy emitted by them is several orders of magnitude greater than the energy of solar flares. Researchers flash profiles are divided into two main types. I-type flashes are short with a rapid increase in brightness and flashes of II-type, in which the increase and decrease in brightness occurs about 10 times slower (Smirnov, 2015).

This paper presents the observational data for the star 2MASSJ10183905+0014078 (UCAC4452-048383), in which so far no brightness variability has been detected. However, the photometric observations made in 2015 made it possible to register flare activity in this star.

2. Observations and data processing

The observations of 2MASSJ10183905+0014078 stellar object were performed at the ISON-Kislovodsk Observatory (MPC code D00) in 2015 on the night of March 18-19 during the search for variable

*romasastro@gmail.com

DOI: 10.52526/25792776-2019.66.1-60

stars on the GENON telescope (lens diameter 190 mm and focal length F = 295 mm) with CCD FLIML09000. The resolution of the received images is 8.4 "/pix. On the night of observations, from 18:00:05 UT to 20:20:06 UT, 250 images with an exposure of 30 sec, were obtained in the "C" filter (350 nm - 900 nm). HWFM of the received images is 9.8 "/ pix.

Three stars were used as photometric standards:

1) UCAC4-452-048393: V = 12.13 m, color index: 0.46

2) UCAC4-452-048389: V = 13.32 m, color index: 0.84

3) UCAC4-452-048353: V = 11.54 m, color index: 0.92

Initial image processing was performed according to the standard procedure using the MaximDL 5 program. With this program, the stellar magnitudes of objects were also measured. In determining the stellar magnitudes aperture radius, gap radius, and annulus radius were 3 pix, 4 pix and 8 pix, respectively.

In addition to our observations, we also used photometric parameters borrowed from some optical, infrared, as well as X-ray surveys and databases. These include Gaia DR2 (Gaia Collaboration et al., 2018), Fourth U.S. Naval Observatory CCD Astrograph Catalog (UCAC4, Zacharias et al. (2013), Sky Patrol All-Sky Automated Survey for Supernovae (ASAS), LAMOST DR4 catalogs, 2MASS, UKIDSS DR8 LAS (Lawrence et al., 2007), and 3XMM-DR5 (Rosen et al., 2016).

3. Main parameters

Fig 1 shows the image of 2MASSJ10183905+0014078 stellar object and Table 1 presents the main parameters of it.

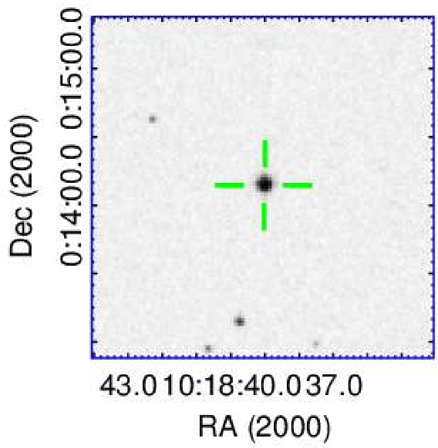

Figure 1. The image of 2MASSJ10183905+0014078 stellar object on the maps of DSS2 R survey.

Table 1. Main parameters of 2MASSJ10183905+0014078

UCAC4	**B**	**V**	**R**
	14.96	13.55	13.00
2MASS	**J**	**H**	**K**
	10.81	10.13	9.97
Gaia DR2	**Par**	**$L_\odot$**	T_{eff}
	8.9 mas	0.1	4029

According to the parallax value in Table. 1, the distance to the object is 112 pc, which corresponds to the distance correction for the absolute magnitude -5.25 m. Taking into account the value of interstellar absorption A_G = 0.705, also borrowed from the Gaia DR2 database, then V_0 = 7.59, and (according to the law of interstellar absorption Rieke & Lebofsky (1985)) $(B - V)_0 = 1.19$. This relationship between the luminosity of the star and its color index corresponds to the objects of the Main Sequence, which is reflected in Fig. 2, where our object is marked with a red circle. The photometric data of the near-infrared range also indicate that our stellar object does not exhibit an infrared excess. Fig. 2, borrowed from Pettersen (1989)), shows the Hertzsprung-Russell diagram (G-R), as well as the position of the flare stars. According to the color indices, the star has a spectral class K7. In the spectrum of the star from the LAMOST DR4 database, the Ca, Fe, NaD, Hα lines, and the MgH, TiO bands are distinguishable in the range from 4000 to 9000 Å (see Fig. 3).

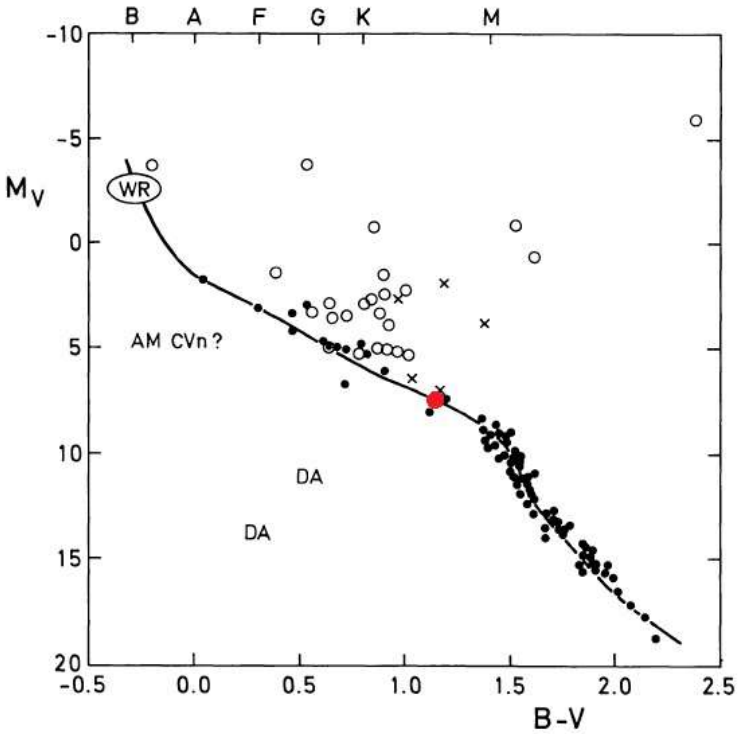

Figure 2. G-R diagram for flaring stars: black circles - flaring stars, crosses - young stars, open circles - giants. The red circle marks the position of 2MASSJ10183905+0014078 object.

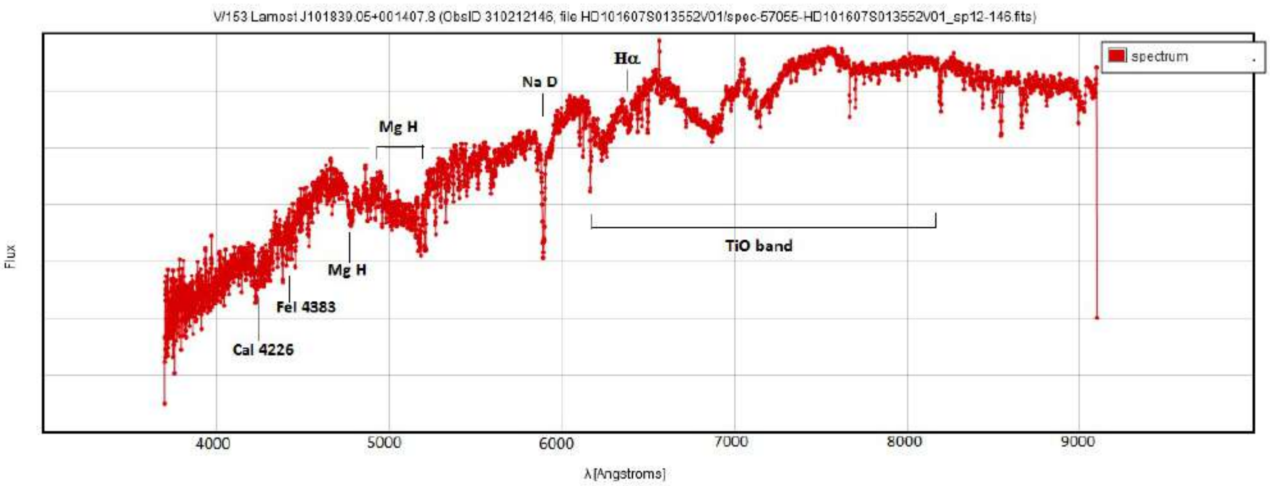

Figure 3. Spectrum of 2MASSJ10183905+0014078 from the LAMOST DR4 catalog.

According to isochrons models from Siess et al. (2000) and conversation tables from Kenyon & Hartmann (1995) for 2MASSJ10183905+0014078 with the L⊙ and T_{eff} values, which were borrowed

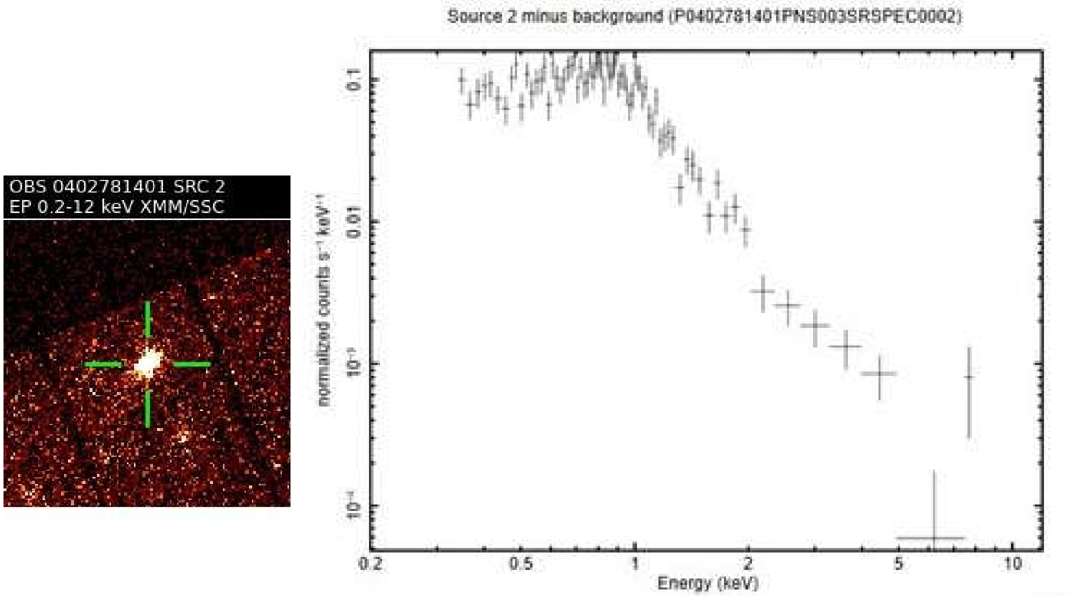

Figure 4. The image (left panel) and the spectrum (right panel) of 2MASSJ10183905 + 0014078 stellar object in the X-ray range from 3XMM-DR5 catalog.

from the Gaia DR2 data base, the mass estimate (for the solar metallicity model Z = 0.02) is 0.6 M$\odot$, which corresponds to upper mass limit of known UV Cet flare stars (Smirnov, 2015).

Like most flare stars, 2MASSJ10183905+0014078 also shows X-ray activity. On Fig. 4 the image and the spectrum of the object obtained in the X-ray range (3XMM-DR5 catalog) are presented.

4. Variability of 2MASSJ10183905+0014078

So far, the star 2MASSJ10183905+0014078 has not been identified as a variable. According to the ASAS data, this star showed only small fluctuations in the brightness of the order of 0.2 m in the V and g ranges. (see Fig. 5).

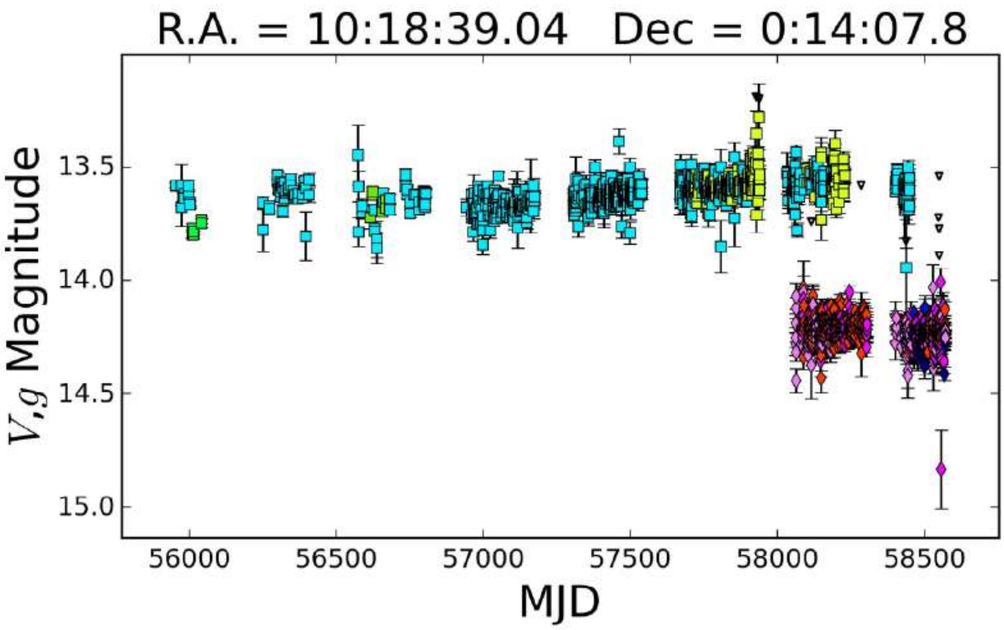

Figure 5. The light curve of 2MASSJ10183905+0014078 from the ASAS database.

However, our observations made on the night of March 18-19, 2015, revealed an outburst of brightness with amplitude of 0.8 m, which is shown in Fig. 6, where for comparison the light curves of standard stars are given. As can be seen from the data of photometric observations, the light curves of standard stars undergo only minor fluctuations, while the 2MASSJ10183905+0014078 shows a significant increase in brightness and its subsequent decline. Unfortunately, we were unable to continue the observations until the moment when the brightness of the object will drop to its original, basic level. However, according to the existing flash profile, it can be attributed to type II, with a relatively slow increase and decrease in brightness (Smirnov, 2015).

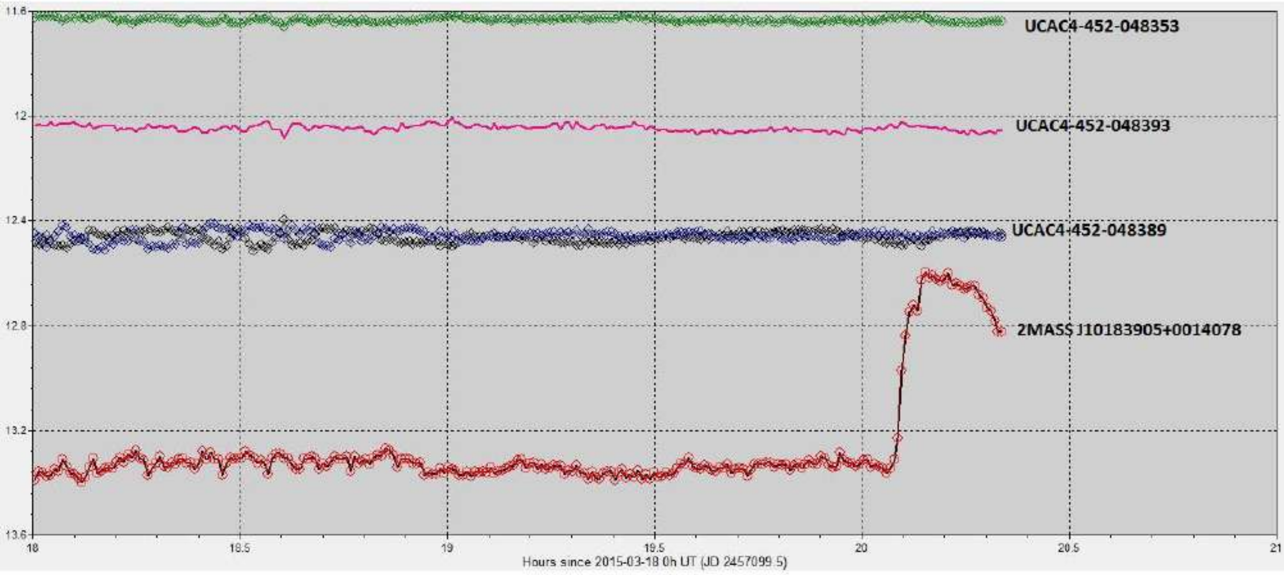

Figure 6. Light curves of 2MASSJ10183905+0014078, UCAC4-452-048353, UCAC4-452-048393, and UCAC4-452-048389 stellar objects, obtained on the night of March 18-19, 2015.

The study of archival data allowed in two other cases to reveal a significant fluctuation in the brightness of this star. First, this is the USNO B1 catalog data, according to which the brightness of a star in the R range on the maps of the First Palomar Atlas is ∼0.6 m higher than the brightness on the maps of the Second Palomar Atlas (DSS R1 = 12.59 m and DSS R2 = 13.18 m). However, in the B range, no noticeable difference in brightness is observed (DSS B1 = 14.84 and DSS B2 = 15.02). Secondly, the brightness variability in the near-infrared range. According to the magnitudes of the star in two infrared databases, namely 2MASS (epoch of observation 2000) and UKIDSSD R8 LAS (epoch of observation 2007), the brightness of the object in the H range also varied within 0.6 m (UKIDSS H = 10.77). In the other two bands are not observed significant differences (UKIDSS J = 11.84 and UKIDSS K = 10.18).

5. Discussion and Conclusion

Thus, photometric observations made on the night of March 18–19 in 2015 revealed a flash of brightness with an amplitude of 0.8 m in an unregistered until now as a variable 2MASSJ10183905+0014078 (UCAC4 452-048383) star. The star parameters, namely magnitude and color index (V_0 = 7.59, $(B - V)_0$ = 1.19) and, therefore, the position on the G-R diagram, luminosity ($L_\odot$ = 0.1), spectral class (7), mass ($M_\odot$ = 0.6), the spectral characteristics in optical (Ca, Fe, Na D, Hα lines, Mg H, and TiO bands) and X-ray ranges allow us to classify the star as UV Cet type object. The flash profile can be attributed to type II, with a relatively slow increase and decrease in brightness. Unfortunately, the observation period does not allow us to fully trace the decline in brightness to the initial level. Undoubtedly, the photometric and spectral studies of this object will be continued.

In conclusion, I would like to note the following. It is known that modeling of stars, even at rest is a challenge, which is still unresolved. And the modeling of flashing stars is important for several reasons. Presumably, flares, including those of the stars of type UV Cet, arise due to the magnetic field of the star. If, based on the parameters of stars, it would be possible to calculate the magnetic field, then it would be possible to compare the theory of the generation of a magnetic field and observations. This will undoubtedly greatly help us to fully understand the nature of flare activity. For this reason, the search for new flashing stars or observation of already known ones is of considerable scientific interest.

Acknowledgements

The author thanks E. Nikoghosyan for his assistance in writing the article.

References

Ambartsumyan V. A., Mirzoyan L. V., Parsamyan E. S., Chavushyan O. S., Erastova L. K., 1970, Astrophysics, 6, 1

Gaia Collaboration et al., 2018, A&A, 616, 1

Gershberg R. E., Shakhovskaya N. I., 1973, Nature Physical Science, 242, 85

Kenyon S. J., Hartmann L., 1995, ApS, 101, 117

Lawrence A., et al., 2007, MNRAS, 379, 1599

Pettersen B. R., 1989, Soph, 121, 299

Rieke G. H., Lebofsky M. J., 1985, ApJ, 288, 618

Rosen S. R., et al., 2016, A&A, 590, 1

Siess L., Dufour E., Forestini M., 2000, A&A, 358, 593

Smirnov A. A., 2015, "UV Cet type stars", St. Petersburg State University, pp 1–18

Zacharias N., Finch C. T., Girard T. M., Henden A., Bartlett J. L., Monet D. G., Zacharias M. I., 2013, AJ, 145, 44

TUIMP: The Universe In My Pocket. Free astronomy booklets in all languages

G. Stasińska*

LUTH, Observatoire de Paris, PSL, CNRS, UMPC, Université Paris Diderot, 5 place Jules Janssen, 92195 Meudon, France

Abstract

TUIMP (www.tuimp.org) is an international project to produce little astronomy booklets. These booklets, folded from just one sheet of paper, can be used in classrooms, at open public conferences, or during visits of observatories and planetariums. They are free to download from the internet, the only thing which is needed is a color printer (in absence of a printer, the booklets can also be directly consulted on line, even with just a mobile phone). The booklets are intended for children from nine years old and for anyone curious of astronomy. They are written in a simple language, amply illustrated, revised and translated by professional astronomers. So far, they are being published in six languages, others languages are to come. Everyone is invited to download the booklets and use them in their outreach activities.

1. Introduction

TUIMP stands for The Universe in My Pocket, in English. The characteristics of this outreach project are threefold. First, it does not require any funding and provides its products for free. Second, it allows anyone with an internet connection to download pdf files that can be printed and folded into small astronomy booklets. Third, it is open to all languages, in the hope of reaching populations that do not have much contact with astronomy.

2. Free

Even in the richest countries, outreach activities better reach their goals if they are free of charge. In less developed countries this is a necessity.

With TUIMP, all that is needed is a computer with an internet connection (and a printer).

3. Astronomy booklets

There are lots of sites for astronomy outreach on the internet. But people often like to have something to keep after a conference, a planetarium show or a school activity, so that they can remember or share their experience with their families.

TUIMP provides small 16-page booklets folded from one sheet of paper, free to download from the internet.

4. In all languages

In countries with a large number of professional astronomers many persons are available to devote part of their time to astronomy outreach. In countries where astronomy is not much developed, the few professional astronomers are facing a large number of challenges and responsibilities, and developing original outreach activities is difficult for them.

*grazyna.stasinska@observatoiredeparis.psl.eu

DOI: 10.52526/25792776-2019.66.1-66

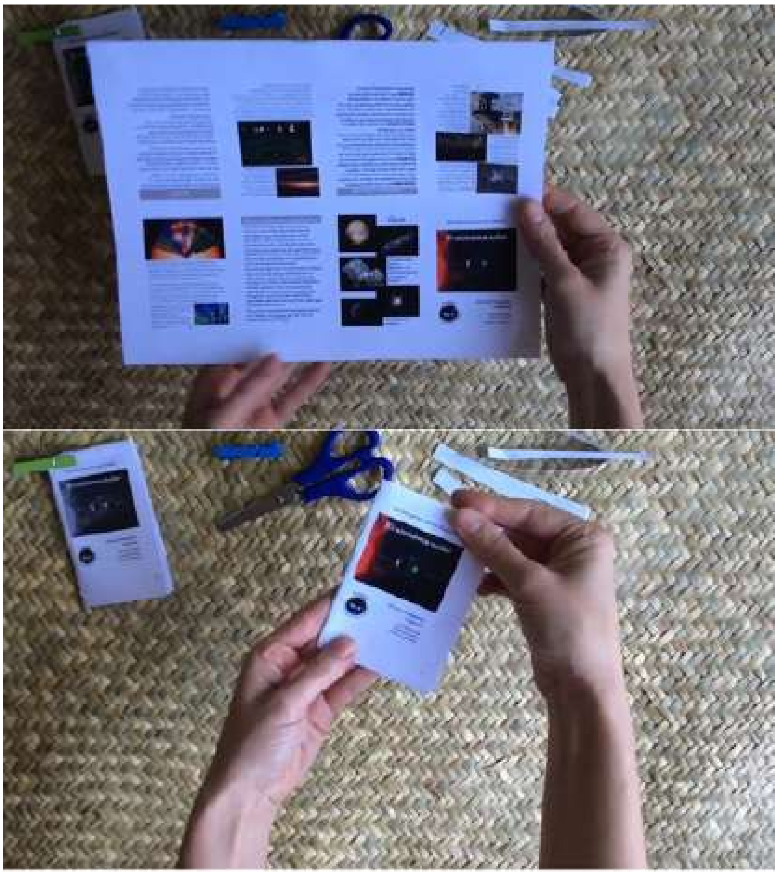

Figure 1. How to fold a booklet.

A photo by Wally Pacholka of the Pleiades constellation, that can be seen with the naked eye. For the aboriginal people of northern Australia, the Pleiades are a group of kangaroos that are chased by a pack of dingoes.

Galileo Galilei explains to the Doge of Venice how to use his telescope (Fresco by Giuseppe Bertini).

Galileo's drawing of the Pleiades as seen through his telescope. The small asterisks represent stars not seen without the telescope.

The first photograph of the Orion Nebula made by Henry Draper in 1880 with a 50 min. exposure using a telescope 28 cm in diameter.

2

The dawn of astronomy

In ancient times, knowledge of the Universe was limited to what the un-aided human eye could see. Myths and legends completed this view of the Universe.

At the beginning of the 17th century, the first telescopes allowed astronomers to detect objects several times weaker than the weakest ones seen with the naked eye. Hundreds of stars were discovered and a lot of nebulae were detected.

By the end of the 19th century, astronomical photography allowed a deeper exploration of space. One could follow an object with a telescope and record its light on a photographic plate during several hours. In this way, one could detect fine details on the planets and many nebular objects.

3

Figure 2. Two pages from the booklet "The invisible Universe".

Figure 3. The covers of two booklets, one in Albanese, the other in Spanish.

Ready-made outreach internet sites are numerous in English but are likely scarce in the majority of languages, except a few in which an active astronomical community is working.

TUIMP provides material written by professional astronomers that can be translated and used for free in any region of the World.

5. The target audience

The booklets are written with a wide audience in mind: children from nine years old but also any person curious about astronomy irrespective of their background. The language is simple, the texts are supported by numerous illustrations.

6. What makes the quality of TUIMP

The authors are professional astronomers. All the information and illustrations are taken from verified sources. There is an effort, in spite of very limited space, to put the astronomical material in a broader context and to touch on historical or sociological aspects. The scientific content is revised by external referees. To insure an accurate translation, the texts are translated by professional astronomers or astronomy students.

7. The languages of TUIMP

Booklets are presently available in Albanian, English, French, Polish, Portuguese, and Spanish. Translations are being prepared into Armenian, Greek, Italian, Nahuatl, Persian and Russian.

Clearly many more languages are wished for, especially from African and Asian countries.

8. Where can the booklets be used?

They are perfect for activities in the classroom. They have much success when distributed after open public conferences on a related topic. They can be made available to visitors in planetariums and observatories. They also make nice little gifts for relatives and friends.

9. The TUIMP team

Initially, the team was composed of just a few persons from different parts of the world: Fabricio Chiquio Boppré (Brazil), Gloria Delgado Inglada (Mexico), Mimoza Hafizi (Albania), Dorota Kozieł-Wierzbowska (Poland), Stan Kurtz (USA), Grażyna Stasińska (France), Natalia Vale Asari (Brazil). The team is growing, with astronomers from Greece, Italy, Iran, Armenia joining in. All the participants – including the webmaster – give their time for free.

New authors and translators are welcome to join us. For this they can visit www.tuimp.org and write to us using the contact form to be found on our site at http://www.tuimp.org/pages/about.

10. Conclusions

The TUIMP project has started off well. It needs now to find its public. It is crucial to introduce it to potentially interested people all over the world, i.e. educators, children and teen agers, students, scientific journalists, astronomy aficionados and anyone interested in science. For this, the international astronomical community can be of great help.

Catalog of cometary nebulae and related objects ($-42° < \delta < +60°$)

E. S. Parsamian*and V. M. Petrosyan

NAS RA V. Ambartsumian Byurakan Astrophysical Observatory (BAO), 0213, Armenia

Abstract

The catalogue of cometary nebulae and related objects is compiled using the known up to the publication date lists.

Keywords: *Cometary nebulae, coordinats, morphology*

1. Introduction

Among diffuse nebulae, a special group consists of cometary nebulae and related objects (arc or comma-shaped nebulae), a remarkable feature of which is their connection in most cases with T Tauri type variables or peculiar stars of spectral classes Be-Ae.

Strong continuous radiation was detected by Joy (1954) in the T Tauri type stars. Ambartsumian (1954) showed that the radiation is non-thermal in nature and that in T Tauri type stars there is a release of stellar energy into the outer layers of the star's atmosphere. Continuous emission - as this phenomenon was named by him - is non-stationary in nature and, as observations have shown, changes its intensity. Since the cause of the emission of cometary nebulae, apparently, are stars, it is undoubtedly that continuous emission somehow affects the emission of cometary nebulae.

The cometary nebulae were considered reflective, but Ambartsumian (1954) questioned the reflection as the only effective mechanism for the glow in the nebulae. Colorimetric studies of the brightest cometary nebulae NGC 2261, NGC 2245, Anon 6^h04^m, and others (see Johnson, 1960, Khachikyan & Parsamyan, 1964, Parsamian, 1962, 1963) showed that reflection is not the main or only mechanism for their emission. The detailed colorimetry of the nebula 2261 at BWM showed that:

1) In ultraviolet rays, the nebula is much brighter than a star.

2) The color index of the nebula everywhere?

3) Hubble's correlation is broken.

4) Inequality $m_n - m_s \geq -5 \text{ lg } sin\frac{\alpha}{4}$ is broken (Parsamian, 1963), where m_n is the integral brightness of the nebula, m_s - the stellar magnitude of the star, and α is the cometary nebula solution angle.

5) There is no correlation between changes in the star and the nebula.

Subsequently, some of these results were confirmed in papers by Johnson (1960) and Brück (1974). The most detailed spectral study was carried out for the cometary nebula NGC 2261 and the star-like object R Mon associated with the nebula (see, Dibay, 1966, Greenstein, 1948a,b, Greenstein et al., 1976, Herbig, 1960a,b, 1968b, Kazarian & -Vartanian, 1970, Kazarian & Terzan, 1972, Slipher, 1939, Stockton et al., 1975). The spectrum of the nebula has been shown to be unlike the spectra of ordinary diffuse nebulae. Strong continuous spectrum, emission and absorption lines of hydrogen, forbidden

*elma@sci.am, Corresponding author

DOI: 10.52526/25792776-2019.66.1-70

lines 3727 [OII] were detected (Greenstein, 1948a,b, Kazarian & Terzan, 1972). In the cometary nebula NGC 2579 (Pupis) the lines N1, N2 [OIII] was found as well (Mendez & Parsamyan, 1974).

The detection of forbidden lines N 1, N 2, and 3727 Å once again showed that cometary nebulae are not just reflective, but have their own sources of radiation.

The polarization of cometary nebulae and the stars associated with them has a radial character. This suggests that the reflection factor also plays a certain role, although, without knowing the true nature of the illumination of cometary nebulae, it is somewhat premature to attribute the radiality due only to reflection (Hall, 1964, Johnson, 1960, Khachikyan, 1958, Khachikyan & Kalloglian, 1962, Khachikyan & Parsamyan, 1964, Martel & Rousseau, 1963, Parsamian, 1963, Razmadze, 1960, Zellner, 1970).

It was shown in the paper by Vardanian (1964) that the directions of the axes of cometary nebulae coincide with the mean plane of polarization of the surrounding stars, whence it was concluded that such an orientation is caused by a general galactic or local magnetic field. Cohen (1974) showed that, unlike the usual nebulae, only cometary nebulae have infrared radiation at 10 microns. An infrared study of stars associated with cometary nebulae has been conducted by Cohen (1973a,b). An attempt was made to classify cometary nebulae according to the degree of hydrogen excitation and forbidden lines in Mendez & Parsamyan (1974). It was shown that among the spectra of cometary nebulae, there is some diversity from purely continuous, characteristic of purely reflective nebulae, to emission, resembling spectra of low-excited diffuse nebulae. Interestingly, the spectral types of stars associated with cometary nebulae do not correlate with the spectral type of nebulae.

2. On the classification of cometary nebulae and related objects

Cometary nebulae include nebulae that have at least some of the following characteristics:

1) Comet-shaped appearance.
2) Connection with a T Tauri star or with related objects.
3) Violation of the Hubbles relation.
4) Variability.

The classification of cometary nebulae and related objects was carried out by a number of authors (Badaljan, 1960, Dibay, 1970). The existing classification was not intended to find a connection between the objects included in the classification. This classification had the following form:

I	**II**	**III**	**IV**
The stars with a comma-shaped nebula (Z CMa)	Cometary nebulae (NGC 2261)	The stars with an arc-shaped nebula (T Tau)	Biconical cometary nebulae (Anon $6^h\,04^m$)

However, the discovery of the fuor V 1057 and the possibility of separating stars with P Cyg characteristics into the group of possible post-fuors allows us to approach the classification of cometary nebulae and related objects in a new way. As is well known, flare stars, T Tauri stars associated with comma or arc nebulae, and cometary nebulae are often found in star associations somehow linked to T Tauri stars. As shown by Ambartsumyan et al. (1970), approximately 25 percent of T Tauri type stars in the Orion association are simultaneously flare stars. Thus, it can be schematically represented that, in the course of their evolution, T Tauri stars can pass through the following stages:

T Tauri
- 1. flare stars
- 2. fuors, stars with comma- or arc-shaped nebulae
- 3. cometary nebulae

In this case, stages 2 and 3 are the shortest, and the stars associated with them are not always typical T Tauri stars. Thus, T Tauri stars evolve in different ways, but the common to them all, apparently, is the ejection process, which in some cases comes to light in typical flare stars, in others in the form of fuors, around which nebulae are then formed, third - in the form of cometary nebulae. Although the phenomenon can be described as a sudden rise of the stars luminosity, the causes and mechanisms may be completely different. So, in the case of flare stars, we have an ejection, the release of a certain portion of energy, and the stars after the flare quickly return to their previous state. In the case of fuors (Ambartsumian 1971), the process of increasing the brightness occurs more slowly, the released ultraviolet radiation can cause ionization of the medium, however, the nebulae formed in this case have a certain arc or comma shape. Given the above considerations, we propose the following classification:

I a	**I a**	**II a**	**II b**
Cometary nebulae of conical form (NGC 2261)	Cometary nebulae of the biconical form (Anon $6^h\,04^m$)	Comma-shaped nebulae (Z CMa)	Arc-shaped nebulae (T Tau)

The nebulae in the second group are often associated with stars that have characteristics of R. This group includes the well-known three fuors; It should be expected that among the above list will be unknown to us postfuors. Nebulae in the first group also have common properties; thus, the biconical form, characteristic of subgroup I b, is also found in a less pronounced form in subgroup I a as a "mirror" image of a nebula (NGC 2261, NGC 2245). Among cometary nebulae, 12% are biconical; among related objects, 30% are class II b.

3. Explanation to the catalog

The first attempt to search for "cometary" nebulae on the maps of the Palomar Atlas was carried out by Parsamian (1965). Over the years, this list has been replenished with new data, which included objects found by other authors. It is clear that when selecting objects of this kind only in appearance, the catalog will also include those that are not actually the same according to their physical nature, and also some will fall out of it, due to the orientation, which look somewhat different from the typical representatives. The best criterion should be spectral and colorimetric characteristics. Unfortunately, the latter are known only for a few bright objects. Therefore, this catalog can give the opportunity to select objects for spectral, infrared, polarimetric, colorimetric studies.

The catalog includes mostly objects with $-42° < \delta < +60°$ (see Appendix A). The size of nebulae (height of the cone) is of the order of $0.5' - 3.0'$. About 80% of nebulae have a positive color index. The angle of inclination of the axes of nebulae to the plane of the Galaxy is in the range from 0 to 60°. The cometary nebulae belong to the flat subsystem.

The DSS2 R images of the nebulae are given in Appendix B.The coordinate grid is marked on the images: X axis – RA (2000) and Y axis – Dec (2000).

Comments to the objects from the catalog are given in Appendix C.

Acknowledgements

The editorial board of ComBAO thanks H. A. Harutyunian and E. H. Nikoghosyan for the translation and preparation of the article.

References

Ahnert P., 1950, Astronomische Nachrichten, 278, 123

Ambartsumian V. A., 1954, Soobshcheniya Byurakanskoj Observatorii Akademiya Nauk Armyanskoj SSR Erevan, 15, 40

Ambartsumyan V. A., Mirzoyan L. V., Parsamyan E. S., Chavushyan O. S., Erastova L. K., 1970, Astrophysics, 6, 1

Apruzese J. P., 1975, ApJ, 196, 769

Aveni A. F., Hunter J. H. J., 1969, AJ, 74, 1021

Badaljan G. S., 1960, Akademiia Nauk Armianskoi SSR Doklady, 31, 261

Badaljan G., 1962, Astronomicheskij Tsirkulyar, 230, 4

Barnard E. E., 1907, ApJ, 25, 218

Bernes C., 1977, A&AS, 29, 65

Blanco V. M., 1962, PASP, 74, 330

Bohlin K., 1922, Astronomische Nachrichten, 216, 31

Brück M. T., 1974, MNRAS, 166, 123

Calvet N., Cohen M., 1978, MNRAS, 182, 687

Cederblad S., 1946, Meddelanden fran Lunds Astronomiska Observatorium Serie II, 119, 1

Claria J. J., 1974, AJ, 79, 1022

Cohen M., 1973a, MNRAS, 161, 85

Cohen M., 1973b, MNRAS, 161, 97

Cohen M., 1973c, MNRAS, 161, 105

Cohen M., 1973d, MNRAS, 164, 395

Cohen M., 1974, , 86, 813

Cohen M., Kuhi L. V., Harlan E. A., 1977, ApJL, 215, L127

De Boer K. S., 1977, A&A, 61, 605

Dibay E. A., 1966, Astron. Zh, 43, 903

Dibay E. A., 1970, Astron. Zh, 47, 907

Dorschner J., Gürtler J., 1963, Astronomische Nachrichten, 287, 257

Gahm G. F., Welin G., 1972, IBVS, 741, 1

Garrison L. M. J., Anderson C. M., 1978, ApJ, 221, 601

Glesekingn F., 1973, IBVS, 806

Glesekingn F., 1974, A&A, 31, 117

Grasdalen G. L., 1973, ApJ, 182, 781

Greenstein J. L., 1948a, Stars in Diffuse Nebulae. p. 19

Greenstein J. L., 1948b, ApJ, 107, 375

Greenstein J. L., Kazaryan M. A., Magakyan T. Y., Khachikyan É. E., 1976, Astrophysics, 12, 384

Gyul'Budagyan A. L., Amirkhanyan A. S., 1977, in "Flare Stars". pp 127–128

Gyul'Budagyan A. L., Magakyan T. Y., 1977a, Pisma v Astronomicheskii Zhurnal, 3, 113

Gyul'Budagyan A. L., Magakyan T. Y., 1977b, Doklady Akademiia Nauk ArmSSR, 64, 104

Hall R. C., 1964, ApJ, 139, 759

Haro G., 1953, ApJ, 117, 73

Haro G., 1971, IBVS, 565, 1

Haro G., 1972, IBVS, 714, 1

Haro G., Rivera Terrazas L., 1954, BOTT, 1, 3

Haro G., Iriarte B., Chavira E., 1953, BOTT, 1, 3

Herbig G. H., 1950, ApJ, 111, 11

Herbig G. H., 1957, ApJ, 125, 612

Herbig G. H., 1960a, ApJS, 4, 337

Herbig G. H., 1960b, ApJ, 131, 516

Herbig G. H., 1961, ApJ, 133, 337

Herbig G. H., 1968b, Contributions of Lick Observatory, 264

Herbig G. H., Harlan E. A., 1971, IBVS, 543, 1

Herbig G. H., Kameswara Rao N., 1972, ApJ, 174, 401

Hoffmeister C., 1949, Verzeichnis von 1440 neuen veranderlichen Sternen MIT Angaben uber die Art ihres Lichtwechsels.

Johnson H. M., 1960, PASP, 72, 418

Johnson H. M., 1966, AJ, 71, 224

Joy A. H., 1945, ApJ, 102, 168

Joy A. H., 1949, ApJ, 110, 424

Joy A. H., 1954, PASP, 66, 5

Kazarian M. A., -Vartanian K. V., 1970, ComBAO, 41, 46

Kazarian M., Terzan A., 1972, A&A, 17, 323

Khachikian E. E., Einatian D. A., 1975, ComBAO, 46, 43

Khachikyan E. E., 1958, ComBAO, 25, 67

Khachikyan E. E., Kalloglian A. T., 1962, ComBAO, 30, 45

Khachikyan E. E., Parsamyan E. S., 1964, ComBAO, 35, 71

Khachikyan E. E., Parsamyan E. S., 1965, Astrophysics, 1, 221

Kolotilov E. A., 1977, ATsir, 955, 1

Kuhi L. V., 1964, ApJ, 140, 1409

Landolt A. U., 1977, PASP, 89, 704

Low F. J., Johnson H. L., Kleinmann D. E., Latham A. S., Geisel S. L., 1970, ApJ, 160, 531

MacConnel 1968, ApJS, 16, 275

Martel M.-T. è., Rousseau J., 1963, Notes et Informations, 1, 33

Mendez M., Parsamyan É. S., 1974, Astrophysics, 10, 43

Merril P. W., Burwel C. S., 1949, ApJ, 110, 387

Merril P. W., Burwel C. S., 1950, ApJ, 112, 72

Minkowski R., 1946, PASP, 58, 305

Morgan W. W., Sharpless S., 1946, ApJ, 103, 249

Morgenroth O., 1939, AN, 268, 273

Osterbrok D. E., Sharpless S., 1958, PASP, 70, 399

Parenago P. P., 1954, Die Sternenwelt.

Parsamian E. S., 1962, Soobshcheniya Byurakanskoj Observatorii Akademiya Nauk Armyanskoj SSR Erevan, 30, 31

Parsamian E. S., 1963, Soobshcheniya Byurakanskoj Observatorii Akademiya Nauk Armyanskoj SSR Erevan, 32, 3

Parsamian E. S., 1965, Izvestiya Akademiya Nauk Armyanskoi, 18, 146

Penston M. V., Keavey P. M., 1977, MNRAS, 180, 407

Pik Sin 1962, Contr. Bosscha Obs., 15

Razmadze N. A., 1960, Bull. Abastuman Obs., 4, 322

Romano G., 1969, MmSAI, 40, 375

Rosino L., Romano G., 1962, Contrib. Asiago, 127, 1

Sanduleak N., 1971, PASP, 83, 95

Schwartz R. D., 1974, ApJ, 191, 419

Schwartz R. D., 1975, ApJ, 195, 631

Sharpless S., 1959, ApJS, 4, 257

Slipher V. M., 1939, PASP, 51, 115

Stockton A., Chesley D., Chesley S., 1975, ApJ, 199, 406

Struve O., 1962, S&T, 24, 67

Struve O., Rudkjøbing M., 1949, ApJ, 109, 92

Struve O., Swings P., 1948, PASP, 60, 61

Swings P., Struve O., 1940, ApJ, 91, 546

Swings P., Struve O., 1942, ApJ, 96, 254

Van den Bergh S., 1966, AJ, 71, 990

Van den Bergh S., Herbst W., 1975, AJ, 80, 208

Vardanian R. A., 1964, ComBAO, 35, 3

Welin G., 1976, IBVS, 1195, 1

Zellner B., 1970, AJ, 75, 182

Appendices

Appendix A Catalog of the nebulae

The designations in the catalog are as follows:
(1) – The number of nebula in the catalog.
(2) – Name of the nebula from other sources: *GM* (Gyul'Budagyan & Magakyan, 1977a,b); *Ber* (Bernes, 1977); *B* (Barnard, 1907); *DG* (Dorschner & Gürtler, 1963); *P* (Parsamian, 1965); *Ced* (Cederblad, 1946); *vdB* (Van den Bergh, 1966); *Sh* (Sharpless, 1959); *M* (Minkowski, 1946).
(3) – The cone height d of the nebula in arcmin.
(4) – The class according to the present classification
(5) – The photographic magnitude of the associated star.
(6) – The spectral type of the star.
(7) – The name of the star in the general catalog of variable stars or other sources: *GR* (Romano, 1969); *HRC* (Herbig & Kameswara Rao, 1972); *MacC* (MacConnel, 1968); *Bl* (Blanco, 1962); *H* (Haro, 1953, Haro & Rivera Terrazas, 1954); *Cl* (Claria, 1974); *vdBH* (Van den Bergh & Herbst, 1975); *SR* (Struve & Rudkjøbing, 1949).
(8) – References: 1 – Herbig & Kameswara Rao (1972); 2 – MacConnel (1968); 3 – Herbig (1960a); 4 – Blanco (1962); 5 – Gyul'Budagyan & Magakyan (1977a); 6 – Joy (1949); 7 – Barnard (1907); 8 –Bernes (1977); 9 - – Herbig (1960b); 10 – Kuhi (1964); 11 – Cohen (1973b); 12 – Dorschner & Gürtler (1963); 13 – Herbig (1950); 14 – Osterbrok & Sharpless (1958); 15 – Schwartz (1974); 16 – Schwartz (1975); 17 – Low et al. (1970); 18 – Badaljan (1960); 19 – Haro (1953); 20 – Dibay (1970); 21 - – Cohen (1973c); 22 – Cederblad (1946); 23 – Garrison & Anderson (1978); 24 – Hoffmeister (1949); 25 – Haro (1953); 26 – Parenago (1954); 27 – De Boer (1977); 28 – Morgan & Sharpless (1946); 29 – Merril & Burwel (1950); 30 – Haro & Rivera Terrazas (1954); 31 – Sanduleak (1971); 32 – Ambartsumyan et al. (1970); 33 – Morgenroth (1939); 34 – Herbig (1968b); 35 – Parsamian (1965); 36 – Van den Bergh (1966); 37 – Merril & Burwel (1949); 38 – Gyul'Budagyan & Magakyan (1977b); 39 – Calvet & Cohen (1978); 40 – Calvet & Cohen (1978); 41 – Mendez & Parsamyan (1974); 42 – Penston & Keavey (1977); 43 – Minkowski (1946); 44 – Hall (1964); 45 – Apruzese (1975); 46 – Cohen (1974); 47 – Gyul'Budagyan & Magakyan (1977a); 48 – Claria (1974); 49 – Ahnert (1950); 50 – Swings & Struve (1942); 51 – Pik Sin (1962); 52 – Van den Bergh & Herbst (1975); 53 – Struve & Rudkjøbing (1949); 54 – Joy (1945); 55 – Romano (1969); 56 – Landolt (1977); 57 – Welin (1976); 58 – Herbig (1957); 59 – Kolotilov (1977); 60 – Herbig & Harlan (1971); 61 – Haro (1971); 62 – Glesekingn (1974); 63 – Gahm & Welin (1972); 64 – Glesekingn (1973); 65 – Haro (1972); 66 – Cohen (1973a); 67 – Rosino & Romano (1962); 68 – Aveni & Hunter (1969).

N (1)	Name of nebula (2)	d (3)	Class (4)	m_{ph} (5)	Sp (6)	Name of star (7)	Ref (8)
1		0.4	Iia	17.3		HRC 1n, MacC H12	1, 2
2		0.5	Ia	15.0	A:5eα	L_kH_α 198, 11Rc 3n, V376 Cas	3
3		0.2	Iia	16.0−18.0			3
4		0.4	Iia	16.2	Geβ	HRC 5, B1 10, MacC H9	1, 2, 4
5		0.4	Ia				5
6	GM 33	0.6	Iia				5
7		0.2	Iia	15.4−17.0		LW Cas	
8	GM 55, Ber 53	1.3	Ia				5
9	GM 13	0.6	Ia				5
10		0.5	Iia	14.0	K2eα	L_kH_α 325, HRC 11n	1
11	GM 14	0.7	Ia				5
12	GM 15	0.4	Ia				5
13	GM 68	0.3	IIa				5
14	B 10, IC 359			14.1−15.0	dK6e	DD Tau, HRC 30n	6, 35
15		1.1	IIa				
16	B 96, Ber 73, DG 30	2−3	Ia	9.3−12.3	dF8e−dG2e	RY Tau, HRC 31n	1, 7, 9, 10, 11
17	NGC 1555-4, DG 31		IIa	9.5−13.5v	K1e	T Tau, HRC 35n	5, 10 − 17
18			IIa	11.5−14.0	G:e	DG Tau, HRC 37	1, 6, 18
19	Ber 81, DG 39		IIa	13.0−15.2	K5(e)	GK Tau, HRC 57n, H6−22	1, 8, 12, 19
20	Ber 83, DG 41		IIa	14.0−17.2		HP Tau, L_kH_α 258, HRC 66n	1, 8, 12,18
21		0.6	IIa	12.4−16.5	G:e	DO Tau, HRC 67n	1, 35
22		0.5	IIa				
23		0.5	Ia	9.3−11.5	G2neIII	SU Aur, HRC 79n	1, 3, 11
24	GM 3		IIa				5
25	GM 36	0.4	IIa				5
26	GM 37	0.3	IIa				5
27	GM 38	0.3	IIa				5
28	P 1	1.1	IIa	11.9	B2		20
29	B 122, Ber 89, Ced 51	3−5	Ia	11.1−13.3	A4ep	HK Ort, HRC 94n	6, 7, 8, 19, 21, 22, 23, 24
30	GM 16	0.4	Ia				5
31	GM 17	0.6	IIa				5
32		0.3	Ia	9.6−13.8	A3:eα+shell	TȮri, H4̇−123, HRC 154n	3, 21, 23, 25, 26
33		0.7	IIa	10.7−17.8	eα	H 4−218,V 582 Ori	
34	NGC 1999	1.5	IIa	9.8−10.5v	A1:e	V 380 Ori, BD +6° 1253, HRC 164n	1, 3, 21, 23, 27, 28
35	GM 39	0.3	IIa				5
36	GM 40	0.4	IIa				5
37	H 13a	0.8	IIa				25
38		0.4	Ia	10.5−14.2	A2eII−III	RR Tau, HD 245906a	3, 21, 23, 29

(1)	(2)	(3)	(4)	(5)	(6)	(7)	(8)
39		0.3	IIa	15.0	eα	HRC 176n, H 4−255	1, 25
40	GM 66		IIa				5
41	P 2	0.6	IIa				5
42	Ber 131		Ia	13.0	G−Ke	HRC 182n, H 7−12, San 6	30, 31
43			IIa	9.7−16.5	F2:peαI-II	FU Ori, HRC 186n	27, 32 − 34
44	Ber 106	0.8	IIa				
45			Iia				
46	P 3, Ber 59, vdB 62	1.6	Ia		K2	BD+1°1156	8, 35, 36
47	GM 18	0.3	Ia				5
48	P 4	1.0	Ia				5
49			Iia	9.7	B9eq	HRC 192n, HD 250550	4, 21, 23, 67
50		1.0	IIa				38
51		2.3	Ia				
52		0.5	Iia				
53	P 5	1.3	IIa				35
54	P 4, Anon $6^h\,04^m$, P 6	2.0	Ia	13.0	FOV	HRC 193n, L_kH_α 208	1, 3, 21, 23, 35, 39
55	P 8, Ced 71, vdB 74	1.0	Ia		B6	BD+6°1414	22, 35, 36
56	P 9	0.6	Ia				35
57	Sh 258	1.1	Ia				40
58	GM 45	0.8	Iia				5
59	P 10, M 3, Sh 259	3.0	Ia		B6e		35, 40, 41, 43
60	P 11, DG 97	0.7	Ia				12, 35
61	P 12, DG 98	1.2	Ia				12, 35
62	P 13, NGC 2245,DG 108	3.5	Ia	10.7	Be+shell	L_kH_α 215	3, 12, 21, 23, 35
63	GM 20	0.4	Ia				5
64	NGC 2261	3.0	Ia	11.3−13.8	A−Fpe	R Mon, HRC 207n	1, 3, 17, 21, 23, 45
65	P 15	1.0	Ia	12.8−14.1	A5V−F8V		35, 39, 46
66	P 16	0.6	Ia				35
67	P 17, NGC 2313	1.1	Ia	15.7			35, 41
68	P 18, NGC 2316	1.6	Ia				34, 45
69		0.4	Ia				
70		0.5	Ia			CI 70	57
71		0.7	IIa	8.8−11.2	eq	Z CMa, HRC 243n	1, 2, 21, 23, 37, 48, 45, 50
72	NGC 2327, DG 135	1.6	Ia		B5V	L_kH_α 231, CI 81	8, 12, 48
73	GM 21	0.4	IIa				5
74	GM 22	0.3	Ia				5
75	P 19	0.8	Ia			BD−16°2003	35
76		0.7	Ia				
77	P 20, M 5, Sh 307	1.1	Ia				35, 40, 43

(1)	(2)	(3)	(4)	(5)	(6)	(7)	(8)
78	NGC 2579	1.5	Ia			vdBH−13a	41, 52
79			Ia			vdBH−47c	52
80			Ia	10.5r		vdBH−65a	52
81		0.7	Ia	15.0	Geα	HRC 248n	1, 51
82		0.2	Ia		eα	SR−24, HRC 232n, H 1−7	1, 5, 14
83	GM 47	0.8	Iia				5
84	GM 48, Ber 1, DG 144	0.8	Ia				5
85	GM 24	0.1	IIa				5
86	GM 56	1.7	Ia	10.0−11.6			5
87	NGC 6729	1.7	IIa	13.5	FO+pe	RCrA, HRC 288n, Ced 165c	1, 22, 54
88	P 21	1.1	Ia		A5eα		35, 46
89	NGC 6829, GM 26	0.9	Ia				5
90	GM 27		Ia				5
91		0.1	IIa	15.4−18.5	eα	L_kH_α 225, GR 168	3, 55
92		0.3	Iia	13.5		V 1515 Cyg	46, 47
93	GM 10		Ia				5
94	GM 11		IIa				5
95	P 22		IIa	17.0			5
96	GM 28	1.1	Ia				5
97	GM 29	0.8	Ia				35, 46, 39
98		0.5	IIa	12.2	GO	V 1057 Cyg, L_kH_α 190	32, 47, 56 − 66
99	Ber 29		IIa	11.8−12.2	eα	L_kH_α 120, HRC 302n, V 1331 Cyg	10, 42
100		0.8	Ia	17.0−17.7		RR−10	67
101	GM 12		Ia				5
102	GM 57	0.8	IIa				5
103		2.3	Ia	14.5	A7eα	L_kH_α 233, HRC 313n	1, 3, 39
104	GM 79	0.7	Ia				5
105		1.0	Ia	12.4−14.6	F8:eα	BM And, HRC 318n	1, 11, 68
106	P 23	1.1	IIa		eα	L_kH_α 259, HRC 321n, MacC H 4	1, 2, 4

Appendix B Images of the nebulae

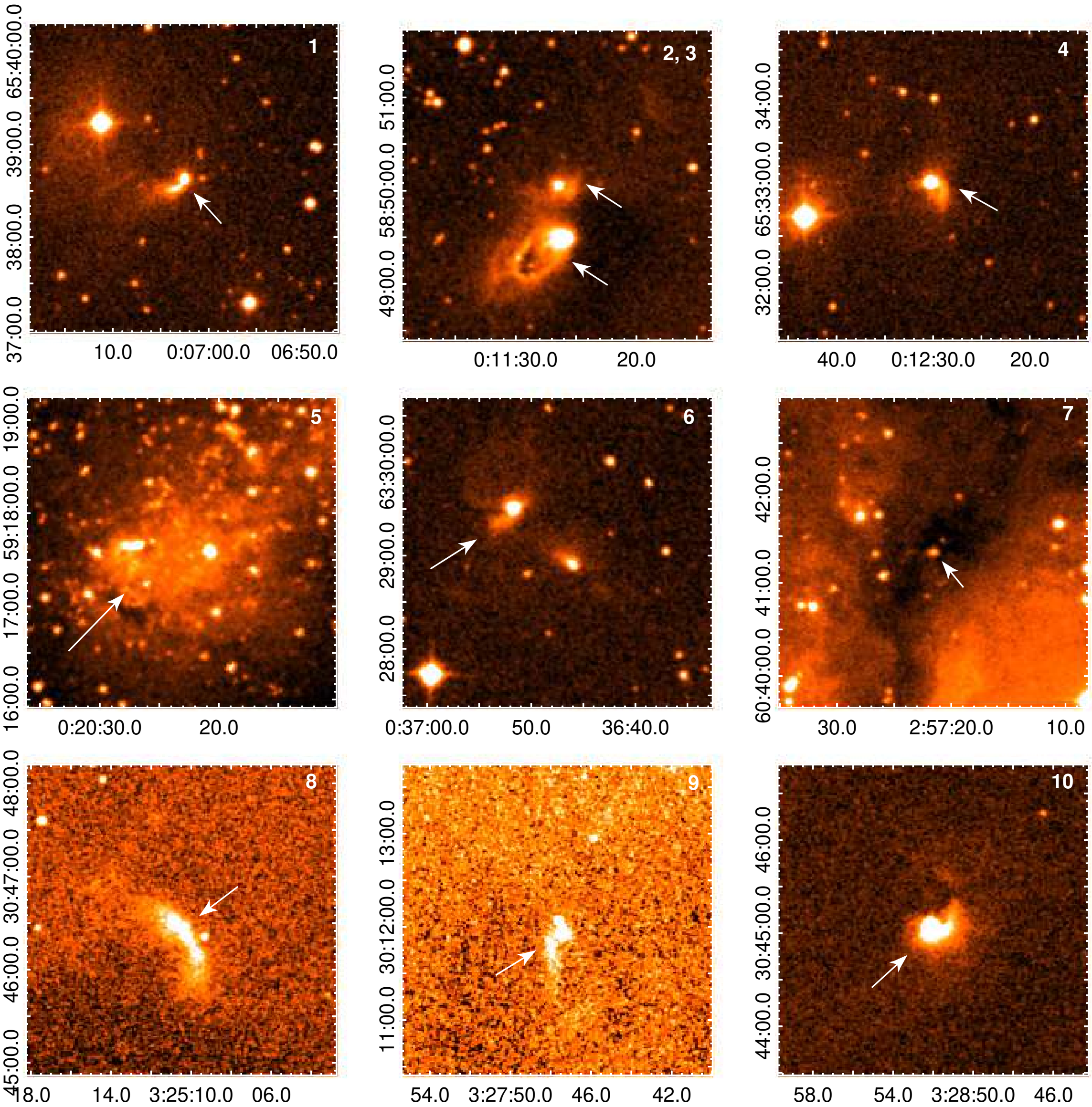

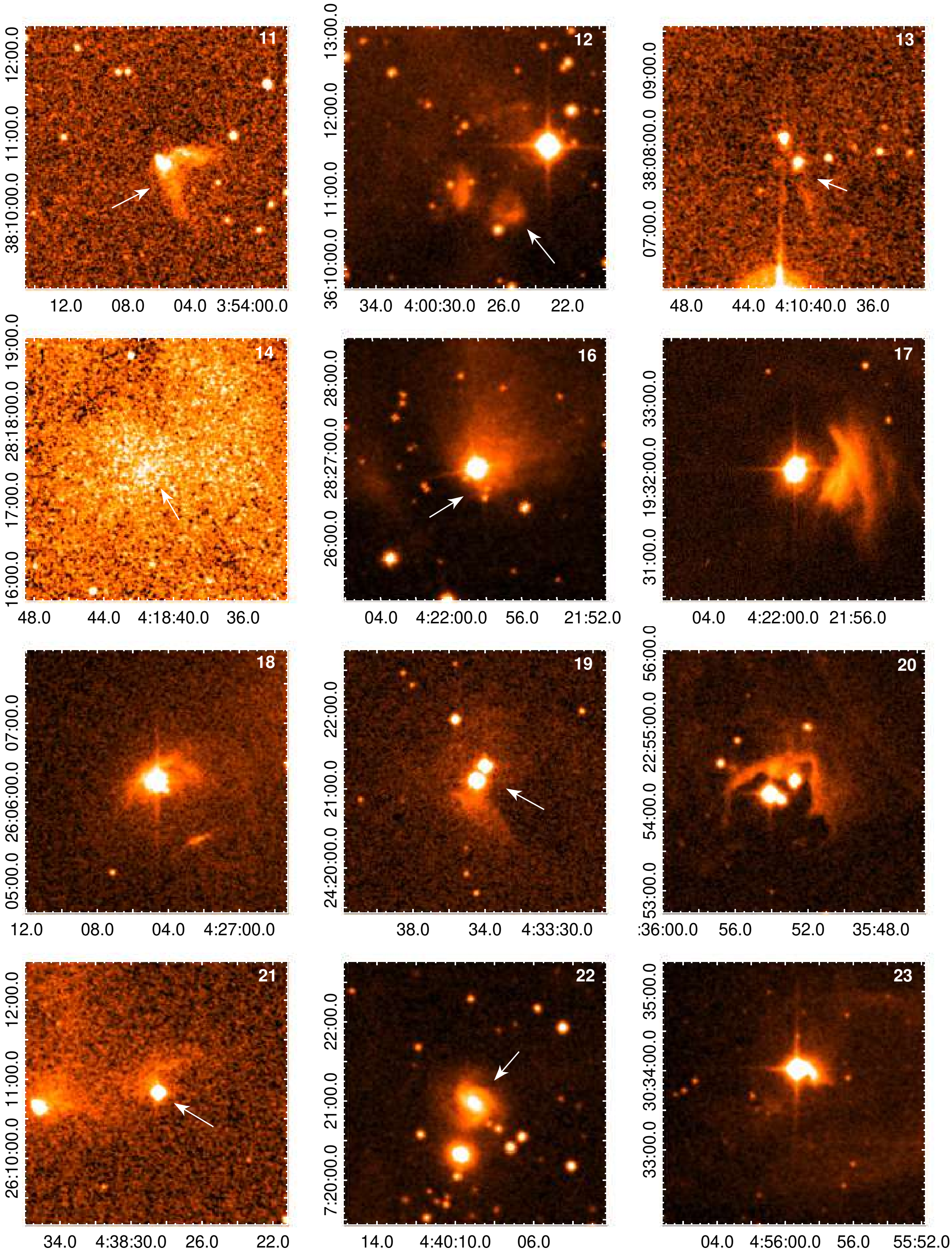
11
12
13
14
16
17
18
19
20
21
22
23
12.0 08.0 04.0 3:54:00.0
38:10:00.0 11:00.0 12:00.0
34.0 4:00:30.0 26.0 22.0
36:10:00.0 11:00.0 12:00.0 13:00.0
48.0 44.0 4:10:40.0 36.0
07:00.0 38:08:00.0 09:00.0
48.0 44.0 4:18:40.0 36.0
16:00.0 17:00.0 28:18:00.0 19:00.0
04.0 4:22:00.0 56.0 21:52.0
26:00.0 28:27:00.0 28:00.0
04.0 4:22:00.0 21:56.0
31:00.0 19:32:00.0 33:00.0
12.0 08.0 04.0 4:27:00.0
05:00.0 26:06:00.0 07:00.0
38.0 34.0 4:33:30.0
24:20:00.0 21:00.0 22:00.0
:36:00.0 56.0 52.0 35:48.0
53:00.0 54:00.0 22:55:00.0 56:00.0
34.0 4:38:30.0 26.0 22.0
26:10:00.0 11:00.0 12:00.0
14.0 4:40:10.0 06.0
7:20:00.0 21:00.0 22:00.0
04.0 4:56:00.0 56.0 55:52.0
33:00.0 30:34:00.0 35:00.0

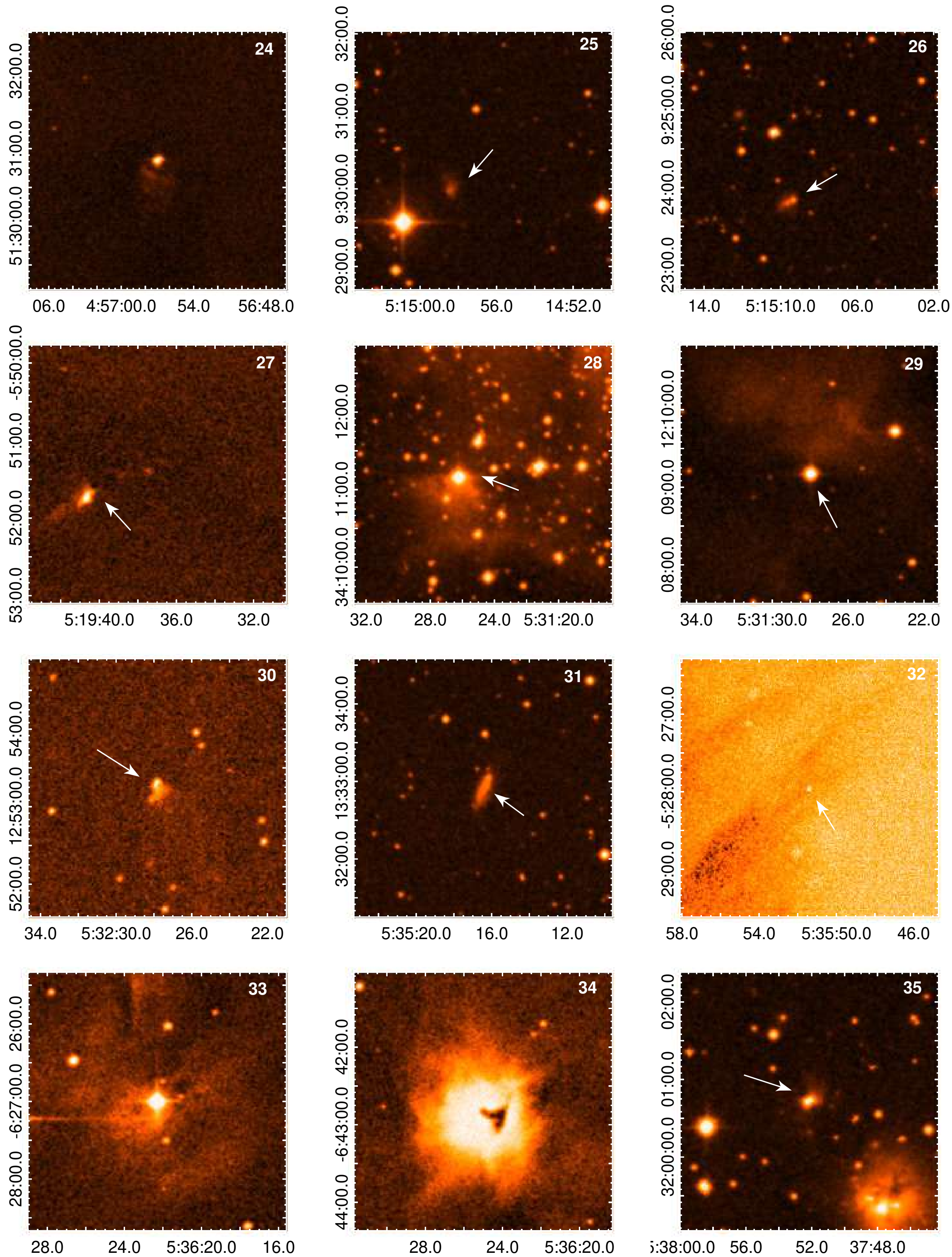
24
51:30:00.0
31:00.0
31:00.0
32:00.0
06.0
4:57:00.0
54.0
56:48.0
25
29:00.0
9:30:00.0
31:00.0
32:00.0
5:15:00.0
56.0
14:52.0
26
23:00.0
24:00.0
9:25:00.0
26:00.0
14.0
5:15:10.0
06.0
02.0
27
53:00.0
52:00.0
51:00.0
-5:50:00.0
5:19:40.0
36.0
32.0
28
34:10:00.0
11:00.0
12:00.0
32.0
28.0
24.0
5:31:20.0
29
08:00.0
09:00.0
12:10:00.0
34.0
5:31:30.0
26.0
22.0
30
52:00.0
12:53:00.0
54:00.0
34.0
5:32:30.0
26.0
22.0
31
32:00.0
13:33:00.0
34:00.0
5:35:20.0
16.0
12.0
32
29:00.0
-5:28:00.0
27:00.0
58.0
54.0
5:35:50.0
46.0
33
28:00.0
-6:27:00.0
26:00.0
28.0
24.0
5:36:20.0
16.0
34
44:00.0
-6:43:00.0
42:00.0
28.0
24.0
5:36:20.0
35
32:00:00.0
01:00.0
02:00.0
5:38:00.0
56.0
52.0
37:48.0

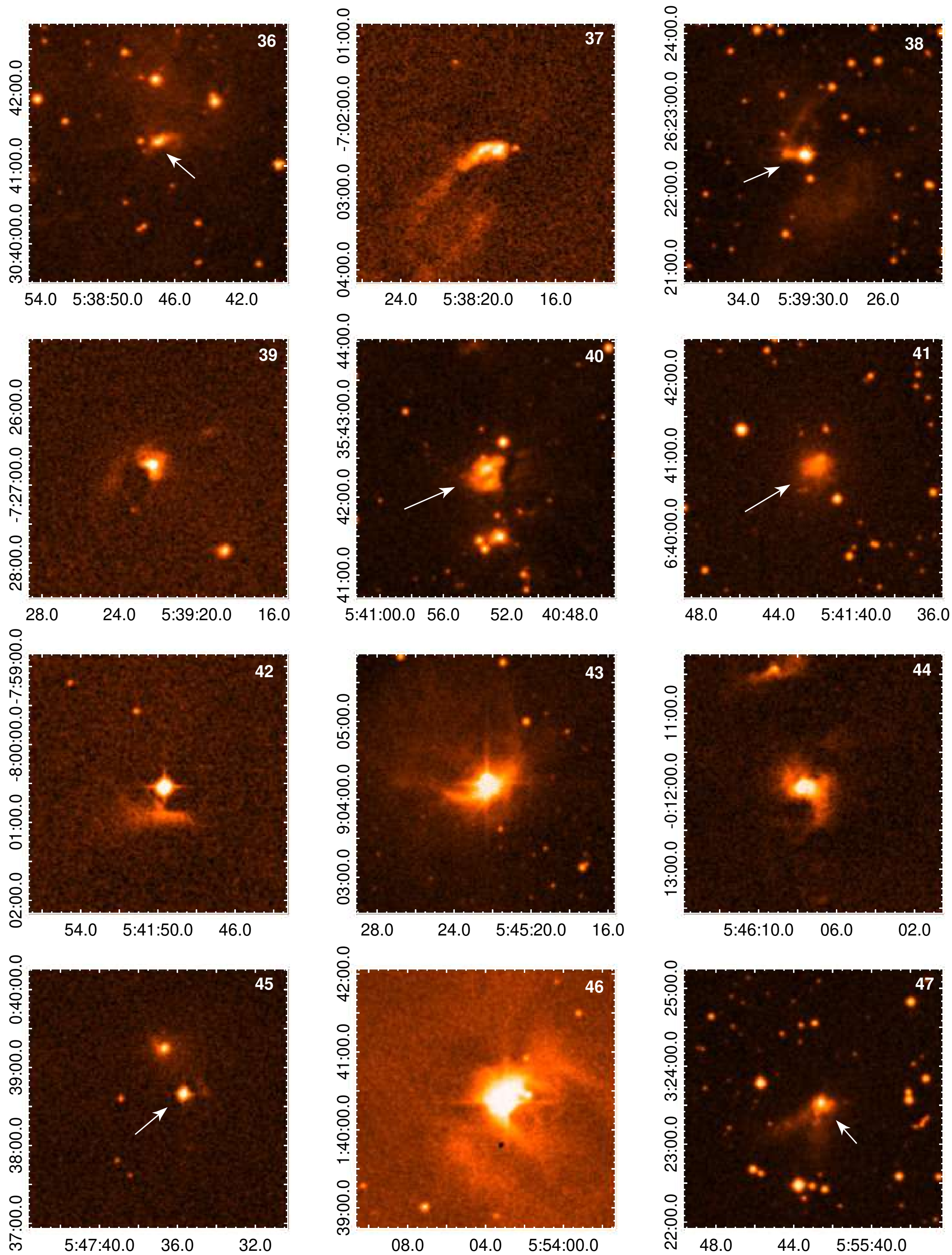
36
54.0 5:38:50.0 46.0 42.0
30:40:00.0 41:00.0 42:00.0
37
24.0 5:38:20.0 16.0
04:00.0 03:00.0 -7:02:00.0 01:00.0
38
34.0 5:39:30.0 26.0
21:00.0 22:00.0 26:23:00.0 24:00.0
39
28.0 24.0 5:39:20.0 16.0
28:00.0 -7:27:00.0 26:00.0
40
5:41:00.0 56.0 52.0 40:48.0
41:00.0 42:00.0 35:43:00.0 44:00.0
41
48.0 44.0 5:41:40.0 36.0
6:40:00.0 41:00.0 42:00.0
42
54.0 5:41:50.0 46.0
02:00.0 01:00.0 -8:00:00.0-7:59:00.0
43
28.0 24.0 5:45:20.0 16.0
03:00.0 9:04:00.0 05:00.0
44
5:46:10.0 06.0 02.0
13:00.0 -0:12:00.0 11:00.0
45
5:47:40.0 36.0 32.0
37:00.0 38:00.0 39:00.0 0:40:00.0
46
08.0 04.0 5:54:00.0
39:00.0 1:40:00.0 41:00.0 42:00.0
47
48.0 44.0 5:55:40.0
22:00.0 23:00.0 3:24:00.0 25:00.0

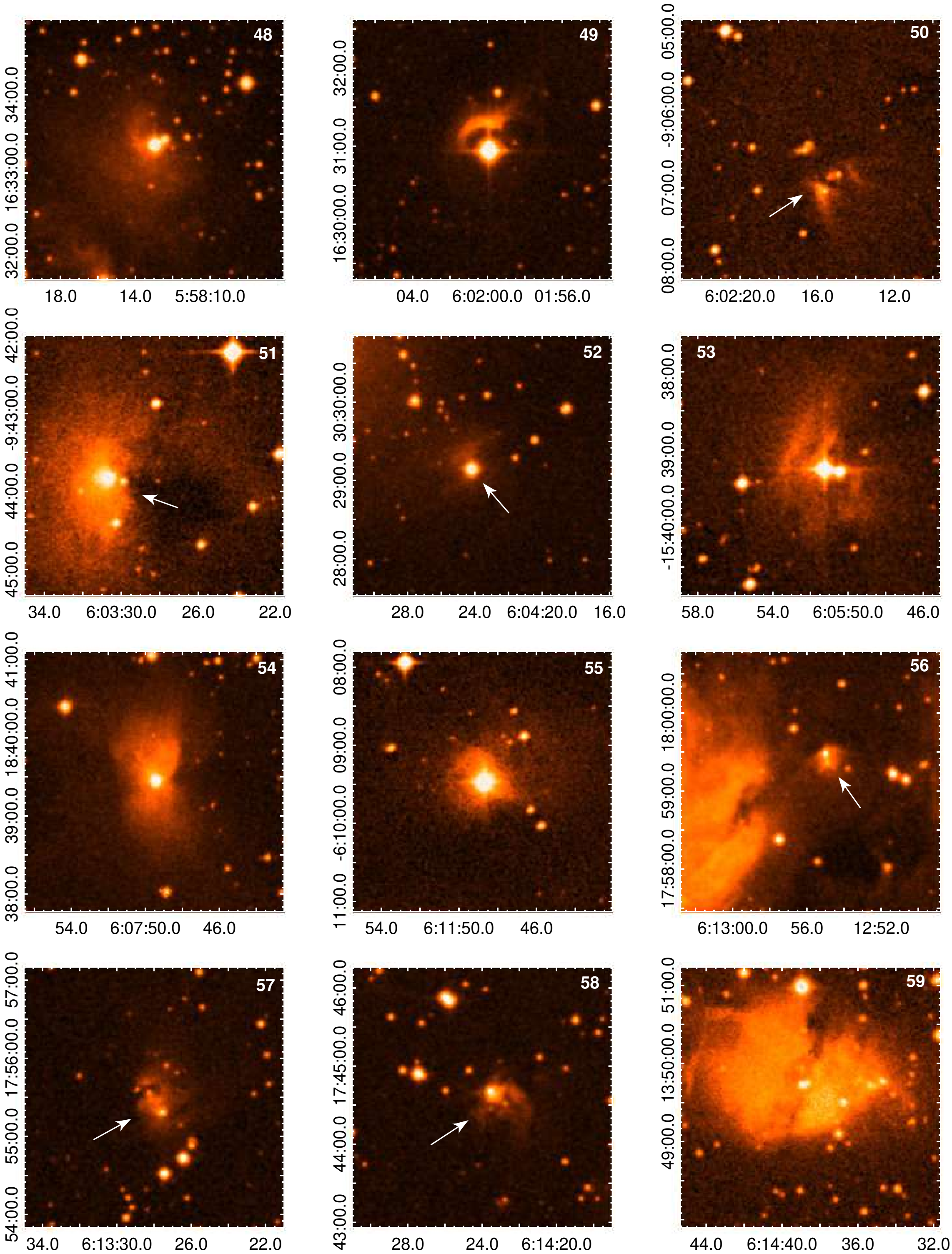
48
32:00.0 16:33:00.0 34:00.0
18.0 14.0 5:58:10.0
49
16:30:00.0 31:00.0 32:00.0
04.0 6:02:00.0 01:56.0
50
08:00.0 07:00.0 -9:06:00.0 05:00.0
6:02:20.0 16.0 12.0
51
45:00.0 44:00.0 -9:43:00.0 42:00.0
34.0 6:03:30.0 26.0 22.0
52
28:00.0 29:00.0 30:30:00.0
28.0 24.0 6:04:20.0 16.0
53
-15:40:00.0 39:00.0 38:00.0
58.0 54.0 6:05:50.0 46.0
54
38:00.0 39:00.0 18:40:00.0 41:00.0
54.0 6:07:50.0 46.0
55
11:00.0 -6:10:00.0 09:00.0 08:00.0
54.0 6:11:50.0 46.0
56
17:58:00.0 59:00.0 18:00:00.0
6:13:00.0 56.0 12:52.0
57
54:00.0 55:00.0 17:56:00.0 57:00.0
34.0 6:13:30.0 26.0 22.0
58
43:00.0 44:00.0 17:45:00.0 46:00.0
28.0 24.0 6:14:20.0
59
49:00.0 13:50:00.0 51:00.0
44.0 6:14:40.0 36.0 32.0

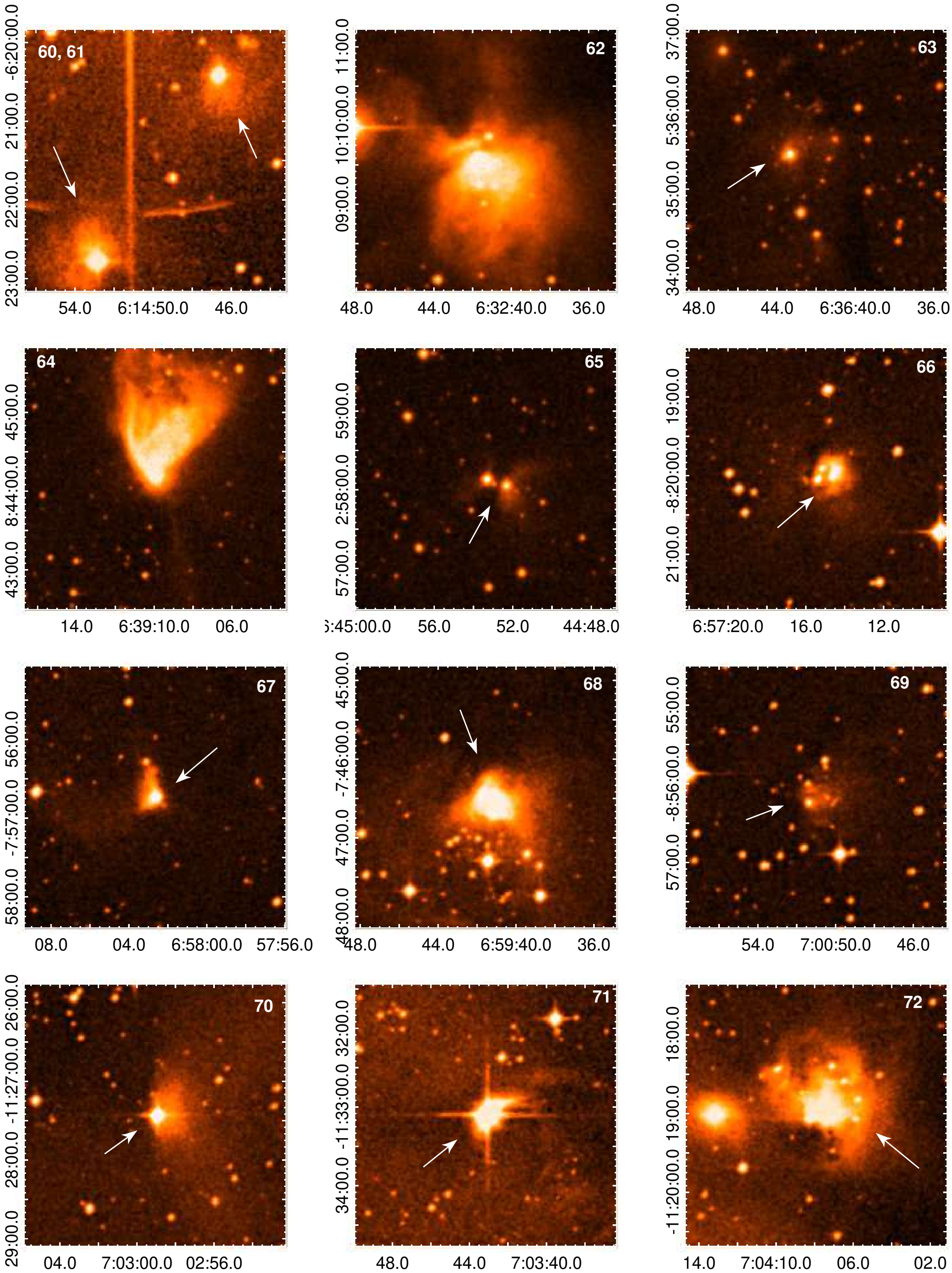
60, 61
-6:20:00.0
21:00.0
22:00.0
23:00.0
54.0
6:14:50.0
46.0
62
11:00.0
10:10:00.0
09:00.0
48.0
44.0
6:32:40.0
36.0
63
37:00.0
5:36:00.0
35:00.0
34:00.0
48.0
44.0
6:36:40.0
36.0
64
45:00.0
8:44:00.0
43:00.0
14.0
6:39:10.0
06.0
65
59:00.0
2:58:00.0
57:00.0
56.0
52.0
44:48.0
66
19:00.0
-8:20:00.0
21:00.0
6:57:20.0
16.0
12.0
67
56:00.0
-7:57:00.0
58:00.0
08.0
04.0
6:58:00.0
57:56.0
68
45:00.0
-7:46:00.0
47:00.0
48:00.0
48.0
44.0
6:59:40.0
36.0
69
55:00.0
-8:56:00.0
57:00.0
54.0
7:00:50.0
46.0
70
26:00.0
-11:27:00.0
28:00.0
29:00.0
04.0
7:03:00.0
02:56.0
71
32:00.0
-11:33:00.0
34:00.0
48.0
44.0
7:03:40.0
72
18:00.0
19:00.0
-11:20:00.0
14.0
7:04:10.0
06.0
02.0

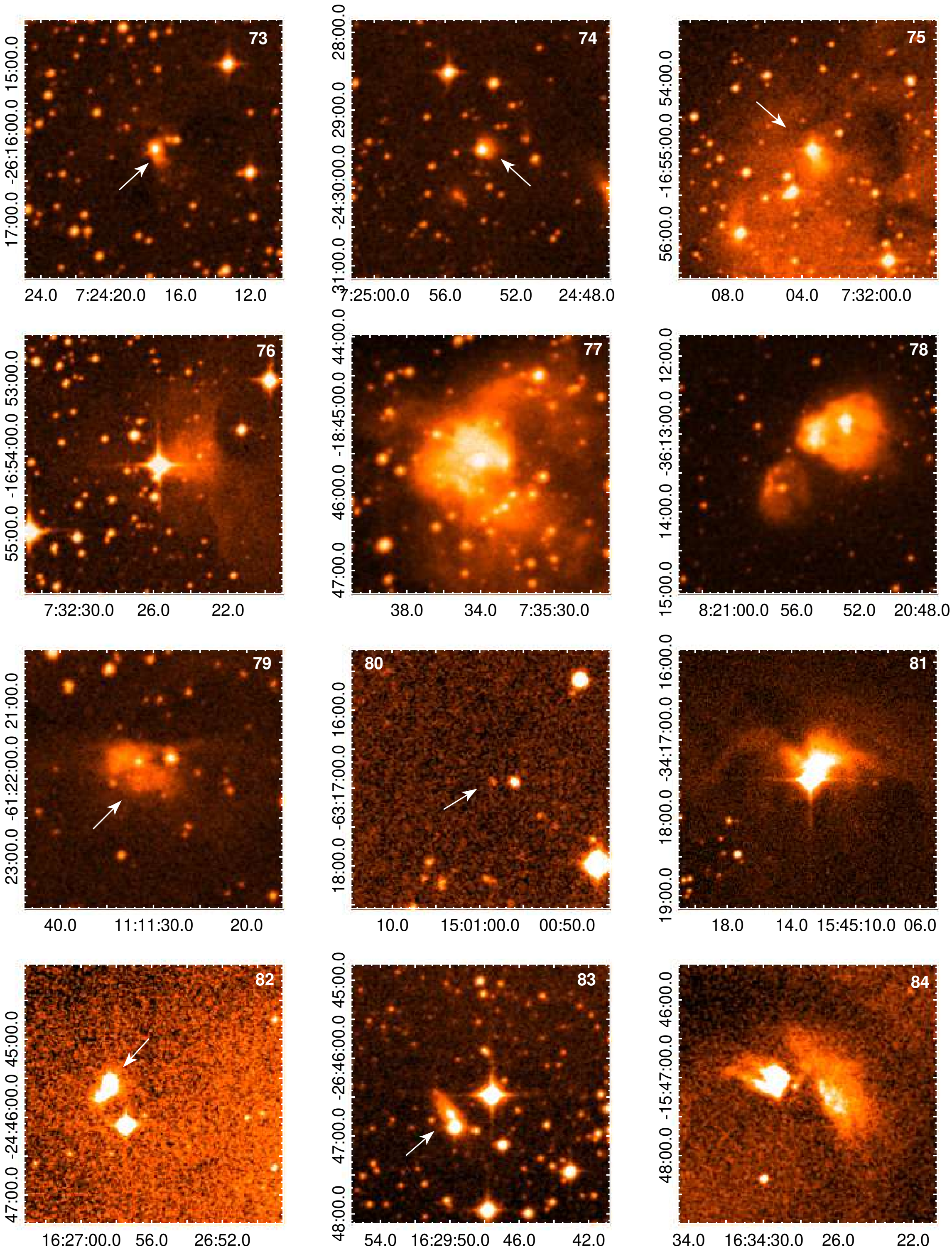
73
17:00.0 -26:16:00.0 15:00.0
24.0 7:24:20.0 16.0 12.0
74
31:00.0 -24:30:00.0 29:00.0 28:00.0
7:25:00.0 56.0 52.0 24:48.0
75
56:00.0 -16:55:00.0 54:00.0
08.0 04.0 7:32:00.0
76
55:00.0 -16:54:00.0 53:00.0
7:32:30.0 26.0 22.0
77
47:00.0 46:00.0 -18:45:00.0 44:00.0
38.0 34.0 7:35:30.0
78
15:00.0 14:00.0 -36:13:00.0 12:00.0
8:21:00.0 56.0 52.0 20:48.0
79
23:00.0 -61:22:00.0 21:00.0
40.0 11:11:30.0 20.0
80
18:00.0 -63:17:00.0 16:00.0
10.0 15:01:00.0 00:50.0
81
19:00.0 18:00.0 -34:17:00.0 16:00.0
18.0 14.0 15:45:10.0 06.0
82
47:00.0 -24:46:00.0 45:00.0
16:27:00.0 56.0 26:52.0
83
48:00.0 47:00.0 -26:46:00.0 45:00.0
54.0 16:29:50.0 46.0 42.0
84
48:00.0 -15:47:00.0 46:00.0
34.0 16:34:30.0 26.0 22.0

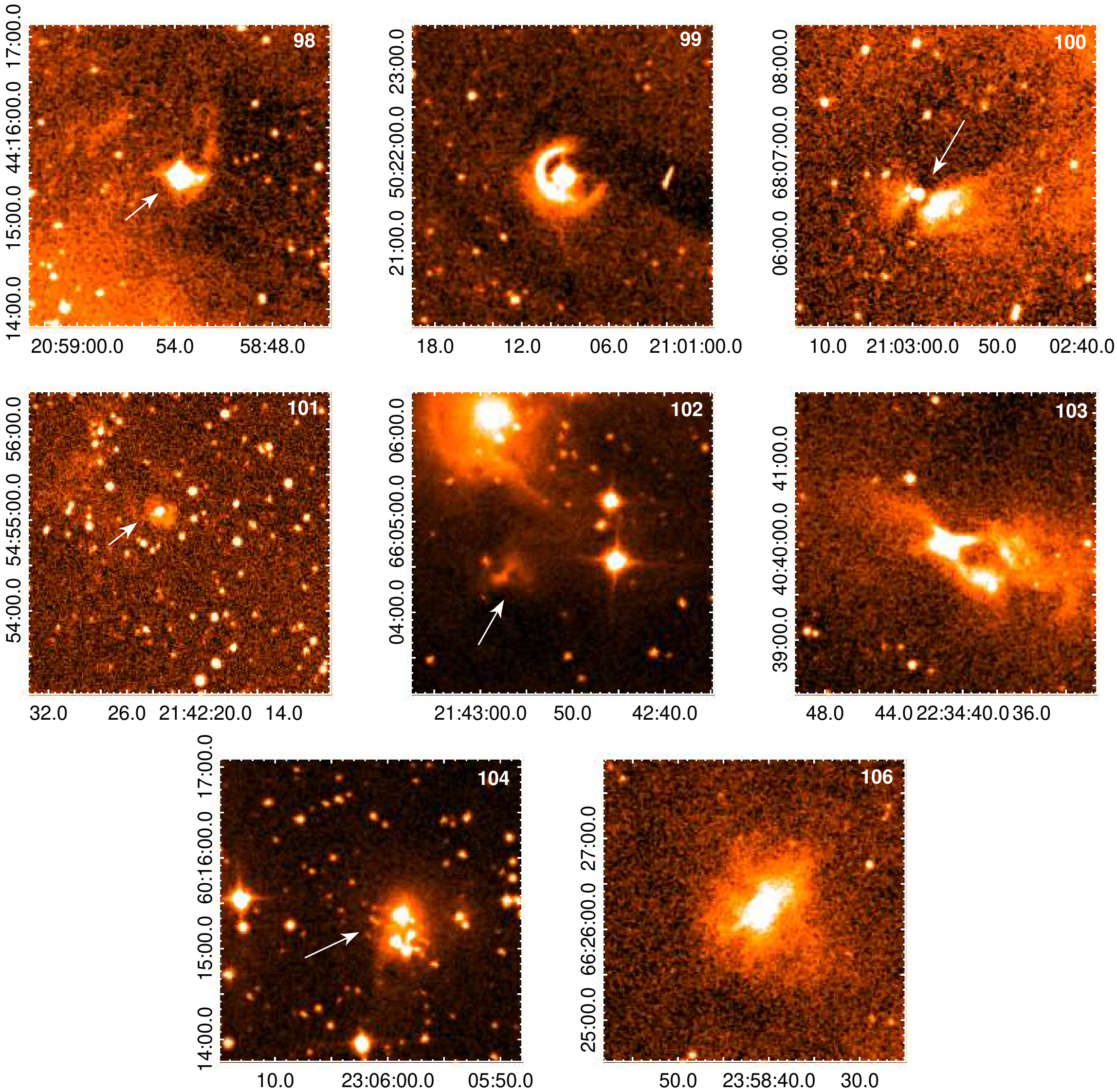
98
20:59:00.0 54.0 58:48.0
14:00.0 15:00.0 44:16:00.0 17:00.0
99
18.0 12.0 06.0 21:01:00.0
21:00.0 50:22:00.0 23:00.0
100
10.0 21:03:00.0 50.0 02:40.0
06:00.0 68:07:00.0 08:00.0
101
32.0 26.0 21:42:20.0 14.0
54:00.0 54:55:00.0 56:00.0
102
21:43:00.0 50.0 42:40.0
04:00.0 66:05:00.0 06:00.0
103
48.0 44.0 22:34:40.0 36.0
39:00.0 40:40:00.0 41:00.0
104
10.0 23:06:00.0 05:50.0
14:00.0 15:00.0 60:16:00.0 17:00.0
106
50.0 23:58:40.0 30.0
25:00.0 66:26:00.0 27:00.0

Appendix C Comments to the nebulae

PP 3 – According to Herbig (1960a), the nebula is variable.
PP 5 – Inclusion in a diffuse nebula, stronger in red rays. The picture is given from the blue Palomar maps.
PP 7 – The star is located in the dark channel of the HII region of IC 1848. No emission lines were detected in the spectrum of the star. The picture is given from the blue Palomar maps.
PP 14 – Variable nebula, which was listed to the cometary class by Ambartsumian (1954). According to Struve & Swings (1948), the Hubble ratio in it is violated by more than 7 magnitudes.
PP 15 – The core of the nebula is an asymmetrical starlike object, brighter in blue rays.
PP 17 – Variable nebula associated with a T Tau star. Of particular interest is the oval-shaped nebula surrounding the T Tau star, which has an emission spectrum characteristic for the Hebig-Haro objects.
PP 31 – Following studies have shown that this object is a galaxy.
PP 37 – The star at the top of the nebula is almost invisible in the blue rays and visible in the infrared. According to Haro (1953), the tail of the nebula has an emission spectrum.
PP 38 – Variable nebula associated with the star RR Tau.
PP 54 – The Hubble biconical nebula Anon $6^h\,04^m$ is associated with the star $L_k\,H_\alpha$ 208, which is variable with the amplitude of 0^m,2 in the rays B and has a variable polarization (Garrison & Anderson, 1978).
PP 56 – Nebula P 9 is rediscovered in Gyul'Budagyan & Magakyan (1977a) at number 19.
PP 59 – Nebula has a strong continuous spectrum. In the spectrum of the nebula, the lines of H, Fe, Ti, Ca, as well as the line 3727 [OII] are observed the emission (Mendez & Parsamyan, 1974). P 10 is the only cometary nebula from which radio emission was detected.
PP 64 – The prototype of cometary nebulae.
PP 65 – The nebula P15 is a peculiar object containing two stars of different brightness in the focus of two hyperbolic arcs.
PP 66 – The nebulae P16, P17 and P18 form a cluster of cometary nebulae. They can be connected by one absorbing cloud (Zellner, 1970).
PP 67 – The spectrum of the P17 nebula is continuous, with a maximum intensity at the with no trace of any lines. The Hubble ratio is violated by 3 magnitudes if the illuminating star is a starlike object at the apex (Mendez & Parsamyan, 1974).
PP 68 – The spectrum of the nebula P18 is continuous, without lines. It has two small condensations of variable brightness, the brighter of which is located near the apex (Mendez & Parsamyan, 1974). This condensation in the range between 11.3 μm and 18 μm is the brightest of the objects observed so far and has $CI_{int} = 4^m.6$. It is possible that the nebula represents the shell of a small cluster of faint red stars (Cohen, 1974).
PP 78 – A variable nebula, in the spectrum of which emission lines of hydrogen, N1, N2, 3727 [OII] were observed (Mendez & Parsamyan, 1974). South of the nebula there are two starlike condensations that are very bright in the red and infrared rays.
PP 88 – The starlike core is variable (Parsamian, 1965). In the spectrum of the nucleus obtained at the 6 m telescope of the Special Astrophysical Observatory of the USSR Academy of Sciences, the emission line has an absorption component from the ultraviolet side.
PP 91 – $L_k H_\alpha$ 225 is a variable star. On the plates obtained by the 2.6 m telescope of the Byurakan Observatory, towards the north of the star, a nebula is seen with a condensation in the upper part. It is much brighter in the red rays. From comparisons with the Palomar maps, it turned out that in 1954 there were no nebulae near the star. This means that by then either it has weakened, or has not yet appeared. In the picture given by Herbig (1960a) in 1956, the asymmetry is felt from the northern side, but the author himself writes nothing about it.
PP 92 – A variable nebula near the fuor V 1515 Cyg.
PP 94 – Following studies have shown that this object is a planetary nebula. 97 – A variable nebula, which is located about 1.5' west of the NGC 7023. The star of the nebula is almost exactly at its top and is visible only in the red rays, but the fan has an approximately neutral color.
PP 98 – The nebula appeared after the formation of the fuor V 1057 Cyg.
PP 106 – In the paper by Parsamian (1965) there was an imprint of coordinates.

Integrable systems connected with black holes

H. Demirchian*

Ambartsumian Byurakan Astrophysical Observatory, Byurakan, 0213, Armenia

Abstract

We studied some important questions in general relativity and mathematical physics mainly related to the two most important solutions of the theory of relativity - gravitational waves and black holes. In particular, the work is related to astrophysical shock waves, gravitational waves, black holes, integrable systems associated with them as well as their quantum equivalents. We studied the effects of null shells on geodesic congruences and suggested a general covariant definition of the gravitational memory effect. Thus, we studied observable effects that astrophysical shock waves can have on test particles after cataclysmic astrophysical events. We studied the geodesics of massive particles in Near Horizon Extremal Myers-Perry (NHEMP) black hole geometries. This is the space-time in the vicinity of the horizon of higher dimensional rotating black holes. Thus, this work can have applications for studying accretions of black holes. The system is also important in mathematical physics as it describes integrable (in special cases superintegrable) system, where the constants of motion are fully studied. On the other hand, the quantum counterparts of this and other integrable systems are studied as well and a new technique is suggested for geometrization of these systems.

Keywords: *shock wave, impulsive signal, gravitational memory effect, black hole, integrable system, Klein-Gordon equation, geometrization*

1. Introduction

This work is devoted to the study of some important questions in general relativity. They include topics related to astrophysical shock waves, impulsive signals, gravitational memory effect, black hole geometries and integrable systems connected with them.

We begin by studying the effects that an impulsive signal in a singular hypersurface can have on a particle which encounters it. We propose a new approach for studying the effect of null shells on null geodesic congruences. This is an exact method which allows one to easily calculate the change in the expansion, shear and rotation of the congruence upon crossing the shell and its evolution to the future of the shell. We find that the effect of the shell on the congruence is a discontinuity in the B-tensor (the gradient of the geodesic vector). We call this the B-memory effect, which is a more covariant way of describing the gravitational memory effect.

Furthermore, we study Hamilton-Jacobi system of a particle in Near Horizon geometry of Extremal Myers-Perry (NHEMP) black hole. The question of integrability of special cases of fully non-isotropic and fully isotropic cases is addressed in this description. The general case, when groups of equal and non-equal rotation parameters exist, is studied. It is shown that this problem reduces to its special cases of fully non-isotropic and fully isotropic NHEMP conformal mechanics. At the end we turn to the integrability problem of the Hamilton-Jacobi system in so-called Near Horizon Extremal Vanishing Horizon Myers-Perry black hole (NHEVHMP).

We have also studied quantum aspects of the superintegrable systems encountered in black hole backgrounds. We propose a geometrization procedure which associates to a non-relativistic quantum particle in a potential on a curved spacetime a purely geodesic motion in another geometry. In other words, we propose a correspondence between the solutions of Schroedinger equation and Klein-Gordon equation. We explain this procedure on the example of the Higgs oscillator and superintegrable Rosochatius system.

*demhov@bao.sci.am

DOI: 10.52526/25792776-2019.66.1-89

2. Geodesic congruences, impulsive gravitational waves and gravitational memory

The study of impulsive gravitational waves in the form of null shells has recently received renewed attention due to their possible role in the transfer of information from black hole horizons to null infinity. As the black hole horizon is a killing horizon, there is an infinite variety of ways to attach (solder) the black hole interior to the black hole exterior creating a null shell on the horizon (Barrabes and Israel, 1991, Blau and O'Loughlin, 2016). A subclass of these can be shown to correspond to BMS like supertranslations. Furthermore the long studied BMS supertranslations at null infinity of asymptotically flat spaces are linked to the physics of soft gravitons which appear to play an important role in restoring information not seen in the hard gravitons of Hawking radiation (Hawking et al., 2017, 2016). In turn the soft gravitons are related to the gravitational memory effect (Strominger and Zhiboedov, 2016).

Gravitational memory (Zel'dovich and Polnarev, 1974, Strominger, 2017, Ashtekar et al., 2018) is the classical change in nearby geodesics in an asymptotically flat region of space-time as they pass through an outgoing gravitational wave. The study of the effect of a null shell on a time-like congruence that crosses it has been addressed by Barrabes and Hogan (Barrabès and Hogan, 2003, Barrabes and Hogan, 2001). They calculated the change in the tangent vector and the geodesic deviation vector together with the expansion, shear and rotation upon crossing an impulsive gravitational wave and found a jump in the acceleration of the geodesic and derivatives of the geodesic deviation vector proportional to the stress-energy content and gravitational wave components of the shell.

To further understand the relationship between gravitons and gravitational memory it is thus important to study the effect of waves on null geodesic congruences, not only as the congruence crosses the wave but also the future evolution of the congruence.

We have presented (O'Loughlin and Demirchian, 2019) a new approach for studying congruences that cross a singular hypersurface. Our method is based on the physically justified assumption that the geodesic vector of a test particle is continuous across the hypersurface when using continuous coordinates. To obtain the geodesic flow to the future of the hypersurface one simply needs to do a coordinate transformation on the past coordinates to go to a continuous coordinate system. The resulting transformation on the geodesic congruence in $\mathcal{M}^-$ gives initial conditions on $\mathcal{N}$ to develop the geodesic vector field on $\mathcal{M}^+$ to the future.

We then proved that a parallel congruence upon crossing the shell gives rise to a hypersurface orthogonal congruence to the future of the shell, and in particular that the shell gives rise to a discontinuity in the B-tensor of the congruence. In general the jump in the expansion is determined by the energy density and currents on the shell while the jump in the shear is determined by the gravitational wave component together with the surface currents. Although we derived these results using a particular congruence, it is clear that the results are independent of the choice of congruence in the case of BMS supertranslations for which the surface currents are zero. We also provide a general argument that a hypersurface orthogonal congruence before the shell will give rise to a hypersurface orthogonal congruence to the future.

The change in the B-tensor after the passage of an outgoing gravitational wave leads to a covariant description of the gravitational memory effect - the *B-memory effect*.

3. Integrability of geodesics in near-horizon extremal Myers-Perry black holes

The system is called *integrable* if in a dynamical system with N degrees of freedom ($2N$ dimensional phase space), the number of independent symmetries is equal to N. If the system possesses $N + p$, $1 \leq p \leq N - 1$, independent symmetries (and hence functionally independent constants of motion), it is called *superintegrable*.

The question of integrability of particle dynamics (Hamilton-Jaconi system) on black hole or near horizon geometries have been extensively analyzed in the literature e.g. see (Carter, 1968, Galajinsky, 2013, Bellucci et al., 2012, Saghatelian, 2012, Galajinsky et al., 2013, Frolov et al., 2007). In particular, it has been shown that the problem is (super)integrable for a large class of black holes.

Given an extremal black hole there are general theorems stating that in the near horizon limit we obtain a usually smooth geometry with larger isometry group than the original extremal black hole. It is hence an interesting question to explore if this symmetry enhancement yields further independent constants of motion and how it affects the integrability of particle dynamics. This question, besides the academic interests, is also relevant to some of the observations related to black holes: It is now a well-accepted fact that there are fast rotating black holes in the sky which are well modeled by an extreme Kerr geometry and the matter moving around these black holes in their accretion disks are essentially probing the near horizon geometry.

The isometry group of generic stationary extremal black holes in the near horizon region is shown to have an $SO(2,1) = SL(2,\mathbb{R})$ part. Therefore, particle dynamics on the near horizon extreme geometries possesses dynamical $0+1$ dimensional conformal symmetry, i.e. it defines a "conformal mechanics" (Galajinsky, 2013, Bellucci et al., 2012, Saghatelian, 2012, Galajinsky et al., 2013). This allows to reduce the problem to the study of system depending on latitudinal and azimuthal coordinates and their conjugate momenta with the effective Hamiltonian being Casimir of conformal algebra. Such associated systems have been investigated from various viewpoints and have been named "angular or spherical mechanics".

We analyzed massive and massless geodesics in the Near Horizon Extremal Myers-Perry background (Demirchian et al., 2018a, Demirchyan et al., 2018, Demirchian et al., 2018b, Demirchian, 2017). We started with a system with $2N+1+\sigma$ variables. Fixing the momenta associated with the isometries, we obtained and focused the $N-1+\sigma$ dimensional "angular mechanics" part. In this sector, whenever N number of rotation parameters m_i of the background metric are equal the $U(1)^N$ isometry is enhanced to $U(N)$ and this latter brings about other second rank Killing tensors. All in all, in the fully isotropic case in odd dimensions with $U(\frac{d-1}{2})$ isometry, the $d-2$ dimensional spherical mechanics part is maximally superintegrable, it has $N+(N-2)=2N-2$ extra constants of motion. The fully isotropic case in even dimensions, however, is not maximally superintegrable; it has still $2N-1$ extra Killing tensors (one less than the N constants of motion to make the system fully superintegrable).

We also discussed the Extremal Vanishing Horizon (EVH) case, which derives from odd dimensional extremal MP when one of the rotation parameters a_i vanishes. In the general NHEVHMP case, where the background isometry is $SO(2,2)\times U(1)^{\frac{d-3}{2}}$ the number of independent charges associated with Killing vectors is $\frac{d+1}{2}$. Despite enhancement of the isometry group compared to the generic NHEMP case, we found that this symmetry enhancement does not add independent constants of motion, the system in general does not poses extra constants of motion and remains just integrable.

4. Superintegrable quantum systems and resonant spacetimes

Geometrization of dynamics is a recurrent theme in theoretical physics. While it has underlied such fundamental developments as the creation of General Relativity and search for unified theories of interactions, it also has a more modest (but often fruitful) aspect of reformulating conventional, well-established theories in more geometrical terms, in hope of elucidating their structure. One particular approach of the latter type is the Jacobi metric. This energy-dependent metric simply encodes as its geodesics the classical orbits of a nonrelativistic mechanical particle on a manifold moving in a potential.

We have presented (Evnin et al., 2018) a procedure associating to quantum systems a Klein-Gordon equation on a static spacetime. For systems with the quadratic energy spectrum, our procedure results in spacetimes with a resonant spectrum of evenly spaced frequencies. This correspondence generalizes the previously known relation between the Higgs oscillator and (global) Anti-de Sitter spacetime.

Implementing our procedure in practice requires solving a nonlinear elliptic equation. The latter form is closely reminiscent of elliptic equations extensively studied in relation to classic 'prescribed scalar curvature' problems of differential geometry (though the exact power appearing in the power-law nonlinearity is different). If one aims at constructing a massless Klein-Gordon (i.e., wave) equation corresponding to the original quantum-mechanical system, the nonlinearity drops out, resulting in a much simpler problem. In this case, known ground state wavefunctions for the original quantum system can be utilized for the conversion procedure. We have demonstrated how this approach works for superintegrable Rosochatius systems, resulting in a family of spacetimes resonant with respect to the massless wave equation.

5. Summary

Here we outline of the main results of this thesis.

- A new approach has been suggested for studying the effects of impulsive gravitational waves on congruences encountering them. The technique has been applied on null congruences. It has been established that hypersurface orthogonal null congruences stay such after crossing the shell.
- A covariant definition of the gravitational memory effect has been suggested based on the B-tensor of the congruence. The relations between the components of the B-tensor and the stress-energy tensor of the shell have been derived. The B-tensor has been calculated and the approach has been demonstrated for BMS type soldering.
- A common description has been introduced for even and odd dimensional NHEMP geometries. This description was used to prove that the even dimensional fully non-isotropic NHEMP system is integrable.
- Integrals of motion, as well as the Killing vectors of the fully non-isotropic NHEMP in arbitrary dimensions have been presented in initial coordinates. We found a non-trivial transformation between the integrals of motion of fully non-isotropic and fully isotropic NHEMP black hole geometries.
- We separated the variables of the most general partially isotropic NHEMP and showed its transformation to the special cases of fully non-isotropic and isotropic NHEMP.
- A new approach has been suggested for mapping Schrödinger equation on a curved background to a Klein-Gordon equation on the background of another geometry. We have shown that this procedure greatly simplifies for systems with quadratic spectra and applied it on the Higgs oscillator and the superintegrable Rosochatius system.

References

C. Barrabes and W. Israel. Thin shells in general relativity and cosmology: The Lightlike limit. *Phys. Rev.*, D43:1129–1142, 1991. doi: 10.1103/PhysRevD.43.1129.

Matthias Blau and Martin O'Loughlin. Horizon Shells and BMS-like Soldering Transformations. *JHEP*, 03:029, 2016. doi: 10.1007/JHEP03(2016)029.

Stephen W. Hawking, Malcolm J. Perry, and Andrew Strominger. Superrotation Charge and Supertranslation Hair on Black Holes. *JHEP*, 05:161, 2017. doi: 10.1007/JHEP05(2017)161.

Stephen W. Hawking, Malcolm J. Perry, and Andrew Strominger. Soft Hair on Black Holes. *Phys. Rev. Lett.*, 116(23):231301, 2016. doi: 10.1103/PhysRevLett.116.231301.

Andrew Strominger and Alexander Zhiboedov. Gravitational Memory, BMS Supertranslations and Soft Theorems. *JHEP*, 01:086, 2016. doi: 10.1007/JHEP01(2016)086.

Y. B. Zel'dovich and A. G. Polnarev. Radiation of gravitational waves by a cluster of superdense stars. *Soviet Astronomy*, 18:17, August 1974.

Andrew Strominger. Lectures on the Infrared Structure of Gravity and Gauge Theory. 2017.

Abhay Ashtekar, Miguel Campiglia, and Alok Laddha. Null infinity, the BMS group and infrared issues. *Gen. Rel. Grav.*, 50(11):140–163, 2018. doi: 10.1007/s10714-018-2464-3.

C. Barrabès and P. A. Hogan. *Singular Null Hypersurfaces in General Relativity: Light-Like Signals from Violent Astrophysical Events.* World Scientific Publishing Co, 2003. doi: 10.1142/5454.

C. Barrabes and P. A. Hogan. Detection of impulsive light - like signals in general relativity. *Int. J. Mod. Phys.*, D10:711–722, 2001. doi: 10.1142/S0218271801001098.

Martin O'Loughlin and Hovhannes Demirchian. Geodesic congruences, impulsive gravitational waves and gravitational memory. *Phys. Rev.*, D99(2):024031, 2019. doi: 10.1103/PhysRevD.99.024031.

B. Carter. Hamilton-Jacobi and Schrodinger separable solutions of Einstein's equations. *Commun. Math. Phys.*, 10(4):280–310, 1968. doi: 10.1007/BF03399503.

Anton Galajinsky. Near horizon black holes in diverse dimensions and integrable models. *Phys. Rev.*, D87(2):024023, 2013. doi: 10.1103/PhysRevD.87.024023.

Stefano Bellucci, Armen Nersessian, and Vahagn Yeghikyan. Action-Angle Variables for the Particle Near Extreme Kerr Throat. *Mod. Phys. Lett.*, A27:1250191, 2012. doi: 10.1142/S021773231250191X.

Armen Saghatelian. Near-horizon dynamics of particle in extreme Reissner-Nordstróm and Clement-Gal'tsov black hole backgrounds: action-angle variables. *Class. Quant. Grav.*, 29:245018, 2012. doi: 10.1088/0264-9381/29/24/245018.

Anton Galajinsky, Armen Nersessian, and Armen Saghatelian. Superintegrable models related to near horizon extremal Myers-Perry black hole in arbitrary dimension. *JHEP*, 06:002, 2013. doi: 10.1007/JHEP06(2013)002.

Valeri P. Frolov, Pavel Krtous, and David Kubiznak. Separability of Hamilton-Jacobi and Klein-Gordon Equations in General Kerr-NUT-AdS Spacetimes. *JHEP*, 02:005, 2007. doi: 10.1088/1126-6708/2007/02/005.

Hovhannes Demirchian, Armen Nersessian, Saeedeh Sadeghian, and M. M. Sheikh-Jabbari. Integrability of geodesics in near-horizon extremal geometries: Case of Myers-Perry black holes in arbitrary dimensions. *Phys. Rev.*, D97(10):104004, 2018a. doi: 10.1103/PhysRevD.97.104004.

H. Demirchyan, A. Nersessian, S. Sadeghian, and M. M. Sheikh-Jabbari. Integrability of Geodesics in Near-Horizon Extremal Vanishing Horizon Myers–Perry Black Holes. *Phys. Atom. Nucl.*, 81(6): 907–911, 2018. doi: 10.1134/S106377881806011X.

H. Demirchian, T. Hakobyan, A. Nersessian, and M. M. Sheikh-Jabbari. Myers–Perry Conformal Mechanics. *Phys. Part. Nucl.*, 49(5):860–864, 2018b. doi: 10.1134/S1063779618050167.

Hovhannes Demirchian. Note on constants of motion in conformal mechanics associated with near horizon extremal Myers–Perry black holes. *Mod. Phys. Lett.*, A32(27):1750144, 2017. doi: 10.1142/S0217732317501449.

Oleg Evnin, Hovhannes Demirchian, and Armen Nersessian. Mapping superintegrable quantum mechanics to resonant spacetimes. *Phys. Rev.*, D97(2):025014, 2018. doi: 10.1103/PhysRevD.97.025014.

Communications of BAO, Vol. 66, Issue 1, 2019, pp. 94-110

The Origin of Non-Thermal Emission from FSRQs

S. Gasparyan

ICRANet-Armenia, Marshall Baghramian Avenue 24a, Yerevan 0019, Republic of Armenia

Abstract

The observations of astrophysical sources in a large frequency range (from radio to very high energy gamma-ray bands) provide complete information on the non-thermal processes taking place in different objects. Here, the origin of broadband emission from the jets of flat-spectrum radio quasars are discussed. For the current study the blazars detected above 100 GeV: PKS 1441+25, 3C 279, PKS 1222+216, PKS 1510-089, as well as CTA 102, which was in flaring state in optcal/UV, X-ray and high energy gamma-ray bands, are selected. The publicly available data of Fermi LAT, Swift UVOT/XRT, Nustar telescopes have been analyzed, which enables to identify the prominent flaring and quiescent states for those sources, as well as, study the spectral properties, constrain the size and location of the emitting region.

The multiwavelength emission spectra of those sources, in different states, are modelled, which is crucial for understanding the particle acceleration and emission processes in their jets. For this purpose, a new code that can derive the model free parameters which statistically better describe the observed data is used. It derives the best-fit parameters and their uncertainties through Markov Chain Monte Carlo sampling of the likelihood distributions. By means of the detailed theoretical modeling of acquired data, it was possible to derive or at least constrain some crucial parameters such as the magnetic field, jet energetics, electron energy density etc.

Keywords: *FSRQs, relativistic jets, gamma-rays, non-thermal emission, theoretical modeling*

1. Introduction

Understanding the formation, structure and evolution of our Universe is one of the greatest mysteries. The emission processes taking place in Galactic sources (e.g. pulsars, supernova remnants, binary systems etc.) are relatively well examined and are always among the most discussed topics in astrophysics, however, the recent major progress in the telescope technique makes it possible to investigate the physical processes in extragalactic objects as well. Among extragalactic sources, the most powerful γ-ray emitters are blazars, which are classified as a subclass of AGNs, whose jet makes small angle in respect to the observer (Urry and Padovani, 1995). Blazars are very strong non-thermal emitters in all observable energy bands, ranging from radio to γ-ray bands.

The extremly short and strong variability, as well as, strong polarization detected from those sources witness the extreme environments and undergoing processes in the jets of blazars, making the study of these objects one of the most important topics of modern astrophysics.

By observational properties, blazars are divided into BL-Lacertae (BL-Lac) and flat spectrum radio quasars (FSRQs). The latter, are low-peaked ($\nu_{peak} < 10^{14}$ Hz) blazars, and in average have decaying spectra in the MeV/GeV bands, which makes these objects less possible to detect in Very High Energy bands (VHE; $>$ 100 GeV). Up to now, only seven of FSRQs have been detected in VHE γ-ray band, which makes these objects more interesting to investigate.

Now, with the available data, the evolution of the broadband emission from blazars can be followed in physically reasonable timescales. In the theoretical modeling of blazar emission two most actual problems are 1) identifying processes responsible for the time averaged emission from radio to HE/VHE γ-ray bands and 2) finding a model which can explain time evolution of SEDs that is physical connection between the emission in different states (flaring and quiescent). These are ambitious and very complicated problems but are the ultimate goals of any currently developing and proposed theories. In principle, these two problems are linked: in order to find a unique dynamical evolving radiative

DOI: 10.52526/25792776-2019.66.1-94

model to explain the overall emission from blazars it is necessary to be able to explain the emission in different states which then can be generalized within one single emission scenario. In other words, in order to understand the global emission processes in the jet, initially the empirical models explaining the SEDs at any given period should be very well investigated. This will also provide most detailed information on the jet parameters and their evolution time which are necessary for developing a self-consistent radiation model.

Up to now various theories and models were proposed to explain the observed multiwavelength emission from blazars. Most of them were successful in explaining the multiwavelength spectra in a given period but usually they fail to model the SED observed in another period. This is normal since these models do not include physical connection between different states of the jet and are meant only to understand the emission observed at a given period. Moreover, sometimes the problems are even more complicated: two different models or the same model with another set of free parameters can equally well explain the observed data which introduces significant difficulties for theoretical modeling.

Since the main aim of the applied theoretical models is to gain as much as possible information from the observed spectra various statistical methods should be applied to compare different models or to find the set of free parameters which statistically better explain the observed data. The latter one is especially important as finding the parameters best explaining the data allows direct insight into the processes ongoing in the jet and constraining the parameters describing the jet. This implies that successful application of any theoretical model should also contain effective optimization of model free parameters. Since the models have nonlinear dependence from the model free parameters the effective optimization of the parameters is not a trivial task. There are various methods which can be used to find best description of the data one of the simplest one being calculation of chi-squares (χ^2) when the data and the models are compared. However, it is well known that the models with many free parameters are best optimized by Markov Chain Monte Carlo (MCMC) method. Due to the recent developments in high performance computing now the MCMC samplers with high number of steps can be used, so most precise results can be obtained.

Last but not least, the observations of blazars (especially in the γ-ray band) can help also to understand the formation of the Universe. The detection of distant γ-ray sources is restricted not only by their low emission flux (below telescopes sensitivities), but also the produced photons can be absorbed. They can interact with the photons of diffuse radiation in the Universe, so called extragalactic background light (EBL) and produce electron-positron pairs. The density of EBL photon field is composed by the light emitted since the formation of the Universe (stars, galaxies etc.) and it contains valuable information on the history of star and galaxy formation. The EBL density cannot be measured directly and it can be done only indirectly, namely when the γ-ray emission from a very distant blazar is observed, it can help to measure the limit of EBL photon density. Especially are important the observations of very distant blazars with Fermi LAT and ground based Cherenkov telescopes (MAGIC, VERITAS, HESS) so combining the data in the MeV/GeV (unabsorbed) and TeV (absorbed) bands can help to constrain the density of EBL. This once more emphasizes the importance of studying blazars in general and the origin of their emission in particular.

2. The study of blazar emission

2.1. Broadband emission from blazars

The electromagnetic emission from blazars is observed in a wide energy range from radio to HE γ-ray bands. This broadband emission is predominantly of a nonthermal origin, although, sometimes, thermal emission from some components can be also observed. The broadband SED of blazars has two nonthermal peaks - one at optical/UV or X-rays (the low-energy component) and the other at higher energies (the γ-ray band). The observed high-degree polarization indicates that the low-energy component is most likely due to the synchrotron emission of electrons accelerated in the jet. While the synchrotron emission can explain the observed features of the low-energy component, the origin of the HE component is still unclear, so various models/scenarios were proposed. One of the most widely applied models is that the HE component is produced via IC scattering of soft photons being either internal (e.g., synchrotron photons; SSC (Ghisellini et al., 1985) (Maraschi et al., 1992)) or external:

EIC (Sikora et al., 1994) (Ghisellini and Tavecchio, 2009) to the jet. The inverse Compton scattering of both internal and external photon fields are discussed in (Gasparyan, 2019). Discussed models are used in this study.
These pure leptonic models have been successful in explaining the SEDs of blazars but sometimes fail to reproduce some observed features. As a distinct alternative, models involving the radiative output of protons accelerated in the jet (hadronic models) were proposed (Mannheim and Biermann, 1992). The protons carry significant amount of energy and the exact estimation of their content in the jet can be crucial for understanding the physics of the jet. Even in the leptonic scenarios, hadrons (protons) are expected to be present in the jet to ensure the charge neutrality of the plasma. Then these protons can be effectively accelerated and by interacting with a dense target (proton-proton interaction), magnetic (proton-synchrotron) and/or photon fields (pγ interaction) produce the observed HE component. In the case of hadronic models, more extreme parameters are required as compared with leptonic models (e.g., in the last two cases the protons should be accelerated beyond 10^{19} and propagate in a magnetic field exceeding 30 G (Mannheim and Biermann, 1992), (Mücke and Protheroe, 2001)) but in principle these conditions can be formed in the jet and sometimes the hadronic models give better modeling of SEDs (Böttcher et al., 2013). Leptonic one-zone emission scenarios are the most common models applied to explain the broadband emission from blazars. The emitting region is assumed to have a spherical geometry (blob) carrying a magnetic field with an intensity of B and a population of relativistic electrons/positrons. Since the emission region moves along the jet with a bulk Lorentz factor of Γ_{bulk}, the observed radiation will be amplified by a relativistic Doppler factor of $\delta = 1/\Gamma_{bulk}(1-\beta\cos(\Theta_{obs}))$, where Θ_{obs} is the jet inclination angle (usually $< 8°$ for blazars). The size of emission region can be constrained by the observed variability time-scale (τ), $R_{\rm b} \leq \delta$ c $\tau/(1+z)$. It has already been noted that blazars are characterized by extreme variability (in both time and amplitude), which implies that the emission region should be very compact. For typical parameters of $t_{\rm var} \sim$ few hours and $\delta \sim 10 \div 20$, the emission region cannot exceed 10^{15}-10^{16} cm. This implies that blazar observations are unique tools for investigation of the sub-parsec structures of their jets. As the one-zone models assume the emission is produced from a single population of electrons, it is expected to have correlated flux changes in various bands (Ulrich et al., 1997). However, for some blazars the expected correlations were not observed, so alternative two-zone models were proposed (Kirk et al., 1998). The basic idea of two-zone models is that the multiwavelength emission is produced from two blobs having different size or location along the jet and each containing different population of particles. For example, one of these models assumes that particles are accelerated in one blob, but they emit whenever they are injected in the second blob. As an alternative, in order to explain the rapid variability in the γ-ray band, a model where the emission is produced in two emitting regions of different sizes and distances from the central source was proposed. Of course, two-zone models contain more free parameters, so are easier for modeling, but these are only possibilities, when complex changes of multiwavelength flux are observed. Now in the era of available large amount of multiwavelength data, not only currently known theories can be tested but also new emission models can be proposed.

2.2. Theoretical modeling of SEDs

The progress of theoretical astrophysics in understanding various processes allowed developing numerical simulation techniques to follow the jet from the beginning up to its termination point. For example, the impact of the jets on the environment where they propagate and their collimation and propagation can be investigated by realistic high-resolution simulations of the jets. By three-dimensional general relativistic magneto-hydrodynamic simulation of jet formation from an accretion disk allows to investigate their launching and acceleration. Of course, the simulations are a powerful tool for investigating different properties of the jet but they require initial parameters which can be obtained only from observations and theoretical modeling of the results. For example, the observations in radio band are unique to probe their morphology and the internal structures of the jet or the monitoring in HE γ-ray bands allows following the evolution of the system in time. On the other hand, the theoretical modeling of the broadband emission spectra will allow to estimate or at least constrain several important parameters, such as emitting particle energy density and distribution, magnetic field, etc., which are necessary to investigate the physics of the jets. Therefore, the high quality of the observed multiwavelength data and their theoretical modeling has become one of the most actively discussed topics in modern astrophysics. As mentioned above, the modeling of multiwavelength spectra of blazars is a powerful method to investigate the physics of blazar jets. However, finding parameters of a model, which statistically best describe the observed data, is perhaps one of the most actual problems in the modeling the multiwavelength SEDs of blazars. There are two main methods of optimizing model free parameters: analytic (e.g. chi-square (χ^2) minimization, maximum log-likelihood estimation, etc.) and numerical (e.g. Newton's, steepest-descent, MCMC methods). Among analytical methods perhaps the simplest method defining the best fit of a function is the chi-square minimization, the idea of which is to minimize the difference between the observed data and prediction curve. Although, there are plethora of optimization techniques, for high-dimensional problems, containing many free parameters, more efficient, i.e. less expensive to compute, are numerical methods, among which one of most popular is MCMC method, which comprises a class of algorithms for sampling from a probability distribution and one can obtain a sample of the desired distribution by observing the chain after a number of steps. Running MCMC samplers allows finding the best-fit and uncertainties of the model free parameters. Due to the recent developments in high performance computing now the MCMC samplers with high number of steps can be used so most precise results can be obtained. In order to optimize the free parameters, when multiwavelength SEDs of blazars are modeled, a python code is developed. It is based on the Naima package (Zabalza, 2015), which is based on the emcee package, enables to constrain a model's free parameters by performing MCMC fitting. The MCMC approach, which is based on the Bayesian statistics, is superior to the grid approach with a more efficient sampling of the parameter space of interest, especially for high dimensions (Wraith et al., 2009). The algorithm behind the code is the affine-invariant ensemble sampling algorithm for MCMC method proposed by Goodman & Weare (Goodman and Weare, 2010), which has several advantages over traditional MCMC sampling methods (e.g. the Metropolis-Hastings algorithm) and excellent performance as measured by the autocorrelation time (Foreman-Mackey et al., 2013). The code derives the best-fit model and uncertainty distributions of spectral model parameters through MCMC sampling of their likelihood distributions. The code is used to study flaring activities in the jets of FSRQs.

3. The origin of flares

In the theoretical interpretation of the multiwavelength emission from blazars, the size/location of the emitting region, magnetic field and electron energy distribution are uncertain. Only during flaring periods some of the unknown parameters can be constrained based on the observations in different bands. The majority of the blazars detected in VHE γ-ray band are high-frequency-peaked BL Lacs for which the synchrotron bump is in the UV/X-ray bands. In addition to the BL Lacs, there are also 7 FSRQs detected in the VHE γ-ray band which is rather surprising, since the BLR structure of these objects, which is rich in optical-UV photons, makes these environments strongly opaque to VHE γ-rays (Liu and Bai, 2006) (Poutanen and Stern, 2010). Moreover, FSRQs have a relatively steep photon index in the energy range of >100 MeV as was observed with the Fermi LAT which does not make them as strong emitters of VHE γ-ray photons. Detection of FSRQs in the VHE γ-ray band is challenging for the near-black-hole dissipation scenarios; it assumes that the γ-rays are most likely produced farther from the central source, outside the BLR, where the dominant photon field is the IR emission from the dusty torus. Typically, the temperature of torus photons $\sim 10^3$ K is lower than that of the photons reflected in the BLR $\sim 10^5$ K, and, in principle, VHE photons with energy up to ~ 1 TeV can escape from the region. Thus, the observations of FSRQs in VHE γ-ray band provide an alternative view of blazar emission as compared to BL Lacs. Moreover, since FSRQs are more luminous than BL Lacs, they could, in principle, be observed at greater distances. Indeed, the farthest sources detected in the VHE γ-ray band are the FSRQs at a redshift of $z \geq 0.9$ (e.g., PKS 1441+25 (Abeysekara et al., 2015), (Ahnen et al., 2015) and S3 0218+35 (Ahnen et al., 2016)). That is why FSRQs are ideal for estimation of the intensity of EBL through the absorption of VHE photons when they interact with the EBL photons (Coppi and Aharonian, 1999), (Madau and Phinney, 1996).

3.1. High energy gamma-ray emission from PKS 1441+25

Among FSRQs, PKS 1441+25 is one of the most distant sources detected so far at $z = 0.939$ (Shaw et al., 2012). In April 2015 both VERITAS and MAGIC collaborations announced the detection of VHE γ-rays from PKS 1441+25 (with up to 250 GeV photons) (Mirzoyan, 2015), (Mukherjee, 2015). During the same period, the source had been also observed with the telescopes Swift and NuSTAR. The observations of PKS 1441+25 during the bright period in April 2015 by different instruments provide us with data on the maximums of the emitting components (Swift UVOT/ASAS-SN and Fermi LAT) as well as on the transition region between these components in the energy range from 0.3 to 30 keV (Swift XRT and NuSTAR) (Abeysekara et al., 2015). In order to scope and investigate the flaring periods, light curves with different equal time binning are generated (see in Fig. 1). Next, for detailed investigation of the flaring periods, the flux changes in time, a light curve has been generated by an adaptive binning method, where the time bin widths are flexible and chosen to produce bins with constant flux uncertainty (Lott et al., 2012). The light curves show a strong emission from the source detected on April 20 to 27, 2015. During the same period, the source had been also observed with the telescopes Swift and NuSTAR. Similar data (up to HE γ-ray band) are available also from the observations carried out on January 06 to 28, 2015, which is the period of the large flare that was observed with Fermi LAT. The source was in active state on 21-27 January, when on 24 January the flux increased up to $(2.22 \pm 0.38) \times 10^{-6}$ photon cm^{-2} s^{-1}. In April, when the source was detected in VHE band, the photon index in MeV/GeV energy range hardened and reached $\leq$1.9 most of the time, with the hardest photon index of $\Gamma = 1.54 \pm 0.16$, which is not typical for FSRQs. Moreover, the

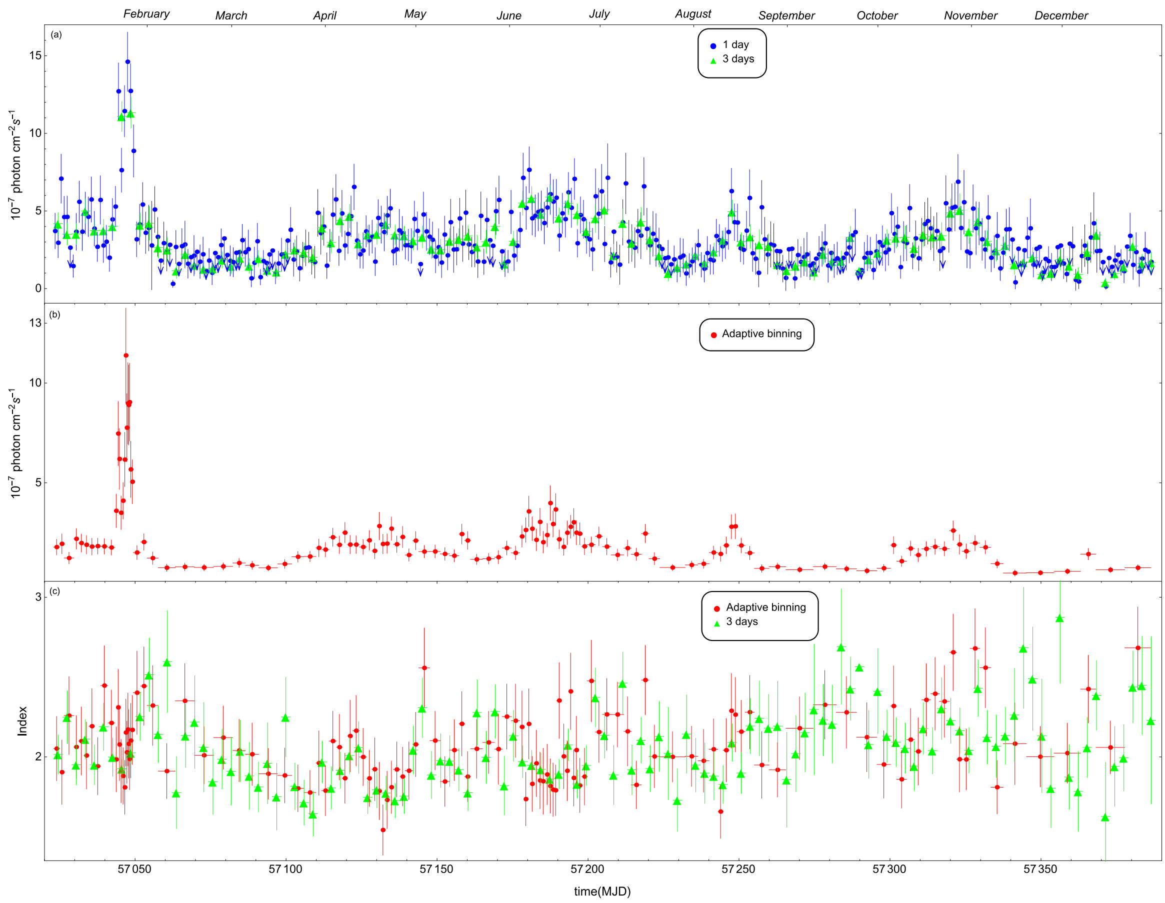

Figure 1. The γ-ray light curve of PKS 1441+25 from January to December 2015 (a). The bin intervals correspond to 1-day (blue data) and 3-days (green data). The light curve obtained by adaptive binning method assuming 20 % of uncertainty is presented in red (b). The change of photon index for 3-day binning (green) and with adaptive binning method are shown in (c).

spectral analyis of Fermi LAT data reveal a deviation of spectrum from the simple power-law shape at $E_{cut} = 17.7 \pm 8.9$ GeV, which most probably is a result of electron cooling (Fig. 2). During the

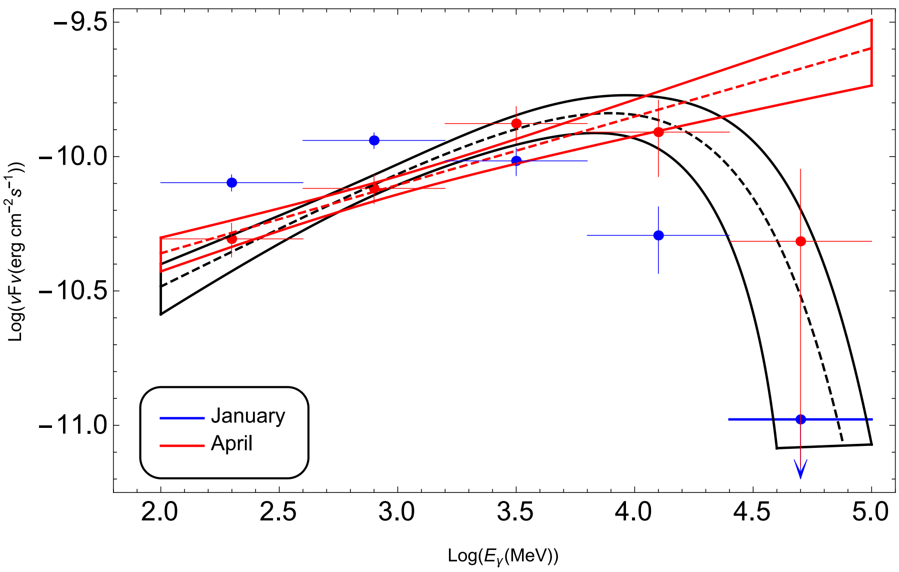

Figure 2. The γ-ray spectrum of PKS 1441+25 above 100 MeV averaged over the *Fermi* LAT observations in January (blue) and April (red).

January flare, the shortest flux variability is measured to be $\tau_d = 1.44$ days (see fig 2 in (Sahakyan and Gasparyan, 2017)), which enables to constrain the emitting region size up to $R_b \leq 3.5 \times 10^{16}(\delta/18)$ cm.

Actually, by modeling the emission in these two periods and estimating the parameter space that describes the underlying particle distribution responsible for the emission through MCMC technique, one can investigate and explore particle acceleration/ emission processes and jet properties in these two significant flaring periods which are crucial for understanding the origin of the flares. The broadband SEDs of PKS 1441+25 for different periods are shown in Fig. 3 where with red and blue colors are the SED observed in January and April respectively, while the archival data from ASI science data center are shown with gray color. We note that during the high states, the second emission peak increased by intensity and shifted to HEs. During the flaring periods the low-energy component's intensity increased as compared with the quiescent state; the increase in April exceeded that one observed in January (although the power-law photon index in the X-ray band ($\approx$2.3) had been relatively constant during both observations). More evident and drastic is the change of the peak intensity of the low energy component; from January to April it increased by nearly an order of magnitude and as compared with the quiescent state it increased $\geq$15 times. On the contrary, the peak of the second component (in the HE γ-ray band) is relatively constant, only the photon index in the MeV-GeV energy range is harder during the observations in April. The Compton dominance of the source is stronger and evident during the flaring periods, which suggests that the density of the external photon fields significantly exceeds the synchrotron photon density ($U_{ext}/U_{syn} \gg 1$). Such a strong amplification of the emission from blazars can be explained by means of introducing changes in the emission region parameters (e.g. in the magnetic field, emitting region size, bulk Lorentz factor and others, and/or particle energy distribution). In principle, all the parameters describing the emitting region can be changed at the same time if the flares are due to a global change in the physical processes in the jet, which also affect the jet dynamics and properties. However, usually, the change in one or two parameters is enough to explain the flares. An interesting study of the flaring activity in FSRQs as a result of changes in different parameters has been investigated in (Paggi et al., 2011). Namely, the emission spectra evolution as a function of changes in different parameters (e.g., bulk Lorentz factor, magnetic field, accretion rate, etc.) is investigated. In the case of PKS 1441+25, during its flaring periods, both the low energy and HE components increased several times. The increase of the second component is most likely due to moving of the emitting region outside its BLR. In principle, there are two possibilities: i) either the emitting region moves faster due to increasing bulk Lorentz factor and leaves the BLR or ii) the bulk Lorentz factor is unchanged and only the emitting region is moving beyond the BLR.

In the first case, since the external photon density in the commoving frame of the jet depends on the Doppler boosting factor, a strong increase in the Compton dominance will be observed. Additional increase of the magnetic field from January to April is also evident when the low energy component kept increasing (this corresponds to the case shown in Fig. 1 (b) in (Paggi et al., 2011)). Accordingly, two possibilities are discussed. First, it is assumed that δ has increased from 10 in the quiescent to 18 in the flaring periods, and alternatively: the Dopller factor was constant ($\delta = 18$) in both periods. These values are below and above the estimated mean bulk Lorentz factor of FSRQs obtained from the analysis of a large sample of γ-ray emitting FSRQs (Ghisellini and Tavecchio, 2015). The emission region size can be estimated through the observed variability time scale $\tau = 1.44$ d implying that $R_b \leq \delta c\tau/(1+z) \approx 3.5 \times 10^{16}$ cm when $\delta = 18$ and $R_b = 1.92 \times 10^{16}$ cm when $\delta = 10$. The SEDs during quiescent and flaring states are modelled using one-zone leptonic models that include the synchrotron, SSC and external inverse Compton processes; the model parameters are estimated using the MCMC method. The underlying electron energy density is considered to have a broken power-law shape presented in (Sahakyan and Gasparyan, 2017).
The modelings with their estimated parameters are depicted in Fig. 3 and Table 1.

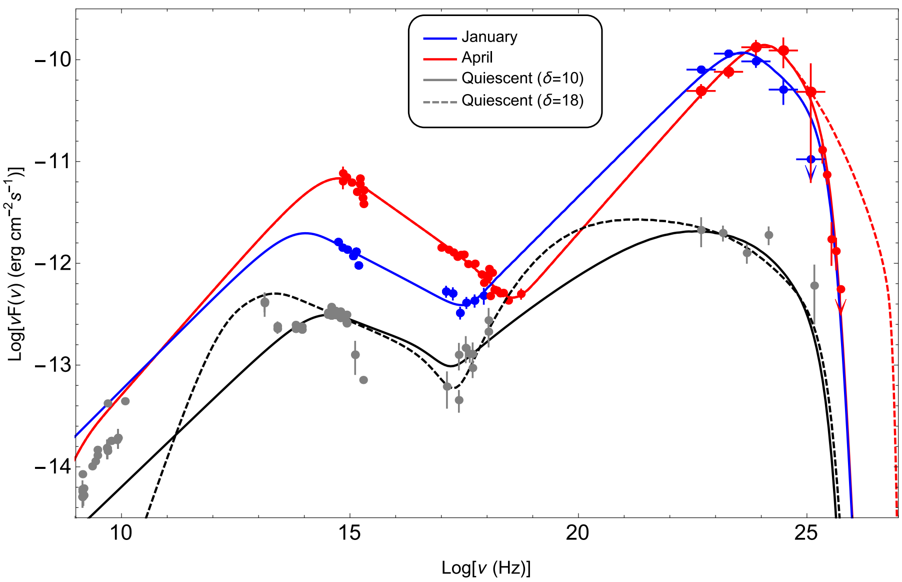

Figure 3. The broadband SED of PKS 1441+25 for January (red), April (blue) and for the quiescent state (gray). The model parameters are presented in Table 1. The UV-X-ray and VHE γ-ray data observed in January and April are from Abeysekara et al. (2015) and HE γ-ray data (Fermi LAT) are from this work.

The jet power in the form of magnetic field and electron kinetic energy are calculated by $L_B = \pi c R_b^2 \Gamma^2 \mathrm{U_B}$ and $L_e = \pi c R_b^2 \Gamma^2 \mathrm{U_e}$, respectively, and are given in Table 1. The jet power in the electrons changes in the range $(4.5 - 9.6) \times 10^{45}$ erg s^{-1} during the flares, while in the quiescent state it is of the order of $(2.1 - 4.1) \times 10^{45}$ erg s^{-1}.
The modelling shows that there is a hint of hardening of the low-energy index ($\sim$1.98) of the underlying non-thermal distribution of electrons responsible for the emission in 2015 April. Such hardening agrees with the γ-ray data, which pointed out a significant γ-ray photon index hardening on 2015 April 13 to 28. During the flaring periods, there are evident changes also in the underlying electron distribution. The electron distribution best describing the data observed in April hints at i) hardening of the low energy index, ii) a higher break at $\sim$3.1 GeV and maximum energies of 203 GeV. E_{br} and E_{max} are expected to shift, as the γ-ray spectrum observed in April is slightly inclined toward HEs, as compared with the January spectrum (see Fig. 3). Most probably these changes in spectrum caused the detection of this source in VHE γ-ray band.
More detailed interpretation of the obtained results can be found in (Sahakyan and Gasparyan, 2017).

Table 1. Model parameters.

	Parameter	Quiescent	Quiescent	January	April
Doppler factor	δ	10	18	18	18
Normalization of electron distribution	$N_0' \times 10^{48}$ eV^{-1}	$10.68^{+3.09}_{-2.64}$	$43.44^{+6.59}_{-7.76}$	$23.83^{+8.11}_{-7.32}$	$6.12^{+1.67}_{-1.56}$
Low-energy electron spectral index	α_1	2.14 ± 0.04	$2.09^{+0.03}_{-0.04}$	$2.10^{+0.04}_{-0.05}$	1.98 ± 0.03
High-energy electron spectral index	α_2	$3.39^{+0.27}_{-0.14}$	3.38 ± 0.06	3.46 ± 0.06	3.64 ± 0.01
Minimum electron energy	$E'_{\rm min}$ (MeV)	$1.84^{+1.75}_{-1.23}$	$286.37^{+30.64}_{-25.39}$	$1.97^{+0.31}_{-0.34}$	$4.16^{+1.00}_{-1.86}$
Break electron energy	$E'_{\rm br}$ (GeV)	$2.83^{+0.51}_{-0.31}$	$1.11^{+0.14}_{-0.12}$	$1.62^{+0.23}_{-0.15}$	$3.11^{+0.15}_{-0.23}$
Maximum electron energy	$E'_{\rm max}$ (GeV)	$46.27^{+49.74}_{-13.76}$	$82.32^{+13.47}_{-17.14}$	$127.82^{+26.74}_{-24.75}$	$202.79^{+21.2}_{-14.6}$
Magnetic field	B [G]	0.19 ± 0.013	0.046 ± 0.002	$0.11^{+0.005}_{-0.004}$	$0.18^{+0.009}_{-0.006}$
Jet power in magnetic field	$L_B \times 10^{43}$ erg s^{-1}	0.49	0.31	1.71	4.51
Jet power in electrons	$L_e \times 10^{45}$ erg s^{-1}	2.11	4.07	9.60	4.47

3.2. More FSRQs on VHE γ-ray map

In order to understand the phyical processes in the jets of FSRQs, the set of FSRQs have to be explored. Besides the PKS 1441+25 blazar, we initiated to model the SEDs in quiescent and different flaring states of PKS 1510-089, PKS 1222+216, 3C 279 FSRQs, which have been detected in VHE γ-ray band, as well.

PKS 1510-089 at a redshift $z = 0.361$ is a γ-ray bright quasar (H. E. S. S. Collaboration et al., 2013), (Aleksić et al., 2014). It is monitored in many energy bands, showing several bright periods with most rapid changes observed in the HE γ-ray band (the flux doubling timescale is as short as $\sim$20 minutes (Foschini et al., 2013)). From many flares we selected these observed in March 2009 (Barnacka et al., 2014), in February-April 2012 (Aleksić et al., 2014), on 18 May 2015 (2015A) and on 22 May 2015 (2015B) which demonstrated interesting modification of the flux and photon index. The data in the quiescent state are time-averaged spectra from ASI science data center.

PKS 1222+216 has been active in the MeV/GeV band since September 2009 followed by brightening also in other observable wavebands. The source underwent two major flares with the maximum of $F_{(\gamma,>100MeV)} = 10^{-5}$ photon cm^{-2} s^{-1} in April and June 2010 (Tanaka et al., 2011). During the second flare the MAGIC telescope also observed increased γ-ray emission with a flux doubling timescale of $\sim$ 10 min (Aleksić et al., 2011). The data for Flare 1 are from (Tavecchio et al., 2011), while for the quiescent state (collected from August 2008 to 12 September 2009) and Flare 2 are from (Lei and Wang, 2015).

3C 279 is probably one of the best and most studied blazar in the γ-ray sky. The emission from this blazar is variable in almost all observed frequencies. Sometimes the flares are simultaneous while in general different time lags are observed. In (Hayashida et al., 2012), analyzing multiwavelength light curves, they found at least 5 periods between 2008 and 2010 when the source was in the flaring state. Each of these flares is different (by means of the flux changes observed in different bands) and needs to be studied individually. For the current study we picked the Flare B (19 November- 9 December 2008) and G (30 July - 2 August 2009) from (Hayashida et al., 2012). During the first flare, the flux in the optical and γ-ray bands increased simultaneously, while the X-ray flux was relatively constant. On the contrary, during the second flare, the increase was observed in all bands (optical, X-ray and γ-ray). For the quiescent state the data collected from April to July 2010 are used (Paliya et al., 2015).

In Fig. 4 the multiwavelength SEDs of PKS 1510-089, PKS 1222+216 and 3C 279 are shown in the quiescent and flaring states. The observed fast variability indicates that their emission regions are compact but their localization is an open problem. Along the jet, the emission can be produced in different zones, and depending on the distance from the central black hole different components can contribute to the observed emission (Sikora et al., 2009).

The strong amplification of the emission from blazars can be explained by means of introducing

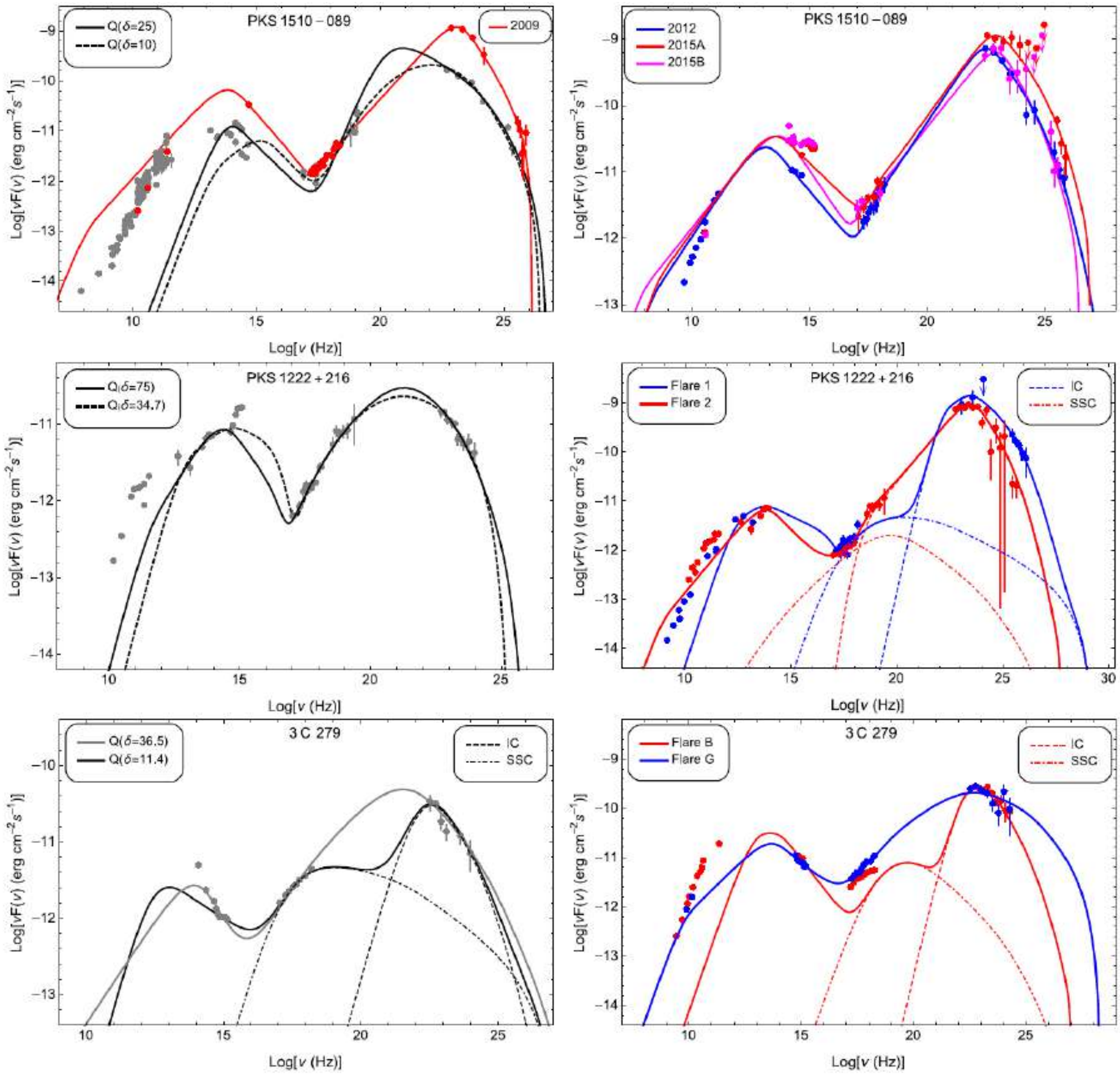

Figure 4. The broadband SEDs of blazars in the flaring and quiescent states. When EBL absorption is significant, the model and data are corrected for EBL absorption.

changes in the emission region parameters (e.g., in the magnetic field, emitting region size, bulk Lorentz factor and others, and/or particle energy distribution). We initiated to explain the flares with the change in one or two parameters is enough to explain the flares. During the flaring periods considered here both the low-energy and HE components are increased but the modification of HE emission component is more drastic. The increase of the second component is most likely due to moving of the emitting region outside the BLR. In the modeling of broadband SEDs we discuss two possibilities. First, we assume that δ has increased from the quiescent to the flaring periods (the values are given in Table 2), and then we assume that it was constant.

The results of the SEDs modeling are shown in Fig. 4 with the corresponding parameters in Table 2 where along with the best fit values also the uncertainties in the parameter estimation are provided. The SEDs observed during quiescent and flaring states are modeled using one-zone leptonic synchrotron and IC models, taking into account the seed photons originating inside and outside of the jet. The energy spectrum of the population of electrons in the jet frame, which is responsible for the non-thermal emission, is assumed to have a broken power-law shape (Gasparyan et al., 2018a).

Let us discuss the obtained results for 3C 279 FSRQ as perhaps the most interesting and complex SEDs are observed for this source (lower panel in Fig. 4). In the quiescent state the tail of the synchrotron emission is defined by the optical data, implying that the peak of the low-energy (synchrotron) component should be $< 10^{14}$ Hz. The IC scattering of these synchrotron photons is in the

Table 2. The parameters derived from the modeling of the SEDs of blazars in the quiescent and flaring states. For the emitting region size the following parameters were considered: for PKS 1510-089- $R = 4 \times 10^{14}$ cm and $R = 10^{15}$ cm for the quiescent and flaring states respectively; for PKS 1222+216- $R = 4.6 \times 10^{14}$ cm and $R = 10^{15}$ cm for the quiescent and flaring states respectively; for 3C 279- $R = 3.4 \times 10^{15}$ cm, $R = 1.1 \times 10^{16}$ cm and $R = 5.8 \times 10^{17}$ cm for the quiescent, periods B and G respectively.

	α_1	α_2	$E'_{\rm min}$	$E'_{\rm br}$	$E'_{\rm max}$	B	L_B	L_e
			MeV	GeV	GeV	G	$\times 10^{41}$ erg s^{-1}	$\times 10^{44}$ erg s^{-1}
PKS 1510-089								
Q ($\delta = 10$)	$2.17^{+0.34}_{-0.27}$	$4.01^{+0.10}_{-0.07}$	$262.59^{+34.74}_{-56.62}$	$0.60^{+0.09}_{-0.09}$	$30.16^{+7.68}_{-4.04}$	$7.89^{+2.26}_{-1.45}$	37.3	1.67
Q ($\delta = 25$)	$1.83^{+0.05}_{-0.04}$	$3.96^{+0.02}_{-0.02}$	$514.92^{+9.94}_{-3.21}$	$0.58^{+0.02}_{-0.02}$	$90.75^{+4.48}_{-4.20}$	$0.37^{+0.01}_{-0.01}$	3.2	22
2009 ($\delta = 25$)	$1.91^{+0.01}_{-0.01}$	$4.13^{+0.20}_{-0.20}$	$0.77^{+0.02}_{-0.07}$	$0.63^{+0.01}_{-0.01}$	$25.77^{+0.59}_{-1.17}$	$0.45^{+0.01}_{-0.01}$	4.9	537
2012 ($\delta = 25$)	$1.93^{+0.03}_{-0.03}$	$3.84^{+0.03}_{-0.02}$	$0.93^{+0.21}_{-0.22}$	$0.296^{+0.009}_{-0.009}$	$74.87^{+42.11}_{-27.63}$	$0.357^{+0.002}_{-0.002}$	2.99	604.42
2015A ($\delta = 25$)	$2.02^{+0.10}_{-0.06}$	$3.68^{+0.08}_{-0.06}$	$1.27^{+0.80}_{-0.40}$	$0.46^{+0.08}_{-0.08}$	$139.88^{+120.62}_{-66.16}$	$0.34^{+0.01}_{-0.02}$	2.68	758.99
2015B ($\delta = 25$)	$2.11^{+0.04}_{-0.04}$	$4.04^{+0.12}_{-0.09}$	$0.61^{+0.11}_{-0.07}$	$0.52^{+0.07}_{-0.04}$	$54.71^{+23.66}_{-17.26}$	$0.46^{+0.02}_{-0.02}$	4.99	598.16
PKS 1222+216								
Q ($\delta = 34.7$)	$2.26^{+0.09}_{-0.07}$	$3.24^{+0.04}_{-0.04}$	$58.4^{+2.82}_{-3.01}$	$0.50^{+0.07}_{-0.04}$	$4.8^{+0.01}_{-0.01}$	$2.26^{+0.03}_{-0.03}$	49.8	3.2
Q ($\delta = 75$)	$1.86^{+0.02}_{-0.01}$	$3.93^{+0.06}_{-0.04}$	$38.90^{+1.79}_{-0.89}$	$1.07^{+0.04}_{-0.02}$	$11.13^{+0.06}_{-0.53}$	$0.162^{+0.003}_{-0.003}$	5.51	30.3
Flare1 ($\delta = 75$)	$2.24^{+0.42}_{-0.32}$	$3.41^{+0.16}_{-0.14}$	$60.07^{+13.12}_{-10.38}$	$0.31^{+0.07}_{-0.07}$	$13.16^{+2.34}_{-2.11}$	$0.42^{+0.03}_{-0.03}$	36.8	10.5
Flare2 ($\delta = 75$)	$1.959^{+0.005}_{-0.004}$	$3.91^{+0.01}_{-0.01}$	$1.04^{+0.03}_{-0.03}$	$0.334^{+0.005}_{-0.005}$	$294.75^{+28.33}_{-21.82}$	$0.473^{+0.002}_{-0.002}$	47.2	15.2
3C 279								
Q ($\delta = 11.4$)	$1.98^{+0.09}_{-0.13}$	$3.47^{+0.08}_{-0.03}$	$60.01^{+4.52}_{-4.53}$	$0.14^{+0.01}_{-0.01}$	$15.71^{+4.24}_{-3.88}$	$2.07^{+0.03}_{-0.06}$	242	3.7
Q ($\delta = 36.5$)	$1.91^{+0.01}_{-0.01}$	$4.28^{+0.04}_{-0.07}$	$4.77^{+4.29}_{-1.49}$	$2.86^{+0.07}_{-0.14}$	$469.41^{+34.04}_{-42.68}$	$0.0195^{+0.0009}_{-0.0003}$	2.26	285.73
Flare B ($\delta = 36.5$)	$2.598^{+0.307}_{-0.536}$	$4.17^{+0.43}_{-0.38}$	$129.76^{+38.79}_{-35.88}$	$0.48^{+0.11}_{-0.09}$	$121.51^{+94.66}_{-71.88}$	$0.56^{+0.06}_{-0.06}$	1872.7	9.3
Flare G ($\delta = 36.5$)	$2.10^{+0.05}_{-0.05}$	$3.74^{+0.03}_{-0.03}$	$121.10^{+31.10}_{-33.14}$	$11.72^{+1.01}_{-0.96}$	$2182.01^{+449.11}_{-238.69}$	$0.00056^{+0.00003}_{-0.00003}$	32.04	4801.56

Klein-Nishina regime ($\sim \gamma\ \nu_{syn}$), which means that it can explain the observed γ-ray data only if high δ is assumed. Thus, we assume two possibilities: when $\delta = 11.4$ is considered, the emission is explained by SSC, plus an additional contribution from BLR photons, instead, when $\delta = 36.5$, the emission in both X- and γ-ray bands are from IC scattering of synchrotron photons. In both cases, α_1 does not change significantly: $\alpha_1 = 1.98 \pm 0.11$ and $\alpha_1 = 1.91 \pm 0.01$ for $\delta = 11.4$ and $\delta = 36.5$, respectively. The break energy is higher when δ=36.5 is used ($E^{'}_{br} = (2.86 \pm 0.11)$ GeV versus $E^{'}_{br} = (0.14 \pm 0.01)$ GeV), since the average energy of synchrotron photons is lower than that of BLR photons. When SSC+BLR model is used, the data can be explained for the jet with a total luminosity of $L_{jet} = 3.9 \times 10^{44}$ erg s^{-1}, and both the electrons and the magnetic field are almost in equipartition $U_e/U_B = 15.3$. For only SSC model, $L_{jet} = 2.9 \times 10^{46}$ erg s^{-1} and $U_e/U_B = 1.3 \times 10^5$. During the Flare B, the emission in both optical and γ-ray bands increased, but it was almost constant in the X-ray band. Accordingly, in the fit we assume that the X-rays are due to another component, and require that SSC emission from the electron population producing the radio to optical emission does not over predict the observed X-ray flux (low right panel in Fig. 4). HE emission is modeled by IC scattering of dusty torus photons on the electrons with the power-law indexes $\alpha_1 = 2.56 \pm 0.44$ and $\alpha_2 = 4.17 \pm 0.41$ changing at $E^{'}_{br} \approx (0.48 \pm 0.10)$ GeV, and $L_{jet} = 1.1 \times 10^{45}$ erg s^{-1}. During the Flare G, due to the simultaneous increase observed in the optical, X-ray and γ-ray bands, we conclude that the same SSC component is responsible for the emission in these bands. The emitting region size is larger (in (Hayashida et al., 2012) it has been shown that the flux variation time is 15 days), so a lower magnetic field $B = (560 \pm 30)\ \mu$G is obtained which results in the change of other parameters, e.g., $E^{'}_{br} = 11.72 \pm 0.98$ GeV. The X-ray data allows the precise estimate of α_1 to be 2.10 ± 0.05, a value which is expected from strong shock acceleration theories. In the jet the particle energy strongly dominates over the magnetic field ($U_e/U_B > 10^5$) and the jet total luminosity is $L_{jet} = 4.8 \times 10^{47}$ erg s^{-1}.
The obtained results presented in Table 2 are interpreted in (Gasparyan et al., 2018a).
The obtained results allow to quantitatively evaluate the jet energetics, break energy in the underlying

electron distribution in different states, which is crucial for investigating the changes in the physical state of the jet which caused the flares. However, the parameters describing the underlying electron distribution below the break are poorly constrained, because the data describing the rising part of both low-energy and HE components are missing. It did not allow us to exactly identify the processes responsible for the acceleration of particles in the jet. In principle, a similar study for the periods identified by the X-ray data can provide a chance to investigate the dominant particle acceleration processes, if the X-ray spectra define the rising part of the HE component.

4. On the multi-wavelength Emission from CTA 102

The modeling of blazar SEDs in quiescent and flaring states enables to understand the physical processes responsible for the emission. However, considering only the seven FSRQs detected in VHE γ-ray band we are limited for detailed investigation of the emission processes. Since the data only for observation in short periods are available and sometimes they are not simultaneous. Therefore, studying the emission only from FSRQs detected in the VHE γ-ray band does not allow to investigate the radiative output of emitting region while it moves along the jet. In order to study the emission produced from different zones of the jet we investigated the emission from well know blazar CTA 102. This source was selected since it is continuously monitored in various energy bands which provides huge amount of data allowing to study not only temporal correlation of emission in various bands but also model SEDs with simultaneous data observed in various periods. CTA 102 is a distant HE γ-ray emitting blazar ($z = 1.037$) detected but due to its distant most likely it cannot be observed in the VHE γ-ray band due to EBL strong absorption. For this blazar the large amount of data in radio, optical, X-ray and γ-ray bands are available, which enable to investigate the physical processes in both quiescent and active states of the jet, as well as distinguish the emission regions along the jet in different active periods.
For the present study we use the publicly available Fermi LAT, Swift UVOT/ XRT, NuStar data acquired in the period 2016-2018 when large-amplitude flares of CTA 102 were observed(Fig. 5). In the γ-ray band, Fermi LAT observed several prominent flares that followed a harder-when-brighter behavior. The peak γ-ray flux above 100 MeV, $(3.55 \pm 0.55) \times 10^{-5}$ photon cm^{-2} s^{-1} was observed on MJD 57,738.47 within 4.31 minutes, corresponds to an isotropic γ-ray luminosity of $L_\gamma = 3.25 \times 10^{50}$ erg s^{-1}, comparable to the highest values observed from blazars so far. The analyses of the Swift UVOT/XRT data show an increase in the UV/optical and X-ray bands that is contemporaneous with the bright γ-ray periods. The X-ray spectrum observed by Swift XRT and NuSTAR during the γ-ray flaring period is characterized by a hard photon index of ~ 1.30. The shortest e-folding time was 4.08 ± 1.44 hr, suggesting a very compact emission region $R \leq \delta \times 2.16 \times 10^{14}$ cm (Gasparyan et al., 2018b). The SEDs of CTA 102 in several periods (having different properties in UV/optical, X-ray, and γ-ray bands) is modeled assuming a compact blob inside and outside the BLR.
Fig. 6 shows the broadband SEDs of CTA 102 in its low and active periods together with the archival radio to X-ray data (light gray) from ASI science data center. The WISE IR data are highlighted by red asterisk which are most probably due to the torus emission as the recent studies show that the detection rate of almost all γ-ray blazars was high in the WISE all-sky survey (Massaro and D'Abrusco, 2016). The comparison shows that during the considered periods the fluxes in the optical/X-ray and γ-ray bands exceed the averaged archival data: the increase is more significant in the optical/UV band. This increase in all bands is expected as the selected periods correspond to the pre-flaring, flaring and post flaring states, and the source shows different emission properties as compared with the averaged spectrum.
Period 1 (P1): MJD 57625.06-57625.39 when the source was in the bright γ-ray state coinciding with XRT observations (Obsid: 33509022 and 33509023, merged during the analyses).
Period (P2): MJD 57738.02-57738.08, bright γ-ray period coinciding with the Swift Obsid: 33509106.
Period 3 (P3): $\approx$3.1 hour period centered on MJD 57752.52, corresponding to a bright γ-ray state coinciding with Swift (Obsid: 33509112 and 88026001, merged) and NuSTAR observations.
Period 4 (P4): $\approx$8.06 hour period centered on MJD 57759.62, corresponding to the period when the highest X-ray flux was observed (Obsid: 33509115).

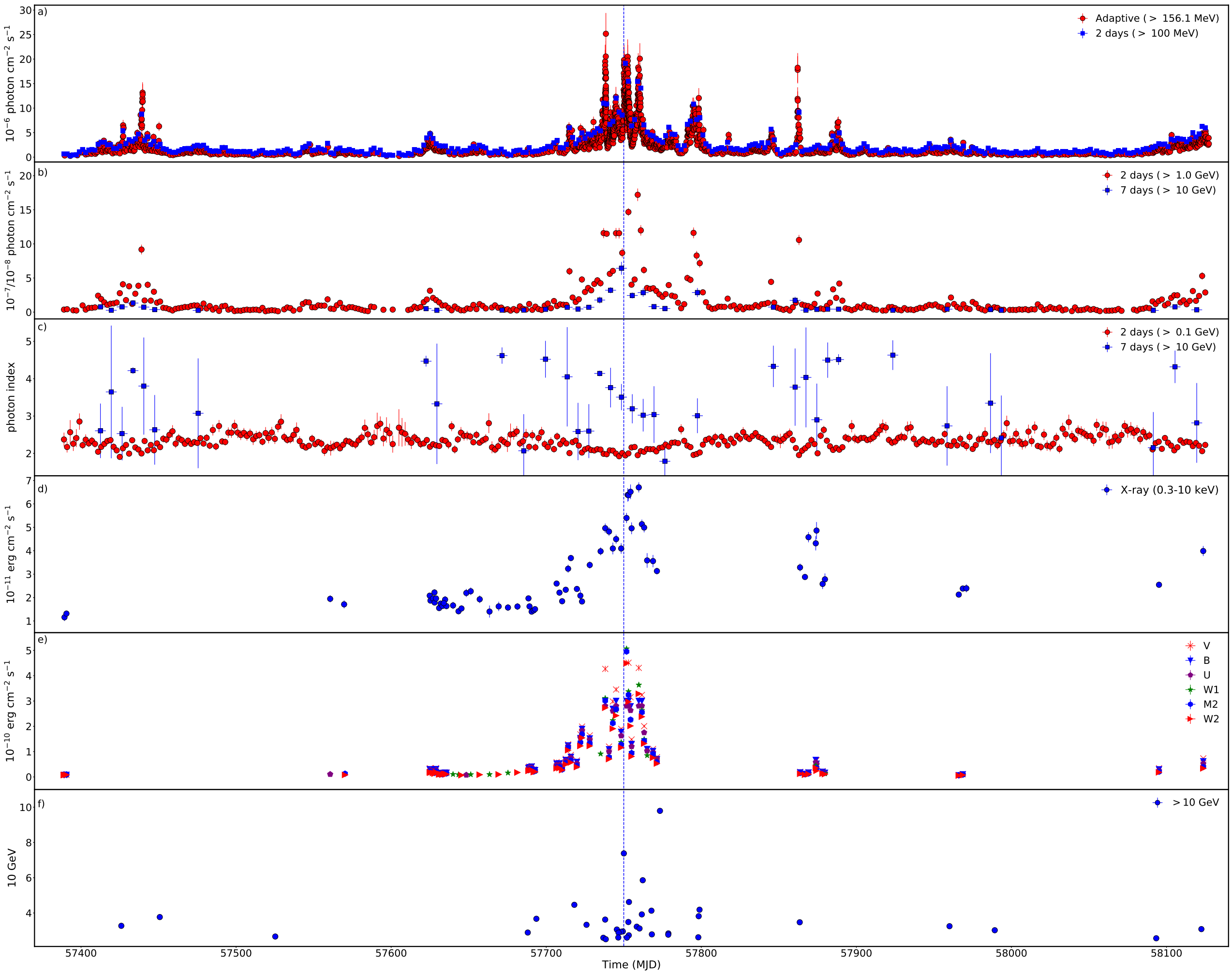

Figure 5. Multifrequency light curve of CTA 102 obtained for the period from 2008 August to 2018 January. *a)* γ-ray light curves with adaptive (red; ≥ 156.1 MeV) and 2-day (blue; 100 MeV) bins, *b) and c)* the flux and photon index with 2- and 7-days binning, *d)* Swift XRT light curve in the 0.3-10 keV range, *e)* UV/optical fluxes in V, B, U, $W1$, $M2$ and $W2$ bands and *f)* the energy and arrival times of the highest-energy photons. The vertical blue dashed line shows the period when a large flare in the $R-$ band was observed (28 December 2016).

Period 5 (P5): ≈14.66 min period centered on MJD 57862.15, corresponding to another peak of γ-ray emission and available quasi-simultaneous Swift observation on the next day (Obsid: 33509121).
Comparing our selected periods i) the low-energy component increased while its peak frequency remained relatively constant ($\leq 10^{15}$ Hz), ii) the second component increased and shifted to HEs with a strong Compton peak dominance and iii) the UV/optical, X-ray and γ-ray fluxes contemporaneously increased in P2, P3 and P4, while the emission in the UV/optical and X-ray bands was relatively constant in P1 and P5.
The blazar flares can be explained by the changes in the magnetic field, in the emitting region size and its distance from the black hole, bulk Lorentz factor, particle energy distribution, etc. (Paggi et al., 2011). For example, both emission components will be shifted to HEs when the particles are effectively re-accelerated. Only the HE component will increase when the contribution of the external photon fields starts to dominate, for example, due to the changes in the location of the emitting region (Paggi et al., 2011). However, these are not unique models for explaining the flaring events. Another possibility is the geometrical interpretation of the origin of flares, the case when the jet regions may have different viewing angles. Such a model with a twisted inhomogeneous jet was already applied to explain the emission from CTA 102 jet in the optical, infrared and radio bands (Raiteri et al., 2017). The photons of different energy come from the jet regions which have different orientations (hence,

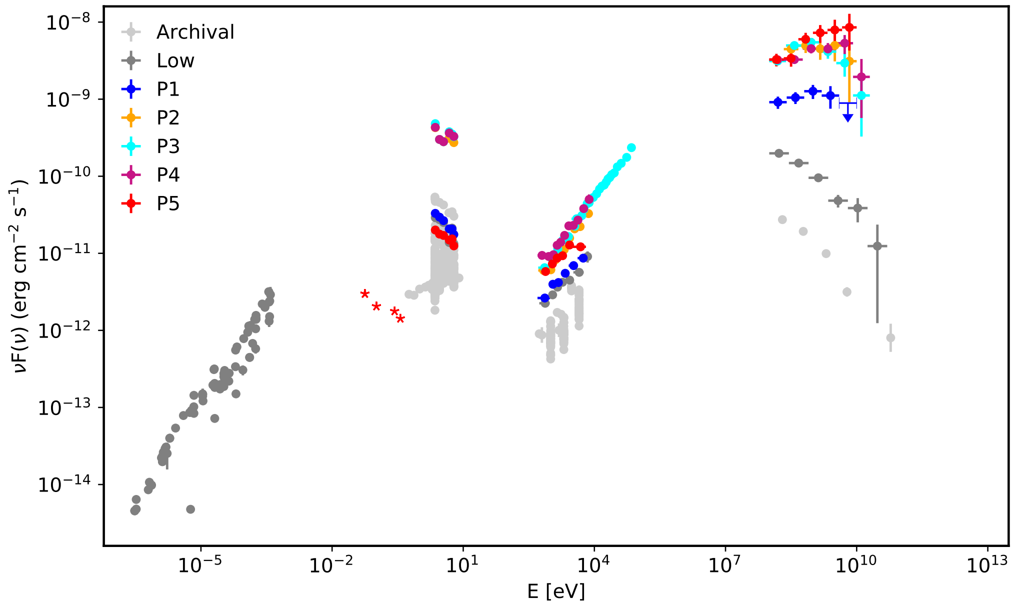

Figure 6. The broadband SEDs of CTA 102 in the selected periods. The archival data are shown in light gray.

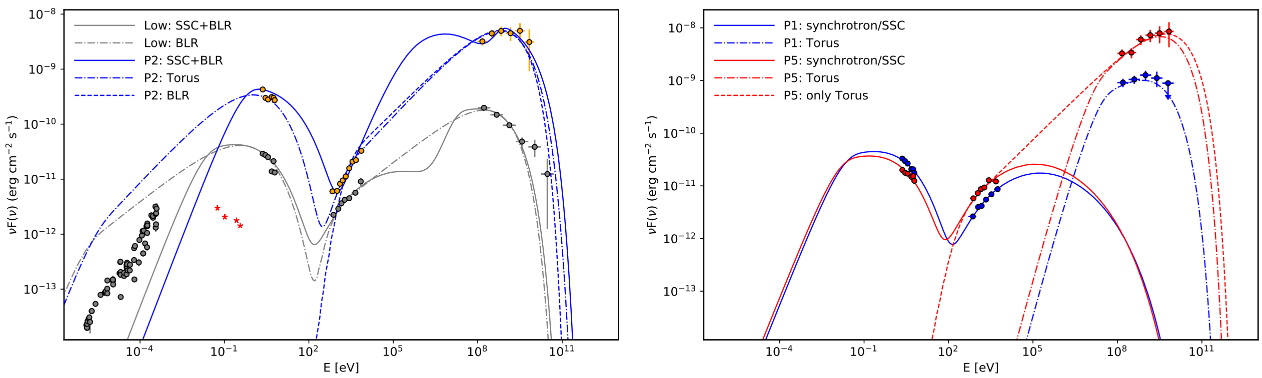

Figure 7. Modeling of the broadband SEDs of CTA 102 during the low state and P2 (left panel, gray and orange, respectively) and P1 and P5 (right panel, blue and red, respectively). The model parameters are given in Table 3. For the models applied see the text.

different Doppler boosting factors) because of the curvature of the jet.
The SEDs obtained in the low state, P1 and P5 showing different features, and in the bright P2 have been modeled. In order to account for Compton dominance, we assume the bulk Lorentz factor (δ which equals to the bulk Lorentz factor for small viewing angles, $\delta \approx \Gamma$) of the emitting region increased from 10 in the low to 20 in the active states (these are typical values estimated for FSRQs (Foschini et al., 2013)). In the modeling, the emission region is supposed to be filled by electrons having energy density of power-law with exponential shape (Gasparyan et al., 2018b).

When the SEDs in the low state and in P2 are modeled, the emission from a compact region inside and outside the BLR is discussed. Instead, when modeling the periods with lacking correlation in the γ-ray and UV/optical/X-ray bands, we assume the emission from the radio to X-rays is produced in the extended and slow-moving region unrelated to the flaring component, while the HE γ-rays come from a compact and fast-moving region outside BLR (Tavecchio et al., 2011).

Initially, we modeled the SED observed in the low state (Fig. 7; left panel). The radio data are treated as upper limits during the modeling, as the emission in this band is produced from the low-energy electrons which are perhaps from much extended regions. When the IC scatterings of both synchrotron and BLR photons are considered, the X-ray data allow to measure $E^{\prime}_{min} = 68.25 \pm 5.27$

	Low		P1	P2		P5	
	SSC+BLR	BLR	Compact	SSC+BLR	Torus	Compact	Torus
δ	10	10	20	20	20	20	20
α	2.51 ± 0.11	2.19 ± 0.02	2.12 ± 0.54	2.79 ± 0.44	1.91 ± 0.03	1.78 ± 0.52	1.95 ± 0.03
E_{min} (MeV)	68.25 ± 5.27	0.54 ± 0.03	155.59 ± 109.18	227.25 ± 26.43	1.38 ± 0.15	121.33 ± 67.33	0.63 ± 0.09
E_c (GeV)	0.67 ± 0.1	0.49 ± 0.04	1.42 ± 0.81	1.32 ± 0.43	0.98 ± 0.05	2.36 ± 1.54	3.85 ± 1.57
E_{max} (TeV)	0.57 ± 0.31	0.49 ± 0.31	0.48 ± 0.34	0.50 ± 0.30	0.41 ± 0.18	0.58 ± 0.25	0.54 ± 0.31
B (G)	5.40 ± 0.13	5.37 ± 0.14	0.23 ± 0.29	6.10 ± 0.50	1.01 ± 0.003	0.004 ± 0.042	0.015 ± 0.049
L_B (erg s^{-1})	1.75×10^{46}	1.73×10^{46}	1.47×10^{42}	1.04×10^{45}	2.86×10^{43}	3.86×10^{38}	6.44×10^{39}
L_e [erg s^{-1}]	4.66×10^{44}	2.90×10^{45}	1.73×10^{46}	2.84×10^{45}	2.74×10^{47}	7.33×10^{46}	1.97×10^{47}

Table 3. Parameters best describing the multiwavelength emission in different periods

MeV and $\alpha = 2.51 \pm 0.11$. In order to explain the observed UV/optical data, a $E_c^{'} = 0.67 \pm 0.1$ GeV cut-off is required which makes the SSC component to decay in sub-MeV band and the HE data are described only by IC of BLR photons. Alternatively, both X-ray and γ-ray data can be described by IC scattering of BLR photons (dot-dashed gray line in Fig. 7) but the low-energy tail of IC spectra can reproduce the X-ray data only if $gamma_{min} = E_e/m_e\,c^2$ is close to unity (Celotti and Ghisellini, 2008). In this case, however, the synchrotron emission of these low energy electrons with $E_{min} = 0.54 \pm 0.03$ MeV will exceed the observed radio flux, making this scenario unlikely.
For the flaring states, it is found, that the HE data are better described when the infrared thermal radiation of the dusty torus is considered. In the flaring periods when the correlation between the γ-ray and UV/optical/X-ray bands is lacking, the γ-ray emission can be produced from the interaction of fresh electrons in a different blob, which does not make a dominant contribution at lower energies. The estimated values for flaring states are discussed and compared within each other in (Gasparyan et al., 2018b).
Consequently, some crucial parameters for the jet parameters were possible to constrain, for instance, the jet luminosity at different spatial regions along the jet, which can help to understand the effective γ-ray emission regions in the jets of FSRQs.

5. Conclusion

The origin of emission from FSRQ blazars which have been detected in VHE γ-ray band are studied. The ongoing physical processes in jets of these sources differ from the conventional the near-black-hole dissipation scenarios, making these objects interesting to investigate. In the study five FSRQs are included: four detected in VHE band, and one additional FSRQ, for which there are simultaneous large amount of data, which is crucial for not only probing the radiative processes in the jets but also identifying the effective γ-ray radiative zones within the jet. For these objects, the data from Fermi LAT, Swift UVOT/XRT and NuStar telescopes were collected/ analyzed, which enables to identify major activities/flares, study their properties and constrain the emission region size. The physical processes in the jets are studied by detailed investigation of their multiwavelength emission spectra. For that purpose, a python code is developed which in the optimization of model parameters uses MCMC methods. The modeling of the observed multiwavelength emission of blazar jets allows to estimate or put constraints on such important physical parameters of the jets as their composition, power, strength of magnetic field, electron energy distribution, etc., which are crucial for understanding of their physics. The obtained results are important and useful also for the future studies in the field.

References

C. M. Urry and P. Padovani. Unified Schemes for Radio-Loud Active Galactic Nuclei. , 107:803, September 1995. doi: 10.1086/133630.

G. Ghisellini, L. Maraschi, and A. Treves. Inhomogeneous synchrotron-self-Compton models and the problem of relativistic beaming of BL Lac objects. , 146:204–212, May 1985.

L. Maraschi, G. Ghisellini, and A. Celotti. A jet model for the gamma-ray emitting blazar 3C 279. , 397:L5–L9, September 1992. doi: 10.1086/186531.

M. Sikora, M. C. Begelman, and M. J. Rees. Comptonization of diffuse ambient radiation by a relativistic jet: The source of gamma rays from blazars? , 421:153–162, January 1994. doi: 10.1086/173633.

G. Ghisellini and F. Tavecchio. Canonical high-power blazars. , 397:985–1002, August 2009. doi: 10.1111/j.1365-2966.2009.15007.x.

S. Gasparyan. Modeling The Multiwavelength Spectra of Blazars. , 12(1):83–95, Feb 2019.

K. Mannheim and P. L. Biermann. Gamma-ray flaring of 3C 279 : a proton-initiated cascade in the jet ? , 253:L21–L24, Jan 1992.

A. Mücke and R. J. Protheroe. A proton synchrotron blazar model for flaring in Markarian 501. *Astroparticle Physics*, 15:121–136, March 2001. doi: 10.1016/S0927-6505(00)00141-9.

M. Böttcher, A. Reimer, K. Sweeney, and A. Prakash. Leptonic and Hadronic Modeling of Fermi-detected Blazars. , 768(1):54, May 2013. doi: 10.1088/0004-637X/768/1/54.

Marie-Helene Ulrich, Laura Maraschi, and C. Megan Urry. Variability of Active Galactic Nuclei. , 35: 445–502, Jan 1997. doi: 10.1146/annurev.astro.35.1.445.

J. G. Kirk, F. M. Rieger, and A. Mastichiadis. Particle acceleration and synchrotron emission in blazar jets. , 333:452–458, May 1998.

V. Zabalza. naima: a python package for inference of relativistic particle energy distributions from observed nonthermal spectra. *Proc. of International Cosmic Ray Conference 2015*, page in press, 2015.

Darren Wraith, Martin Kilbinger, Karim Benabed, Olivier Cappé, Jean-François Cardoso, Gersende Fort, Simon Prunet, and Christian P. Robert. Estimation of cosmological parameters using adaptive importance sampling. , 80(2):023507, Jul 2009. doi: 10.1103/PhysRevD.80.023507.

Jonathan Goodman and Jonathan Weare. Ensemble samplers with affine invariance. *Communications in Applied Mathematics and Computational Science*, 5(1):65–80, Jan 2010. doi: 10.2140/camcos.2010.5.65.

Daniel Foreman-Mackey, David W. Hogg, Dustin Lang, and Jonathan Goodman. emcee: The MCMC Hammer. , 125(925):306, Mar 2013. doi: 10.1086/670067.

H. T. Liu and J. M. Bai. Absorption of 10-200 GeV Gamma Rays by Radiation from Broad-Line Regions in Blazars. , 653(2):1089–1097, Dec 2006. doi: 10.1086/509097.

J. Poutanen and B. Stern. GeV Breaks in Blazars as a Result of Gamma-ray Absorption Within the Broad-line Region. , 717:L118–L121, July 2010. doi: 10.1088/2041-8205/717/2/L118.

A. U. Abeysekara, S. Archambault, A. Archer, T. Aune, A. Barnacka, W. Benbow, R. Bird, J. Biteau, J. H. Buckley, V. Bugaev, J. V. Cardenzana, M. Cerruti, X. Chen, and et. al Christiansen. Gamma-Rays from the Quasar PKS 1441+25: Story of an Escape. , 815(2):L22, Dec 2015. doi: 10.1088/2041-8205/815/2/L22.

M. L. Ahnen, S. Ansoldi, L. A. Antonelli, P. Antoranz, A. Babic, B. Banerjee, P. Bangale, U. Barres de Almeida, J. A. Barrio, W. Bednarek, and et al. Very High Energy γ-Rays from the Universe's Middle Age: Detection of the z = 0.940 Blazar PKS 1441+25 with MAGIC. , 815(2):L23, Dec 2015. doi: 10.1088/2041-8205/815/2/L23.

M. L. Ahnen, S. Ansoldi, L. A. Antonelli, P. Antoranz, C. Arcaro, A. Babic, B. Banerjee, P. Bangale, U. Barres de Almeida, J. A. Barrio, J. Becerra González, W. Bednarek, E. Bernardini, A. Berti, B. Biasuzzi, and et.al Biland. Detection of very high energy gamma-ray emission from the gravitationally lensed blazar QSO B0218+357 with the MAGIC telescopes. , 595:A98, Nov 2016. doi: 10.1051/0004-6361/201629461.

Paolo S. Coppi and Felix A. Aharonian. Simultaneous X-Ray and Gamma-Ray Observations of TEV Blazars: Testing Synchro-Compton Emission Models and Probing the Infrared Extragalactic Background. , 521(1):L33–L36, Aug 1999. doi: 10.1086/312168.

Piero Madau and E. Sterl Phinney. Constraints on the Extragalactic Background Light from Gamma-Ray Observations of High-Redshift Quasars. , 456:124, Jan 1996. doi: 10.1086/176633.

Michael S. Shaw, Roger W. Romani, Garret Cotter, Stephen E. Healey, Peter F. Michelson, Anthony C. S. Readhead, Joseph L. Richards, Walter Max-Moerbeck, Oliver G. King, and William J. Potter. Spectroscopy of Broad-line Blazars from 1LAC. , 748(1):49, Mar 2012. doi: 10.1088/0004-637X/748/1/49.

R. Mirzoyan. Discovery of Very High Energy Gamma-Ray Emission from the distant FSRQ PKS 1441+25 with the MAGIC telescopes. *The Astronomer's Telegram*, 7416:1, Apr 2015.

Reshmi Mukherjee. Very-high-energy gamma-ray emission from PKS 1441+25 detected with VERITAS. *The Astronomer's Telegram*, 7433:1, Apr 2015.

B. Lott, L. Escande, S. Larsson, and J. Ballet. An adaptive-binning method for generating constant-uncertainty/constant-significance light curves with Fermi-LAT data. , 544:A6, August 2012. doi: 10.1051/0004-6361/201218873.

N. Sahakyan and S. Gasparyan. High energy gamma-ray emission from PKS 1441+25. , 470:2861–2869, September 2017. doi: 10.1093/mnras/stx1402.

A. Paggi, A. Cavaliere, V. Vittorini, F. D'Ammando, and M. Tavani. Flaring Patterns in Blazars. , 736:128, August 2011. doi: 10.1088/0004-637X/736/2/128.

G. Ghisellini and F. Tavecchio. Fermi/LAT broad emission line blazars. , 448:1060–1077, April 2015. doi: 10.1093/mnras/stv055.

H. E. S. S. Collaboration, A. Abramowski, F. Acero, F. Aharonian, A. G. Akhperjanian, G. Anton, S. Balenderan, A. Balzer, A. Barnacka, Y. Becherini, and et al. H.E.S.S. discovery of VHE γ-rays from the quasar PKS 1510-089. , 554:A107, Jun 2013. doi: 10.1051/0004-6361/201321135.

J. Aleksić, S. Ansoldi, and et al. MAGIC gamma-ray and multi-frequency observations of flat spectrum radio quasar PKS 1510-089 in early 2012. , 569:A46, September 2014. doi: 10.1051/0004-6361/201423484.

L. Foschini, G. Bonnoli, G. Ghisellini, G. Tagliaferri, F. Tavecchio, and A. Stamerra. Fermi/LAT detection of extraordinary variability in the gamma-ray emission of the blazar PKS 1510-089. , 555:A138, July 2013. doi: 10.1051/0004-6361/201321675.

Anna Barnacka, Rafal Moderski, Bagmeet Behera, Pierre Brun, and Stefan Wagner. PKS 1510-089: a rare example of a flat spectrum radio quasar with a very high-energy emission. , 567:A113, Jul 2014. doi: 10.1051/0004-6361/201322205.

Y. T. Tanaka, Ł. Stawarz, D. J. Thompson, F. D'Ammand o, S. J. Fegan, B. Lott, D. L. Wood, C. C. Cheung, J. Finke, S. Buson, L. Escande, S. Saito, M. Ohno, T. Takahashi, D. Donato, J. Chiang, M. Giroletti, F. K. Schinzel, G. Iafrate, F. Longo, and S. Ciprini. Fermi Large Area Telescope Detection of Bright γ-Ray Outbursts from the Peculiar Quasar 4C +21.35. , 733(1):19, May 2011. doi: 10.1088/0004-637X/733/1/19.

J. Aleksić, L. A. Antonelli, and et al. MAGIC Discovery of Very High Energy Emission from the FSRQ PKS 1222+21. , 730:L8, March 2011. doi: 10.1088/2041-8205/730/1/L8.

F. Tavecchio, J. Becerra-Gonzalez, G. Ghisellini, A. Stamerra, G. Bonnoli, L. Foschini, and L. Maraschi. On the origin of the γ-ray emission from the flaring blazar PKS 1222+216. , 534:A86, October 2011. doi: 10.1051/0004-6361/201117204.

Maichang Lei and Jiancheng Wang. Location of gamma-ray flaring region in quasar 4C +21.35. , 67 (4):79, Aug 2015. doi: 10.1093/pasj/psv055.

M. Hayashida, G. M. Madejski, K. Nalewajko, M. Sikora, A. E. Wehrle, P. Ogle, W. Collmar, S. Larsson, Y. Fukazawa, R. Itoh, J. Chiang, Ł. Stawarz, R. D. Blandford, J. L. Richards, W. Max-Moerbeck, A. Readhead, R. Buehler, E. Cavazzuti, and et. al Ciprini. The Structure and Emission Model of the Relativistic Jet in the Quasar 3C 279 Inferred from Radio to High-energy γ-Ray Observations in 2008-2010. , 754(2):114, Aug 2012. doi: 10.1088/0004-637X/754/2/114.

Vaidehi S. Paliya, S. Sahayanathan, and C. S. Stalin. Multi-Wavelength Observations of 3C 279 During the Extremely Bright Gamma-Ray Flare in 2014 March-April. , 803(1):15, Apr 2015. doi: 10.1088/0004-637X/803/1/15.

M. Sikora, Ł. Stawarz, R. Moderski, K. Nalewajko, and G. M. Madejski. Constraining Emission Models of Luminous Blazar Sources. , 704:38–50, October 2009. doi: 10.1088/0004-637X/704/1/38.

S. Gasparyan, N. Sahakyan, and P. Chardonnet. The origin of HE and VHE gamma-ray flares from FSRQs. *International Journal of Modern Physics D*, 27(10):1844007, Jan 2018a. doi: 10.1142/S0218271818440078.

S. Gasparyan, N. Sahakyan, V. Baghmanyan, and D. Zargaryan. On the Multiwavelength Emission from CTA 102. , 863(2):114, Aug 2018b. doi: 10.3847/1538-4357/aad234.

F. Massaro and R. D'Abrusco. The Infrared-Gamma-Ray Connection: A WISE View of the Extragalactic Gamma-Ray Sky. , 827:67, August 2016. doi: 10.3847/0004-637X/827/1/67.

C. M. Raiteri, M. Villata, J. A. Acosta-Pulido, I. Agudo, A. A. Arkharov, R. Bachev, G. V. Baida, E. Benítez, G. A. Borman, W. Boschin, and et.al Bozhilov. Blazar spectral variability as explained by a twisted inhomogeneous jet. , 552:374–377, December 2017. doi: 10.1038/nature24623.

A. Celotti and G. Ghisellini. The power of blazar jets. , 385:283–300, March 2008. doi: 10.1111/j.1365-2966.2007.12758.x.